Toward Kinematics- and Kinetics-Based Predictions of Muscle Activity in Dynamic Sitting

by

Brad W. R. Roberts

A thesis submitted in partial fulfillment of the requirements for the degree of

Master of Science

Department of Mechanical Engineering
University of Alberta

Abstract

Recent work suggests that closed-loop electrical stimulation may restore dynamic trunk stability following neuromuscular impairment. However, developing such neuroprostheses requires quantitative predictions of the activation profiles of relevant muscles under different types of dynamic trunk disturbances experienced in daily life during non-impaired sitting. The types of disturbances that may be experienced include intrinsic instability or external displacement of the support surface, as well as the exposure to external trunk forces. Muscle activity predictions could be based on characteristic angular kinematics (i.e., the kinematics characterizing trunk stabilization) or the body's center of pressure (CoP) displacement in these dynamic sitting paradigms. Several challenges exist, however, that need to be resolved to allow kinematics- or kinetics-based predictions of muscle activity to be obtained in dynamic sitting. First, the kinematics characterizing trunk stabilization in unstable sitting as well as the relation between kinematics and the muscle activity in this paradigm are unknown. Second, while the body's CoP displacement in dynamic sitting can be measured by instrumenting the support surface with a force plate, in perturbing the support surface, the acquired kinetic data will contain artifacts due to acceleration of the platform. Existing methods for removing these so-called force plate inertial components (FPIC) require knowledge of the inertial properties of the platform. The objectives of this thesis research were therefore to (1): quantify the kinematics characterizing trunk stabilization in unstable sitting; (2) quantify both the spatial and temporal relations between the characteristic kinematics and the muscle activity in unstable sitting; and (3) propose and validate a method for estimating the inertial properties and FPIC for any instrumented platform. Using an unstable sitting paradigm, the angular motion of the base of support (BoS), pelvis, and trunk as well as bilateral electromyograms from fourteen trunk and upper leg muscles were recorded in fifteen non-disabled participants. To

characterize the kinematics in unstable sitting, the angular motion of the BoS, pelvis, and trunk were quantified and compared. The trunk was stabilized through relatively large BoS motion, with the trunk adopting a quasi-static pose. Based on these insights, the relationship between BoS angular displacement and the electromyograms was quantified using cross-correlation analysis. During unstable sitting, the trunk was stabilized through direction-specific activation of the trunk and upper leg muscles that preceded BoS displacement temporally. The proposed method for estimating the inertial properties and FPIC for any instrumented platform was validated exemplarily by estimating the inertial properties specifically for the Computer-Assisted Rehabilitation Environment (CAREN). Unloaded ramp-and-hold perturbations (for estimation) and unloaded random perturbations (for validation) were executed to obtain the force, moment, and motion of the CAREN platform. Inertial properties were estimated by minimizing the error between the measured and computed inertial forces and moments. Obtained estimates were validated by comparing the measured and computed forces and moments when keeping the inertial properties fixed. The estimates of the CAREN's inertial properties exhibited low variability across trials, with excellent agreement between the measured and computed forces and moments for the validation trials. Future work will use the obtained relation between BoS motion and trunk and upper leg muscle activity during unstable sitting to predict the kinematics-based muscle activation patterns within a closed-loop electrical stimulation system for dynamic sitting. Future work will also use the developed method for estimating the inertial properties and FPIC for any instrumented platform to obtain reliable estimates of the kinetic data used in analyses that quantify the relation between the body's CoP displacement and the muscle activity in dynamic sitting. Relations obtained from such analyses can again be used to predict the CoP-based muscle activation patterns within a closed-loop electrical stimulation system for dynamic sitting.

Preface

This thesis is an original work by Brad Roberts, with the following noted exceptions. The Introduction in Chapter 1, Literature Review in Chapter 2, Conclusion in Chapter 6, and Appendices are my original work. Fatemeh Gholibeigian and Justin Lewicke were responsible for the experimental design and data acquisition described in Chapters 3 and 4. I was responsible for the experimental data processing and analysis as well as the manuscript conceptualization and preparation associated with Chapters 3 and 4. Jeremy Hall and I contributed equally to the experimental design and data acquisition described in Chapter 5. Jeremy Hall was responsible for preparing the Introduction section of the manuscript associated with Chapter 5. I was responsible for the experimental data processing and analysis, as well as the remainder of the manuscript conceptualization and preparation associated with Chapter 5. Albert Vette supervised this thesis and its preparation.

Chapter 3 of this thesis is currently in press as a 'Short Communication' in the journal *Medical Engineering & Physics*, as: *Roberts BWR, Vette AH. A kinematics recommendation for trunk stability and control assessments during unstable sitting.*

Chapter 4 of this thesis is currently under review for publication as an 'Original Article' in the journal *Neuromodulation: Technology at the Neural Interface*, as: *Roberts BWR, Gholibeigian F, Lewicke J, Vette AH. Spatial and temporal relation of kinematics and muscle activity during unstable sitting.*

Chapter 5 of this thesis has been published as a 'Technical Note' in the journal *Medical Engineering & Physics*, as: *Roberts BWR, Hall JC, Williams AD, Rouhani H, Vette AH. A method to estimate inertial properties and force plate inertial components for instrumented platforms. Medical Engineering & Physics 2019;66:96–101.*

The human research described in Chapters 3 and 4 received research ethics approval from the Health Research Ethics Board (HREB) of the University of Alberta, Project Title "Use of Stochastic Resonance for Improving Postural Control in the Elderly and Individuals Post-Stroke", HREB Pro00039437, June 24, 2013.

"My goal is simple. It is a complete understanding of the universe, why it is as it is and why it exists at all."

— Stephen W. Hawking

Acknowledgments

I am sincerely grateful to my MSc supervisor, Dr. Albert Vette. He challenged and empowered me to do excellent research, and this thesis would not have been possible without his immeasurable guidance, patience, and encouragement. I could not be more fortunate to have received Albert's mentorship over the last several years.

I thank Drs. Jason Carey, Arman Hemmati, and Lindsey Westover for serving on my examining committee. I also thank those colleagues who contributed to this thesis research: Kshitij Agarwal, Dr. Juan Forero, Fatemeh Gholibeigian, Darrell Goertzen, Jeremy Hall, Justin Lewicke, Dr. Hossein Rouhani, and Andrew Williams.

I am grateful for the funding support provided by Alberta Advanced Education; Alberta Innovates; and the Natural Sciences and Engineering Research Council of Canada.

Finally, I thank my parents and siblings for their undying love, support, and belief in me.

Table of Contents

List of Tables

List of Figures

Chapter 1

1 Introduction

1.1 Background and Motivation

Human trunk stability is achieved when the trunk is in an upright position with the body's center of mass positioned inside its base of support [1,2]. The ability to stabilize the trunk following perturbations that displace the center of mass relative to its base of support is a requirement for general human function and mobility. For example, the ability to maintain seated balance may be lost if trunk stability and its control have been impaired [3]. The consequences on the ability to maintain seated balance are often especially harmful to individuals with neuromuscular impairments affecting trunk stability and its control. Individuals with spinal cord injury between the head and tenth thoracic vertebra, for example, generally experience at least some impairment of trunk function [4]. Consequently, they are often unable to maintain seated balance on their own [5,6].

Previous efforts to improve seated balance in individuals with spinal cord injury have primarily focused on wheelchair modifications that support the trunk in the anterior direction to assist in stabilizing it during quiet sitting [7–10]. However, in addition to not providing multidirectional support to the trunk during static conditions, such modifications do not take into consideration dynamic postural disturbances that may be experienced in daily life during sitting. In this light, recent work suggests that neuroprostheses utilizing electrical muscle stimulation can restore seated balance. For example, recent findings show that low-intensity, open-loop electrical stimulation can assist in stabilizing the trunk under the small perturbations experienced during quiet sitting by increasing overall trunk stiffness [11,12]. However, under larger, transient perturbations commonly experienced in daily life during sitting, stabilizing the trunk has larger compensational demands, requiring higher stimulation intensities that accelerate the start of muscle fatigue [13]. Additionally, stabilizing the trunk under such dynamic perturbations requires many relevant muscles to be activated synergistically and according to well-defined spatial and temporal activation patterns. To prevent muscle fatigue induced by electrical stimulation, low-intensity, open-loop electrical stimulation could be applied to facilitate trunk stability during quiet sitting [12]. Such open-loop electrical stimulation could be paired with intermittent closed-loop electrical stimulation that ensures fatigue-resistant trunk stability under dynamic perturbations. The fatigue-resistant spatial and temporal muscle activation patterns required for closed-loop electrical stimulation could be defined by mimicking the muscle activation patterns that non-impaired individuals use to control dynamic trunk stability. This, however, requires quantitative predictions of the activation profiles of relevant muscles under different types of dynamic trunk disturbances commonly experienced in daily life during non-impaired sitting. The types of disturbances that may be experienced include (1) intrinsic instability or (2) external displacement of the support surface, as well as (3) the exposure to external trunk forces. Muscle activity predictions could be based on characteristic angular kinematics (i.e., the kinematics characterizing trunk de- and re-stabilization) or the body's center of pressure displacement in these dynamic sitting paradigms.

Several challenges exist, however, that need to be resolved to allow kinematics- or kinetics-based predictions of muscle activity to be obtained in dynamic sitting. First, the kinematics characterizing trunk stabilization in unstable sitting [14–19] as well as the relation between kinematics and the muscle activity are unknown, but required to predict the kinematics-based muscle activation patterns in this paradigm. Second, while the body's center of pressure displacement in dynamic sitting can be measured by instrumenting the support surface with a force plate, in perturbing the support surface, the acquired kinetic data will contain artifacts due to acceleration of the platform [20]. Existing methods for removing these so-called force plate inertial components are limited by requiring knowledge of the inertial properties of the platform and by being only applicable to symmetric platforms [20].

1.2 Thesis Objective

Based on the above considerations, the objectives of this thesis research were to: (1) quantify the kinematics characterizing trunk stabilization in unstable sitting, i.e., one of the dynamic trunk disturbances commonly experienced in daily life; (2) quantify both the spatial and temporal relations between the characteristic kinematics and the muscle activity in unstable sitting; and (3) propose and validate a method for estimating the inertial properties and force plate inertial components for any instrumented platform.

1.3 Thesis Outline

Chapter 2 presents a review of the literature that is directly relevant to the work presented in this thesis research. In Chapter 3, the kinematics of the base of support, pelvis, and trunk in unstable sitting are quantified and compared. The results are then used to propose a kinematics recommendation for future studies utilizing an unstable sitting surface and kinematics-based analyses to investigate trunk stability and control. In Chapter 4, the spatial and temporal relations between characteristic angular kinematics and trunk and upper leg muscle activity in unstable sitting are quantified. The results will be used by future studies that predict the kinematics-based muscle activation patterns within a closed-loop electrical stimulation system for dynamic sitting. In Chapter 5, a novel method is proposed for estimating the inertial properties and force plate inertial components for any instrumented platform. The proposed method is then used to estimate inertial properties specifically for the extended Computer-Assisted Rehabilitation Environment, and to validate both the obtained estimates and proposed method via new experimental data. The developed method will be used by future studies that quantify the relation between the body's center of pressure displacement and the muscle activity in dynamic sitting. Chapter 6 provides concluding remarks on the scientific contribution of this thesis research, and describes future perspectives.

Chapter 2

2 Literature Review

2.1 Overview

This chapter reviews the literature that is relevant to this thesis: a review of trunk stability and control during sitting; a review of human movement kinematics; a review of electromyography; and a review of human movement kinetics.

2.2 Trunk Stability and Control During Sitting

2.2.1 Introduction

To stabilize the trunk under perturbations experienced during sitting, the central nervous system (CNS) strategically utilizes *anticipatory* and *compensatory* postural adjustments [21,22]. Anticipatory postural adjustments activate relevant muscles *prior to* predictable perturbations to counteract the perturbations and stabilize the trunk (*open-loop feed-forward postural control*) [23]. Anticipatory postural adjustments often involve co-activation of antagonist muscle pairs which increases the stiffness of the trunk and contributes to its stability [12,24]. Conversely, compensatory postural adjustments activate relevant muscles *following* unpredictable perturbations to counteract the perturbations and stabilize the trunk. Compensatory postural adjustments are based on information about the current state of the body provided by its auditory, proprioceptive, somatosensory, vestibular, and visual sensory systems (*closed-loop feedback postural control*) [22,25,26]. This sensory feedback initiates compensatory postural adjustments, which are executed through involuntary (i.e., reflexive) and voluntary muscle activation [26]. The neurally-driven *active control* (i.e., control that originates in the CNS) mechanisms described above (i.e., anticipatory and compensatory postural adjustments) are complemented by *passive control* mechanisms: intraabdominal pressure [27,28], as well as mechanical properties of the spine, muscles, and connective tissue [29,30] contribute to the overall stiffness and damping of the trunk [12,24], which passively contributes to its stability.

For small perturbations experienced during sitting (*quiet sitting*), stiffness and damping provided by open-loop co-activation of the trunk musculature may be sufficient to counteract the perturbations and stabilize the trunk [24,31]. However, for larger, transient perturbations experienced during sitting (*dynamic sitting*), direction-specific, closed-loop muscle activation is required to stabilize the trunk [31,32].

2.2.2 Muscles Contributing to Trunk Stability and Control During Sitting

Several superficial muscles of the trunk and upper legs are known to contribute to trunk stability and its control during sitting. Trunk muscles that *flex* the trunk and significantly contribute to its stability and control include the rectus abdominis (*RA*) [33–36] as well as the external (*ExO*) and internal oblique (*IO*) [33–38]. Activation of *RA*, *ExO*, or *IO* causes *flexion* or resists *extension* of the trunk [39]. Additionally, activation of *ExO* or *IO* allows the trunk to *side bend* and *axially rotate* [39]. Trunk muscles that *extend* the trunk and significantly contribute to its stability and control include the erector spinae (*ES*) [39]. Activation of *ES* causes extension or resists flexion of the trunk. In particular, *ES* is used to stabilize the trunk against continuous gravitational forces that tend to flex the trunk due to the anterior location of its center of mass [40,41]. In addition to the described trunk flexors (i.e., *RA*, *ExO*, and *IO*) and extensors (i.e., *ES*), several other muscles of the trunk and upper legs are known to contribute to trunk stability and control. The latissimus dorsi (*LD*), although primarily responsible for arm movement at the shoulder [39], also contributes to side bending of the trunk [39]. Finally, the rectus femoris and biceps femoris indirectly contribute to trunk stability and control by stabilizing the pelvis via hip flexion [42–46] and extension [42,43,47,48], respectively.

2.2.3 Trunk Impairment in Individuals with Spinal Cord Injury

As described earlier (*see Section 1.1*), the ability to stabilize the trunk is a requirement for general human function and mobility. This is evident in individuals with impairment of trunk function resulting from spinal cord injury, as they are often unable to control seated balance on their own [4–6]. The inability of affected individuals to control seated balance is due to their complete or partial loss of active control of their trunk and upper leg muscles (*see Sections 2.2.1 and 2.2.2*). Such active control is critical considering, for example, the previously described role of *ES* in stabilizing the trunk against gravity (*see Section 2.2.2*): individuals with spinal cord injury and loss of active control of *ES* are unable to resist gravitational flexion of the trunk, which is required for maintaining seated balance [49].

The degree of trunk function impairment resulting from spinal cord injury is significantly influenced by both the *location* and *severity* of injury. The severity of injury can be broadly categorized into *complete* and *incomplete* spinal cord injury [50]. Complete spinal cord injury is characterized by complete or nearly complete loss of neural connectivity between the central and peripheral nervous systems, resulting in complete or nearly complete loss of active control of the muscles below the location of injury on the spinal cord [51]. Incomplete spinal cord injury results in only a partial loss of that neural connectivity, allowing some active control of the muscles below the location of injury to be retained [51,52].

As a consequence of their impaired ability to stabilize the trunk with the muscles of the trunk and upper legs, individuals with spinal cord injury often compensate by using innervated, non-postural muscles (e.g., shoulder and neck muscles) to control seated balance [53]. Additionally, to avoid gravitational flexion of the trunk, individuals with spinal cord injury often tilt their pelvis posteriorly, resulting in a posterior shift of the trunk's center of mass [54]. These compensatory strategies often lead to secondary health conditions such as kyphosis [55], pressure sores [24], reduced respiratory capacity [24], and shoulder pain [56]. These health conditions are primarily caused by non-physiological use of innervated muscles to control seated balance, as well as sub-optimal spinal posture and weight distribution during sitting.

2.2.4 Paradigms for Studying Trunk Stability and Control During Dynamic Sitting

Paradigms that have been used to elicit dynamic trunk perturbations commonly experienced in daily life during sitting include: *unstable* sitting and *perturbed* sitting via the exposure to externally applied or released trunk forces or external displacement of the support surface. In perturbed sitting studies, the participant was in a seated, restrained semi-seated, or restrained standing posture. In restrained semi-seated and standing postures, the pelvis and lower limbs were restrained. Thus, these postures were biomechanically equivalent to a seated one, since postural adjustments through the hip, knee, and ankle joints were prevented and movement was isolated to the trunk.

2.2.4.1 Unstable Sitting Paradigm

In unstable sitting studies, the sitting surface base was able to angularly displace freely in the frontal and/or sagittal planes about a central pivot. Deviations from the neutral position (i.e., where the unstable sitting surface-human system center of mass was directly above the central pivot) produced destabilizing gravitational moments, necessitating a postural adjustment to reposition the center of mass over the central pivot [14]. Several types of bases have been used in unstable sitting studies, including: a central ball bearing [16,17]; a central ball-and-socket and spring [14,15,19,57–65]; and hemispherical bases [18,66–90]. Unstable sitting surfaces with hemispherical bases are called *wobble boards*. The balancing difficulty on an unstable sitting surface with a central ball-and-socket and spring base was controlled by adjusting the spring stiffness or the radial distance between the springs and the central ball-and-socket; or with a hemispherical base was controlled by adjusting the radius of curvature of the hemisphere. In the majority of unstable sitting studies, the sitting surface base was able to angularly displace freely in both the frontal and sagittal planes; however, some studies restricted its motion to either the frontal [19,68,73,78–80,90] or sagittal [16,17,59,79,85] plane.

2.2.4.2 Perturbed Sitting: External Trunk Force Paradigm

In studies that perturbed the trunk by applying a force to it, dynamic perturbations commonly experienced in daily life during sitting were elicited using rapid and brief, horizontally directed applied forces. The trunk was perturbed in the direction of the applied force (e.g., trunk flexion via an anteriorly directed applied force). The applied forces were executed with control of either the amplitude of the applied force (*force control*) or the position of the trunk at the point of force application (*position control*). Methods that were used for force application include added weights, reciprocating levers, manual rope pulls, pendulums, pneumatic cylinders, as well as linear and rotary servomotors. Pneumatic cylinders and servomotors could apply forces with either force or position control and this with arbitrary force or position profiles in time. The other methods for force application could apply forces with only force control and this with one particular force profile (*see below*). Applied forces with step [37,91–110], Gaussian [12,24,31,82,111–115], sinusoidal [116–121], and randomized [32,122–129] force or position profiles have been used.

In added weight studies, a weight was added to a cable attached to a harness worn over the trunk of the participant [37,91–100,102,104–110]. The applied force had a step profile and its amplitude was controlled by adjusting the added weight. In reciprocating lever studies, an electric motor-driven lever was attached to a spring that was in series with a cable attached to a trunk harness [116–118]. The applied force had a sinusoidal profile and its amplitude was controlled by adjusting the lever displacement or the spring stiffness. In manual rope pull studies, a researcher performed a pull of a rope attached to a trunk harness [31,111–113]. The applied force had a Gaussian profile and its amplitude was controlled by adjusting the pulling force. In pendulum studies, the free end of a pendulum was attached to a cable attached to a trunk harness [114,115]. The pendulum arm was released by a researcher and swung down and away from the participant, applying a force to the trunk at the instant the pendulum arm reached vertical and the cable became taut. The applied force had a Gaussian profile and its amplitude was controlled by adjusting the pendulum mass [114] or its distribution along the pendulum arm [115]. Finally, in pneumatic cylinder [82] or servomotor [12,24,32,101,103,119–129] studies, linear motion generated by a pneumatic cylinder or servomotor was transmitted to the trunk by a rod [32,101,103,127–129] or cable [12,24,82,122–126] attached to a trunk harness, or by physical contact between the pneumatic cylinder or servomotor and the participant [119–121].

In studies that perturbed the trunk by releasing a force attached to it, dynamic perturbations commonly experienced in daily life during sitting were elicited by applying and releasing isometric trunk exertions [76,130–139]. Isometric trunk exertion was applied through a horizontal cable attached to a trunk harness. The cable was released from the trunk harness after a target cable force was reached, producing sudden unloading and resulting in perturbation of the trunk in the opposite direction of the released force (e.g., trunk flexion via a posteriorly directed released force).

2.2.4.3 Perturbed Sitting: External Support Surface Displacement Paradigm

In studies that perturbed the trunk by externally displacing the support surface, dynamic perturbations commonly experienced in daily life during sitting were elicited using rapid and brief support surface translations [140–148] or rotations [144,149] with ramp profiles. The trunk was perturbed in the opposite direction of support surface displacement (e.g., trunk flexion via either posterior translation or toe-up rotation). Support surface displacement was actuated by a researcher [149], a set of two linear servomotors [144], or a set of six hydraulic cylinders [140–143,145–148]. Support surface displacement via actuation by a researcher was limited to rotation about a single axis; and via actuation by a set of two linear servomotors was limited to either translation along, or rotation about, a single axis. Conversely, arbitrary displacement was possible via actuation by a set of six hydraulic cylinders.

2.2.5 Non-Impaired Trunk Stability and Control During Dynamic Sitting

Non-impaired trunk stability and control have been studied in the previously described dynamic sitting paradigms (*see Section 2.2.4*).

2.2.5.1 Non-Impaired Trunk Stability and Control During Unstable Sitting

Trunk stability and control during unstable sitting have been commonly quantified using time- and frequency-domain as well as stabilogram-diffusion analyses based on body or base of support angular displacement [14,17,19,65,72–74,79,150] or center of pressure displacement [65,74,81,87,89]. Time- and frequency-domain analyses provided summary statistics of displacement such as its mean velocity or mean frequency [151]. Stabilogram-diffusion analyses quantified the neuromuscular mechanisms underlying trunk control by assuming the process of stabilizing the trunk was stochastic and therefore could be modelled as a fractional Brownian motion [152]. Using time- and frequency-domain analyses, it was suggested that stabilizing the trunk was more challenging in the frontal than in the sagittal plane [79,150], and that trunk control declined for increased balancing difficulty [19,65,87,89]. Using stabilogram-diffusion analyses, a two-part control mechanism was suggested: open-loop control implying no neural feedback over short time intervals, and closed-loop control implying the presence of neural feedback over longer time intervals [81,87,89,90]. Additionally, the sensory feedback used in such closed-loop control of unstable sitting appeared to be re-weighted relative to quiet sitting: vestibular and visual channels were up-weighted whereas proprioceptive and somatosensory channels were down-weighted [73].

2.2.5.2 *Non-Impaired Trunk Stability and Control During Perturbed Sitting*

Studies have characterized the kinematic and muscle (electrical activity) responses of the trunk during perturbed sitting. Peak trunk kinematics were larger following forces applied diagonally compared to along the anterior-posterior or medial-lateral directions, suggesting the trunk was less stable in the diagonal directions [111]. The direction-specific responses of the trunk muscles have been quantified following multidirectional applied [31] and released [138] forces, as well as translation [146] and rotation [149] of the support surface. The response of the trunk muscles was the same following either anterior translation or toe-up rotation of the support surface, suggesting that somatosensory feedback, derived from backward rotation of the pelvis, initiated postural adjustments following support surface displacement [144]. In support of this, the response of the trunk muscles was the same following rotation of the support surface with or without occlusion of vision [149].

The effect of increased trunk stiffness, via increased co-activation of the trunk musculature, on the kinematic and muscle responses of the trunk during perturbed sitting has been studied. Techniques that have been used to increase trunk muscle co-activation include voluntary co-activation [37,97,100,132], predictability of perturbation [105,109,140,148], and isometric trunk exertion [91,99,104,118,136]. Peak trunk kinematics were smaller following applied forces with higher levels of co-activation of the trunk musculature [37,91,97,99,100,104,105,109]. Additionally, higher levels of trunk muscle co-activation reduced the magnitude, and delayed the onset of, the reflex response of the trunk muscles, suggesting that increased trunk stiffness reduced the need for postural adjustments to stabilize the trunk following perturbations [37,92,97,108,109].

Studies have accurately predicted the kinematic and muscle responses of the trunk during perturbed sitting. The direction-specific linear displacement of the trunk following multidirectional applied forces was accurately modelled using an applied force-based prediction [24,32,101,116,123,124]. Additionally, linear trunk displacement following anteriorly directed applied forces was accurately modelled using an applied force and trunk kinematics-based prediction [119,120,123,124]. The direction-specific responses of *RA*, *ExO*, *IO*, and *ES* following multidirectional applied forces were accurately modelled using direction of applied force-based predictions [31]. Additionally, their responses were accurately modelled, in several directions for each muscle, using trunk kinematics-based predictions [112]. Finally, the response of *ES* following anteriorly directed applied forces was accurately modelled using an applied force-based prediction [114] as well as an applied force and trunk kinematics-based prediction [119,120].

In the context of identifying the parameters in the previously described prediction models, studies have quantified intrinsic and reflex properties of the trunk. Multidirectional intrinsic translational (rotational) trunk stiffness and damping (i.e., due to open-loop co-activation of the trunk musculature, intraabdominal pressure, and mechanical properties of the spine, muscles, and connective tissue) have been identified using applied force and trunk kinematics in combination with an intrinsic translational (rotational) model of a mass-spring-damper (MSD) system [24]. To prevent eliciting closed-loop control mechanisms, the trunk was perturbed with gentle forces. Intrinsic trunk stiffness and damping were roughly symmetrical between the two body sides. Moreover, both quantities were smallest in the anterior and largest in the medial-lateral directions. Effective trunk stiffness and damping (i.e., the combined behavior of intrinsic and reflex stiffness and damping) have been identified using larger applied forces that elicited closed-loop control mechanisms; multidirectional effective translational trunk stiffness and damping were identified using applied force and trunk kinematics in combination with an effective translational model of a MSD system [116,123,124]. Effective trunk stiffness and damping varied with direction and were larger for higher levels of co-activation of the trunk musculature. Finally, intrinsic translational stiffness and damping as well as reflex properties of the trunk in the anterior direction have been identified simultaneously using applied force and trunk kinematics in combination with intrinsic translational MSD and reflex dynamics models [32,119,120].

2.3 Human Movement Kinematics

2.3.1 Introduction

The kinematic analysis of human movement produces a quantitative description of segmental (i.e., the motion of body segments) and joint (i.e., the relative motion between adjacent body segments) motion [153]. A quantitative description of segmental and joint motion is obtained by recording the three-dimensional motion of the segments of interest, followed by the calculation of segmental and joint kinematics such as instantaneous linear and angular positions, velocities, and accelerations [153].

Technologies that can be used to record the three-dimensional motion of body segments include electromagnetic tracking [154–156], inertial sensors [157–162], markerless [163–165] and marker-based [166,167] optoelectronic stereophotogrammetry, and stereoradiography [168]. The gold-standard and most common technique in human movement research is marker-based stereophotogrammetry, since it is the most accurate and reliable way of recording the motion of body segments [167]. However, inertial sensors and markerless stereophotogrammetry are becoming increasingly common, since they offer lower costs and greater usability [157,164,169]. Nevertheless, they are still less accurate and reliable than marker-based stereophotogrammetry [165,169,170].

Marker-based stereophotogrammetric systems reconstruct three-dimensional landmark coordinates from photographs [171], radiographs [172,173], or video images [174]. Video-based systems (termed *motion capture* systems) are the most common type in human movement research, since they offer the lowest financial cost and highest time efficiency [175].

2.3.2 Kinematic Data Acquisition

To record the motion of a body segment using a motion capture system, at least three markers are placed on the skin above the segment, and their instantaneous three-dimensional linear positions relative to a laboratory coordinate system (termed *global* coordinate system (*GCS*)) are measured by a set of motion capture cameras [167]. Markers are placed individually (generally on bony anatomical landmarks) [111,176–179] or in clusters of at least three markers [111,180] and according to the kinematic model used (*see Section 2.3.3*). Since a marker must be visible to at least two cameras for its position to be reconstructed (i.e., not occluded), use of more than two cameras is recommended [181]. Additionally, often more than three markers are used for a given segment [111,166,182], to increase the robustness of acquired data when samples of data are lost due to one or more markers being occluded.

Motion capture systems use either *light-emitting* or *retroreflective* markers for recording the motion of body segments. Light-emitting markers emit pulsating infrared light via light-emitting diodes. Individual markers are identified by the motion capture system based on their unique light pulse frequency [175]. Conversely, retroreflective markers are illuminated by infrared light via light-emitting diodes mounted around the lens of each camera [183,184]. Individual markers are identified using dedicated hardware circuits or pattern recognition algorithms [183,184]. Higher accuracy in reconstructing three-dimensional marker positions as well as higher possible sampling frequencies are advantages of light-emitting in comparison to retroreflective marker systems; however, an advantage of retroreflective marker systems is the absence of batteries, electronic circuits, and wires on the bodies of study participants as in light-emitting marker systems [175,185].

To reconstruct three-dimensional linear marker positions, calibration information and two-dimensional marker coordinates from each camera are used to triangulate each marker's three-dimensional position [181].

Common sources of error in motion capture measurements include: electronic noise, imprecision in marker digitization, marker imaged shape distortion [175,181], incorrect camera set-up and calibration [175], inaccuracy in identifying anatomical landmarks [186–188], and soft tissue movement [189]. Imprecision in marker digitization is imprecision in the process of converting marker images into their two-dimensional coordinates and two-dimensional coordinates into their numerical values [175,181]; marker imaged shape distortion can result from velocity effects and obscured marker images [175,181]; incorrect camera set-up can introduce optical distortion, and camera calibration determines their geometric and optical characteristics as well as their position and orientation relative to the laboratory [175]; accurate identification of anatomical landmarks depends on the skill of the researcher, palpitation procedure used, and marker shape [186–188]; and soft tissue movement occurs due to marker and skin moving together relative to underlying bony anatomical landmarks [189].

2.3.3 Kinematic Models

Segmental and joint kinematics are obtained from motion data via a mathematical model of a chain of body segments (termed *kinematic model*). There can be variability in the complexity (i.e., the number of body segments used) of the kinematic models available to describe the motion of a particular body part [111,176,177,179,180]. For example, trunk motion can be modelled using a single segment (i.e., the simplest or least complex model): all the body parts between the hip and the base of the neck, except the upper limbs, are assumed to be a single rigid body (i.e., a single segment) [166]. Single-segment trunk models can only describe the motion of the entire trunk [178,190]. However, more complex models can be used that divide the trunk into two [167,191] or more [192,193] segments. Multi-segment trunk models can describe, for example, the relative motion between adjacent spinal joint centers [192,193]. An advantage of single-segment in comparison to multi-segment trunk models is they require only three to four markers to record the motion of the trunk. However, their accuracy in representing actual trunk motion is limited by ignoring relative motion between different levels of the trunk [194]. By using more complex trunk models, accuracy in representing actual trunk motion is increased [167,192,193]. However, the computational cost of calculating segmental and joint kinematics increases with model complexity. In contrast to the trunk, some body parts are generally modelled as a single rigid body (e.g., the pelvis). Nevertheless, there can be variability in marker placement between the single-segment models available to describe the motion of a particular body part [179,187,195].

2.3.4 Segmental Kinematics

The following analysis demonstrates how the instantaneous segmental kinematics (i.e., linear and angular positions, velocities and accelerations) of the trunk are calculated from its motion data and recommended single-segment kinematic model [178].

The segment coordinate system of the trunk (*SCS*) is defined using the data of four markers placed on the following trunk landmarks: the seventh cervical vertebra (*C7*), the eighth thoracic vertebra (*T8*), the deepest point of the incisura jugularis (*IJ*), and the processus xiphoideus (*PX*). The x, y, and z axes defining *SCS* are calculated using the following equations. The x axis is calculated using:

$$x = \frac{\left(C7 - 0.5(T8 + PX)\right) \times \left(IJ - 0.5(T8 + PX)\right)}{\left\|\left(C7 - 0.5(T8 + PX)\right) \times \left(IJ - 0.5(T8 + PX)\right)\right\|} \tag{2.1}$$

The z axis is calculated using:

$$z = \frac{0.5(C7 + IJ) - 0.5(T8 + PX)}{\|0.5(C7 + IJ) - 0.5(T8 + PX)\|} \tag{2.2}$$

Finally, the *y* axis is calculated using:

$$y = z \times x \tag{2.3}$$

The origin of *SCS* (i.e., the linear position of the trunk) is coincident with *IJ*. The rotation matrix *R* capturing the orientation of *SCS* relative to *GCS* is calculated using [196]:

$$R = \begin{bmatrix} x_1 & y_1 & z_1 \\ x_2 & y_2 & z_2 \\ x_3 & y_3 & z_3 \end{bmatrix} \tag{2.4}$$

The three-dimensional angles of the trunk are calculated by composing the overall rotation from *GCS* to *SCS* as an ordered sequence of three elemental rotations (i.e., rotations about the axes of a coordinate system). The preferred sequence for calculating segmental and joint angles in humans in general is *x–y–z* by angles of flexion/extension (*F/E*) – lateral bending (*LB*) – axial rotation (*Rot*) about the rotating axes of *SCS* [197]. This sequence is equivalent to the sequence *z–y–x* by angles of *Rot* – *LB* – *F/E* about the fixed axes of *GCS*. The rotation matrix *R*, written as a product of the elemental rotation matrices $R_x(F/E)$, $R_y(LB)$, and $R_z(Rot)$ for the sequence *x–y–z* about the rotating axes of *SCS*, is [198]:

$$R = R_x(F/E)R_y(LB)R_z(Rot) = \begin{bmatrix} 1 & 0 & 0 \\ 0 & c_{F/E} & -s_{F/E} \\ 0 & s_{F/E} & c_{F/E} \end{bmatrix} \begin{bmatrix} c_{LB} & 0 & s_{LB} \\ 0 & 1 & 0 \\ -s_{LB} & 0 & c_{LB} \end{bmatrix} \begin{bmatrix} c_{Rot} & -s_{Rot} & 0 \\ s_{Rot} & c_{Rot} & 0 \\ 0 & 0 & 1 \end{bmatrix} \tag{2.5}$$

where, for example, $c_{F/E} = \cos(F/E)$ and $s_{F/E} = \sin(F/E)$. Multiplying out the right-hand side of Eq. (2.5) yields:

$$R = \begin{bmatrix} c_{LB}c_{Rot} & -c_{LB}s_{Rot} & s_{LB} \\ s_{F/E}s_{LB}c_{Rot} + c_{F/E}s_{Rot} & -s_{F/E}s_{LB}s_{Rot} + c_{F/E}c_{Rot} & -s_{F/E}c_{LB} \\ -c_{F/E}s_{LB}c_{Rot} + s_{F/E}s_{Rot} & c_{F/E}s_{LB}s_{Rot} + s_{F/E}c_{Rot} & c_{F/E}c_{LB} \end{bmatrix} = \begin{bmatrix} r_{11} & r_{12} & r_{13} \\ r_{21} & r_{22} & r_{23} \\ r_{31} & r_{32} & r_{33} \end{bmatrix} \tag{2.6}$$

Finally, equations for the three-dimensional angles of the trunk, derived from Eq. (2.6), are [198]:

$$\begin{gathered} LB = \operatorname{atan2}\left(r_{13}, \sqrt{r_{23}^2 + r_{33}^2}\right) \\ F/E = \operatorname{atan2}\left(-\frac{r_{23}}{c_{LB}}, \frac{r_{33}}{c_{LB}}\right) \end{gathered} \tag{2.7}$$

$$Rot = \text{atan2}\left(-\frac{r_{12}}{c_{LB}}, \frac{r_{11}}{c_{LB}}\right)$$

where atan2 is the four-quadrant inverse tangent.

Linear and angular velocities are obtained by numerically time differentiating linear and angular positions, respectively [199]. Accelerations are obtained similarly, but from velocities instead of positions [199].

2.4 Electromyography

2.4.1 Introduction

Electromyography is a technique for recording the electrical activity of skeletal muscles. It uses an instrument called an electromyograph to record the electrical activity of muscles via a pair of electrodes attached to the skin above the muscle or inserted into the muscle of interest [200]. The signals produced by electromyography, called *electromyograms*, represent the total electrical potential generated by the cells of a muscle [201]. The total electrical potential is the summation of the individual motor unit action potentials of a muscle. A motor unit is the smallest functional unit of a muscle, and is comprised of a motor neuron and a group of muscle fibers innervated by it [200]. An action potential originates when a nerve impulse reaches the synapse between a motor neuron and a muscle fiber. This triggers the motor neuron to release the neurotransmitter acetylcholine, which changes the electrochemical balance of the muscle fiber, causing an action potential to spread along it.

2.4.2 Electromyographic Data Acquisition

Electromyographs use *surface* or *intramuscular* electrodes for recording the electrical activity of muscles. Surface electrodes are attached to the skin above the muscle of interest [32], and can be used to record the activity of superficial muscles [202,203]. Conversely, intramuscular electrodes are inserted into the muscle of interest [200], and are therefore suitable for recording the activity of deep muscles [202]. They are also suitable for use when the potential is high for recording the activity of muscles adjacent to the muscle of interest (i.e., cross-talk) [204]. Surface electrodes are non-invasive and relatively inexpensive [204]; whereas intramuscular electrodes are evasive, more expensive, and may cause pain [204].

To minimize error due to electrode-skin impedance, electrode motion, electrode cable motion, and power line interference in electromyograms acquired using surface electrodes, the impedances of the skin and the electrode-skin interface above the muscle of interest should be minimized [203]. These impedances can be minimized by carefully preparing the skin [203]. Techniques for skin preparation include shaving it [205], cleansing it with alcohol [203,205], rubbing a conductive paste or gel into it [203], and removing the upper layers of the skin via abrasion with sandpaper [203,205].

To provide the highest signal to noise ratio in acquired electromyograms, electrodes are usually aligned in the direction of the muscle fibers of the muscle of interest [31]. A reference or ground electrode, usually attached to the skin above a bony prominence [202], is used to reduce error due to power line interference [203,206].

2.4.3 Electromyogram Amplitude

To define the electromyogram amplitude from a raw electromyogram, some or all of the following sequential processing steps are commonly used: [153]: (1) demeaning; (2) high-pass or band-pass filtering; (3) full-wave rectification; (4) low-pass filtering; and (5) normalization.

The electromyogram is an alternating current signal (i.e., it varies in both the positive and negative directions) and, therefore, has a mean value of zero [153,196]. However, since the raw electromyogram may have a non-zero mean value due to instrument error, it should be demeaned (i.e., by subtracting its mean value from each value of the signal) [153,196].

Error due to electrode-skin impedance, electrode motion, electrode cable motion, power line interference, cross-talk, and electrical activity of the heart may be present in the electromyogram and can be removed by high-pass [201,207–210] or band-pass [211–216] filtering it. The filters used depend on the error present. High-pass filter cut-off frequencies commonly used range from

10–60 Hz [207–209]. Band-pass filter lower and upper cut-off frequencies commonly used range from 5–25 and from 300–500 Hz [211,217–220], respectively.

Time-varying muscle activity is determined by full-wave rectifying [203,221] and then low-pass filtering [209,213,222] the electromyogram. Full-wave rectifying the electromyogram transforms it to a single (positive) polarity; each value in the full-wave rectified electromyogram is the absolute value of the corresponding value in the original electromyogram. The full-wave rectified electromyogram fluctuates with the strength of the muscle contraction (i.e., the changing amplitude of the full-wave rectified electromyogram indicates the changing activity of the muscle) [153]. Low-pass filtering the full-wave rectified electromyogram produces the linear envelope; the linear envelope follows the trend of the full-wave rectified electromyogram [153]. Low-pass filter cut-off frequencies commonly used range from 2–6 Hz [37,216,223–225].

The electromyogram is often normalized to express the time-varying muscle activity as a percentage of some reference electromyogram value. The amplitude of the electromyogram depends on electrode placement and size, superficial resistance at the electrode-skin interface, temperature, and subcutaneous tissue thickness. Therefore, normalization of the electromyogram allows for their comparison between muscles, participants, sessions, or studies. The reference electromyogram value for a participant and muscle is most commonly obtained from maximal or submaximal voluntary muscle contraction tests.

Alternative options for defining the electromyogram amplitude include calculating the root mean square amplitude or integrated electromyogram from the raw electromyogram [196].

2.5 Human Movement Kinetics

2.5.1 Introduction

The kinetic analysis of human movement produces a quantitative description of the forces and moments that cause the motion of the body [226]. When the body is in motion, the force and moment it applies to its support surface are balanced by an equal and opposite reaction force and moment applied by the support surface to the body (termed *ground reaction*). The ground reaction is equal to the algebraic summation of the mass-acceleration products of all the body parts [153]. The ground reaction can be recorded using a *force plate* embedded within the support surface [227,228].

2.5.2 Kinetic Data Acquisition

Force plates used in human movement research use either *strain gauge* or *piezoelectric* transducers for measuring the ground reaction [229]. Both transducers operate on the principle that deformation of the transducer due to an applied mechanical force produces an output voltage proportional to the applied force. The transducers differ in their respective methods used to produce the output voltage. A strain gauge transducer consists of a resistive metallic foil supported by an insulating flexible backing placed in a Wheatstone bridge electrical circuit. Deformation of the foil by an applied mechanical force changes its electrical resistance, which affects the output voltage of the circuit. A piezoelectric transducer consists of a piezoelectric material placed in an electrical circuit. Deformation of the piezoelectric material by an applied mechanical force causes an electrical charge to develop in it, which again affects the output voltage of the circuit.

Force plates used in human movement research are typically constructed with four three-component transducers, with each transducer measuring force and moment in the anterior-posterior, medial-lateral, and vertical directions [230]. One transducer is located at each corner of the force plate, since this arrangement provides the highest accuracy in measuring the applied force and moment [196]. The six output voltage signals from each transducer are converted to force and moment by applying a calibration matrix to the signals. Each component of the resultant force and moment (i.e., the overall force and moment measured by the force plate) is the algebraic summation of the corresponding component of force and moment measured by each transducer. The overall force and moment measured by the force plate is the reaction to all the forces and moments applied to it. The center of pressure is calculated using the overall force and the force measured by each transducer.

Common sources of error in force plate measurements include: electronic noise, transducer deformation due to temperature changes [230,231], and piezoelectric material charge leakage

[231]. Changes in temperature cause the metallic foil (piezoelectric material) in a strain gauge (piezoelectric) transducer to deform, which changes the output voltage of the transducer. There are methods available to compensate for temperature effects in both strain gauge [232] and piezoelectric [233] transducers. Electrical charge developed in the piezoelectric material in a piezoelectric transducer has a tendency to leak to the surrounding environment, which changes the output voltage of the transducer. There are again methods available to compensate for charge leakage in piezoelectric transducers [234].

Chapter 3

3 Kinematics Recommendation for Trunk Control Assessments During Unstable Sitting

The material presented in this chapter is currently in press as the article:

Roberts BWR, Vette AH. A kinematics recommendation for trunk stability and control assessments during unstable sitting. Medical Engineering & Physics.

The content of this chapter is identical to the material presented in the submitted manuscript except for the text formatting which was done according to University of Alberta requirements. Parts of this work have also been presented at scientific conferences including *The XXVII Congress of the International Society of Biomechanics*, in conjunction with *The 43rd Annual Meeting of the American Society of Biomechanics*, held on July 31 to August 4, 2019, in Calgary, Canada.

3.1 Abstract

Trunk control has been commonly studied via an unstable sitting paradigm, with the majority of analyses using angular kinematics-based, posturographic measures. However, considerable variability in the choice of kinematics exists. Furthermore, the kinematics capturing the completion of this task are unknown. The purpose of this study was to characterize the kinematics in unstable sitting by quantifying and comparing the angular motion of the base of support, pelvis, and trunk as elicited via a commonly used wobble board (WB) paradigm. WB, pelvis, and trunk motion was recorded in fifteen non-disabled participants sitting on a wobble board. Posturographic measures were calculated and compared between corresponding WB and pelvis, and between WB and trunk angles. The trunk was stabilized through relatively large WB motion, with the trunk adopting a quasi-static pose. For all measures, angles, and conditions, the WB measure values were significantly larger than their corresponding pelvis or trunk values. Our findings demonstrate that

the WB-human system is stabilized by regulating WB motion. Future work utilizing an unstable sitting surface and kinematics-based analyses to investigate trunk control should include the analysis of base of support kinematics.

3.2 Introduction

Considering that trunk stability is of general importance in human balance control and mobility, it comes as no surprise that it is critical for maintaining stability of the body during sitting [3]. Trunk stability and its control have been commonly studied via an unstable sitting paradigm, where an unstable surface serves as the base of support (BoS). Using, for example, a wobble board, such studies have investigated: differences in trunk control between different populations [15–18,72,88,90]; the effect of applied trunk forces [14], whole body vibration [60], or sensory manipulation [73] on trunk control; and methodological choices, e.g., task difficulty and kinematic outcome measures, that can optimize trunk control assessments and their reliability [19,57,62,73,74].

While the majority of analyses have focused on the use of angular kinematics-based, posturographic measures, considerable variability in the choice of kinematics exists. Kinematics used include those of the: BoS [14–16,19,57,60,62]; pelvis [15,72,74]; pelvis relative to the BoS [16]; lumbar spine relative to the BoS [17]; lumbar spine relative to the pelvis [16]; thoracic spine [15,73,74]; thoracic spine relative to the pelvis [15,72,74,90]; thoracic spine relative to the lumbar spine [18,88]; and thoracolumbar spine relative to the BoS [19]. This comes as no surprise as no study to date has actually investigated the kinematics capturing task completion in unstable sitting. An understanding of the kinematics important for assessing trunk control during unstable sitting could be valuable for recommending the kinematics to be measured in future research and assessments pertaining to unstable sitting.

The purpose of this study was therefore to characterize the kinematics in unstable sitting by quantifying and comparing the angular motion of the base of support, pelvis, and trunk as elicited via a wobble board paradigm. Based on a biomechanical assessment of unstable sitting, we hypothesized that the task is completed by adopting a quasi-static pose of the upper body while regulating the motion of the base of support.

3.3 Methods

3.3.1 Participants and Experimental Procedures

Fifteen non-disabled, young and male individuals were invited to participate in this study (age 25 ± 5.2 years; height 179.6 ± 6.7 cm; and weight 75.1 ± 13.0 kg; mean ± standard deviation). All participants reported no history of neurological or musculoskeletal impairments or pain, gait or balance difficulties, or use of a walking aid. All participants gave written informed consent to the experimental procedures, which were approved by the Health Research Ethics Board of the University of Alberta (Study ID: Pro00039437).

Participants were asked to sit on a custom-made wobble board (Figure 3.1A) with their sagittal plane aligned with the anterior-posterior axis of the wobble board as defined via four motion capture markers (Figure 3.1B). The wobble board, which is described elsewhere [235], was used to induce unstable sitting as elicited by its challenging postural environment. Hemispherical bases of different radii of curvature could be attached to the bottom of the sitting surface to allow for different levels of instability. For each participant, four 35 second trials were performed for each of two task conditions: (1) an easier base and eyes closed (B1EC; radius of curvature: 20 cm); and (2) a more difficult base and eyes open (B2EO; radius of curvature: 13 cm). We specifically included two task conditions to improve the validity of our findings, not to compare kinematics across task conditions. Each task condition had a different base and eye condition as modifying task difficulty is common in studies focused on kinematics-based analyses and unstable sitting paradigms [14,15,18,19,57,60,62,72,73]. To reduce potential learning effects, each participant performed one 60 second practice trial for each task condition. A resting break of 30 seconds was given in between trials.

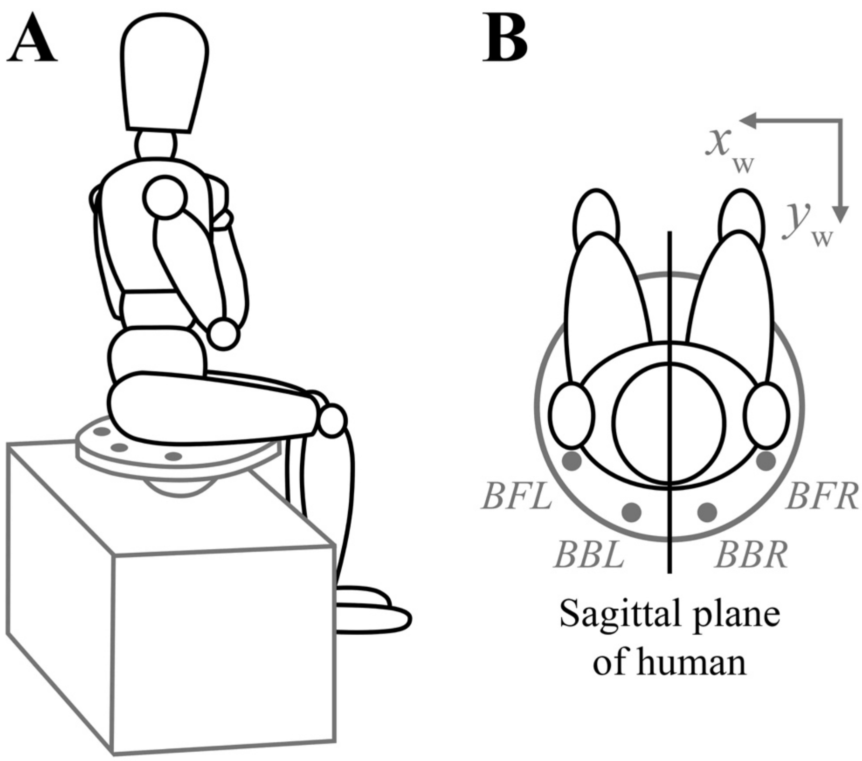

Figure 3.1: Schematic of wobble board balancing (A); and aerial view of wobble board-human system (B), with the following markers attached: board front left (*BFL*), board back left (*BBL*), board back right (*BBR*), and board front right (*BFR*). In (B), the orientation of the local coordinate system of the wobble board relative to the sagittal plane of the participant is shown. Specifically, the y axis of the wobble board (y_w) was aligned with the sagittal plane of the participant.

Kinematic data of the wobble board, pelvis, and thoracic spine (hereafter referred to as *trunk*) were recorded at a sampling rate of 100 Hz using an eight-camera motion capture system (Eagle Digital Camera, Motion Analysis, Santa Rosa, California, USA). In addition to the four markers placed on the wobble board (Figure 3.1B), four markers were placed on the following pelvis landmarks [236]: bilaterally on the anterior superior iliac spine and posterior superior iliac spine. Four markers were also placed on the following trunk landmarks [178]: the seventh cervical vertebra, the eighth thoracic vertebra, the deepest point of the incisura jugularis, and the processus xiphoideus. For subsequent analyses, a 30 second segment [57], starting 1 second into each trial, was isolated in each trial's motion data. Missing motion capture markers of four or less consecutive frames [237] were recreated using spline interpolation [238]. Following interpolation, trials still affected by missing data were removed from subsequent analyses.

3.3.2 Experimental Data Processing and Analysis

To obtain the kinematics of the wobble board, pelvis, and trunk for each trial (all relative to the global coordinate system (*GCS*)), the coordinate systems of the wobble board (*WCS*), pelvis (*PCS*) [236], and trunk (*TCS*) [178] were defined using the raw marker data. The rotation matrices from *GCS* to *WCS*, R_w, from *GCS* to *PCS*, R_p, and from *GCS* to *TCS*, R_t, were identified according to [196]. The three-dimensional angles of the wobble board, pelvis, and trunk were extracted from R_w, R_p, and R_t, respectively, using a Cardan rotation sequence: flexion/extension (*F/E*) – lateral bending (*LB*) – axial rotation (*Rot*) about the moving axes of *WCS*, *PCS*, and *TCS*, respectively, according to [198]. Only *F/E* and *LB* were used in subsequent analyses as the wobble board does not induce substantial perturbations in the axial rotation direction. The obtained kinematic time series were first filtered using a zero phase-shift, fourth-order low-pass Butterworth filter with a cut-off frequency of 2.5 Hz [18], and then demeaned.

To quantify and compare the motion of the wobble board, pelvis, and trunk during the balancing task, three posturographic time-domain measures were calculated for each kinematic time series: the range of the angle (*RANGE*), root mean square of the angle (*RMS*), and mean of the absolute angular velocity (*MVELO*) [151]. These measures, which capture the range, variance, and mean speed of an angle, respectively, were chosen as they are commonly used in kinematics-based analyses and unstable sitting paradigms when investigating trunk stability and its control [14–16,18,19,57,60,62,73,74,88]. A two-tailed, paired *t*-test was used to assess, for a given measure and condition, whether significant differences exist between corresponding wobble board and pelvis kinematics (e.g., wobble board *F/E* and pelvis *F/E*) and corresponding wobble board and trunk kinematics (e.g., wobble board *LB* and trunk *LB*). We applied Bonferroni corrections in all our comparisons and used a statistical significance level of $\alpha = 0.05$. All dependent variables obeyed a normal distribution, as tested by a Kolmogorov-Smirnov test [239]. Details on the experimental data analysis are provided in *Appendix A*.

3.4 Results

In Figure 3.2, representative examples of *F/E* versus *LB* for wobble board, pelvis, and trunk kinematics for the B1EC (A, B, and C) and B2EO conditions (D, E, and F) are shown for a single participant. A visual inspection suggests that the pelvis and trunk remained relatively stationary, whereas wobble board *F/E* and *LB* were comparably variable during the balancing task.

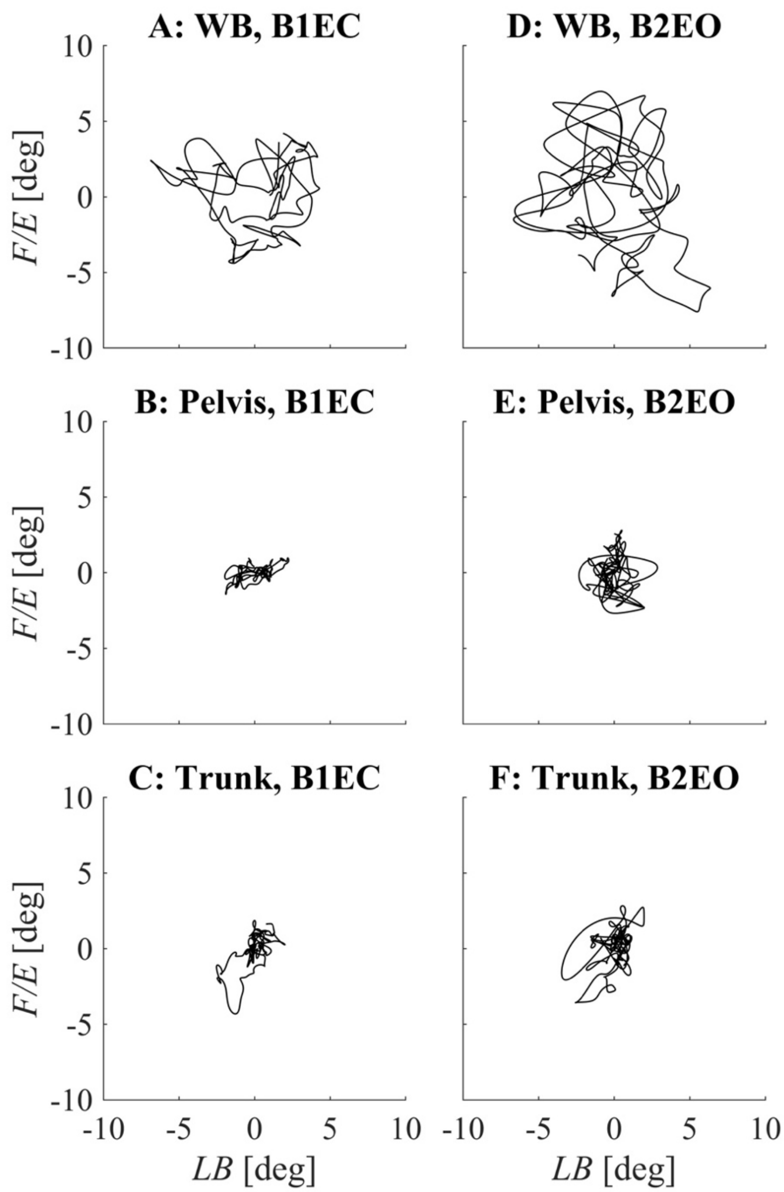

Figure 3.2: Representative examples of flexion/extension (*F/E*) versus lateral bending (*LB*) for wobble board (WB), pelvis, and trunk kinematics for a single participant. A, B, and C: Planar

phase plots for the Base 1 Eyes Closed condition (B1EC); D, E, and F: Planar phase plots for the Base 2 Eyes Open condition (B2EO).

In Figure 3.3, group *RANGE*, *RMS*, and *MVELO* values (mean and one standard deviation) for wobble board, pelvis, and trunk *F/E* and *LB* under B1EC and B2EO conditions are shown. For all measures, angles, and conditions, the wobble board values were significantly larger than their corresponding pelvis or trunk values (Figure 3.3), with the two-tailed, paired *t*-test revealing statistically significant differences in all 24 comparisons ($p < 1\times10^{-2}$). Comparisons with p less than 1×10^{-2}, 1×10^{-4}, or 1×10^{-6} are marked with one, two, or three asterisks, respectively (Figure 3.3). The *RANGE* and *RMS* results verify the visual inspection of Figure 3.2 where the pelvis and trunk remained relatively stationary and displaced significantly less than the wobble board during balancing. The *MVELO* results suggest that the pelvis and trunk displaced significantly slower than the wobble board during balancing. Posturographic measure and p values are tabulated in *Appendix B*.

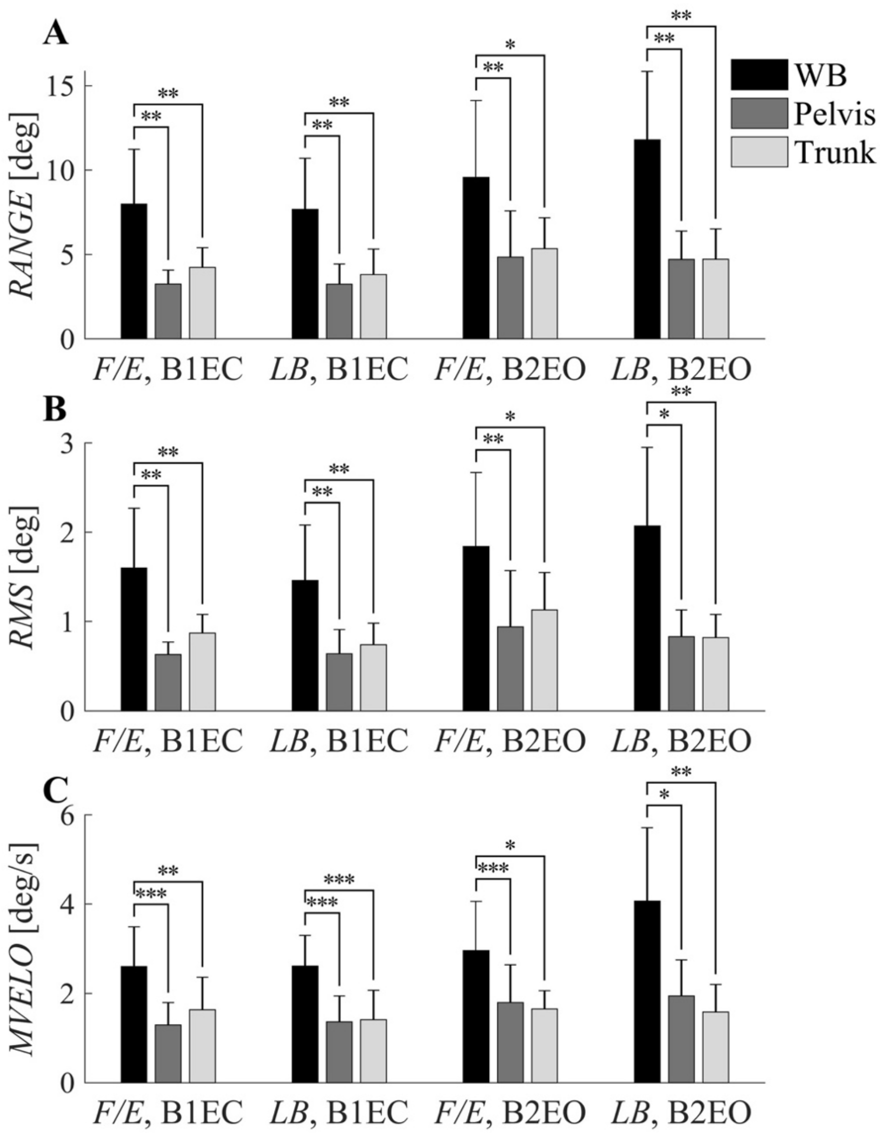

Figure 3.3: Posturographic time-domain measures for wobble board (WB), pelvis, and trunk kinematics. Shown are the range of the angle (*RANGE*) (A), root mean square of the angle (*RMS*) (B), and the mean of the absolute angular velocity (*MVELO*) (C) for flexion/extension (*F/E*) and lateral bending (*LB*) under the Base 1 Eyes Closed (B1EC) and Base 2 Eyes Open (B2EO) conditions. All values are presented as mean and one standard deviation (presented variability is *inter-participant*). A two-tailed, paired *t*-test revealed statistically significant differences between WB and pelvis kinematics and between WB and trunk kinematics for all measures, angles, and task conditions ($p < 1\times10^{-2}$; 24 comparisons). Comparisons with p less than 1×10^{-2}, 1×10^{-4}, or 1×10^{-6} are marked with one, two, or three asterisks, respectively.

3.5 Discussion

The purpose of this study was to quantify the kinematics characterizing task completion in unstable sitting. Our results show that, during unstable sitting, the trunk is stabilized through relatively large, fast displacements of the BoS, whereas both the pelvis and trunk remain relatively upright and stationary.

3.5.1 Biomechanical Insights and Practical Recommendations

The primary goal of the wobble board-human dynamic system is to stabilize the upper body. Mechanically, the wobble board was lighter, smaller, and of lower inertia compared to the upper body. Therefore, it is reasonable to assume the system is most effectively stabilized by regulating the motion of the wobble board. While this biomechanical assessment agrees with our findings, future work could investigate how the central nervous system uses sensory feedback and previous experience to decide that adopting a quasi-static pose of the upper body while regulating the motion of the base of support may be the best stabilization strategy.

In studies that have utilized an unstable sitting surface to investigate or assess trunk stability and its control, considerable variability in the choice of kinematics exists [14–19,57,60,62,72–74,88,90]. However, no study to date has investigated the kinematics characterizing task completion in unstable sitting. The finding that the task is characterized by and completed through relatively large motion of the BoS and relatively small motion of the upper body allows us to isolate the most sensitive kinematic measures in unstable sitting. We therefore propose that future research and assessments utilizing kinematics-based analyses of unstable sitting be standardized by including some variation of BoS kinematics.

3.5.2 Limitations

Since all study participants were male, we were unable to investigate potential sex differences in the unstable sitting kinematics. However, based on previous work [15,16], it can be hypothesized that similar results hold true for females. Nonetheless, future work should examine whether our findings do apply to other populations.

This study used a hemispherical base attached to the bottom of the sitting surface to induce unstable sitting. However, several types of sitting surface bases have been used in studies investigating trunk control, including: a central ball bearing [16,17]; a central ball-and-socket and spring [14,15,19,57,60,62]; and hemispherical [18,72–74,88,90] bases. These unstable sitting paradigms are all mechanically similar, with the base of support in each case able to displace freely about a central pivot. We therefore expect that our findings apply to other types of unstable sitting paradigms.

3.5.3 Conclusions

During unstable sitting, the trunk is stabilized through relatively large, fast displacements of the BoS, whereas the trunk adopts a quasi-static pose. We recommend that future studies utilizing an unstable sitting surface and kinematics-based analyses to investigate or assess trunk control should include analyses involving some variation of the BoS kinematics (i.e., BoS relative to global or trunk relative to BoS).

3.6 Acknowledgments

We would like to thank the Glenrose Rehabilitation Hospital for its in-kind support for this study. We would also like to thank Fatemeh Gholibeigian and Justin Lewicke for their contributions to experimental design and data acquisition. This study was partially funded through a Discovery Grant from the Natural Sciences and Engineering Research Council of Canada (RGPIN-2014-04666).

Chapter 4

4 Relation of Kinematics and Muscle Activity During Unstable Sitting

The material presented in this chapter is currently under review for publication as the article:

Roberts BWR, Gholibeigian F, Lewicke J, Vette AH. Spatial and temporal relation of kinematics and muscle activity during unstable sitting. Neuromodulation: Technology at the Neural Interface.

The content of this chapter is identical to the material presented in the submitted manuscript except for the text formatting which was done according to University of Alberta requirements. Parts of this work have also been presented at scientific conferences including *The XXVII Congress of the International Society of Biomechanics*, in conjunction with *The 43rd Annual Meeting of the American Society of Biomechanics*, held on July 31 to August 4, 2019, in Calgary, Canada.

4.1 Abstract

Recent work suggests that kinematics-based electrical stimulation may restore dynamic trunk stability following neuromuscular impairment. However, to ensure fatigue-resistant control, knowledge of the relation between body motion and the activity of relevant muscles during non-impaired, unstable sitting may be beneficial. Therefore, our objective was to quantify the spatial and temporal relationships between (1) characteristic angular kinematics and (2) trunk and upper leg muscle activity in unstable sitting as elicited via a wobble board. Wobble board motion and bilateral electromyograms from fourteen trunk and upper leg muscles were recorded in fifteen non-disabled participants sitting on a wobble board. The relationship between wobble board tilt and the electromyograms was quantified using cross-correlation analysis. During unstable sitting, the trunk was stabilized through direction-specific activation of the trunk and upper leg muscles, preceding wobble board displacement by 110 to 230 ms. Direction-specific activation suggests the

presence of active neural control, while preceding activation may be needed to account for known torque generation time delays. Furthermore, the findings suggest the use of stiffness control in the anterior-posterior, but not medial-lateral direction. Future work will use the gained insights in defining the muscle activation patterns of kinematics-based neuroprostheses that can restore trunk stability following impairment.

4.2 Introduction

Trunk stability is a critical prerequisite of human function and mobility, regardless of the movement or task performed. It therefore comes as no surprise that activities of daily living (ADLs), such as sitting, standing, walking, and reaching, cannot be accomplished unless the trunk is successfully stabilized [3]. In individuals who experience neuromuscular impairments affecting trunk stability and its control, the consequences are often detrimental. For example, individuals with spinal cord injury (SCI) between the head and tenth thoracic vertebra usually experience at least some trunk function impairment [4]. As a result, they are often not able to control seated balance on their own, leading to significantly reduced independence in ADLs [5,6].

Various attempts have been made to improve sitting stability in individuals with SCI during ADLs, primarily by customizing wheelchair configurations. These include modifying the wheelchair's inclination angle [7] as well as using novel types of seat cushions [10], footrests [9], or chest straps [8]. However, these modifications support the trunk only in the anterior direction and do not take dynamic demands into account that depend on the particular functional and/or environmental context. In this light, recent developments suggest that neuroprostheses utilizing functional electrical stimulation (FES) can facilitate and even restore mobility and function. For example, FES has been used in open- and closed-loop control schemes to restore reaching and grasping in individuals with SCI that present with a range of injury severities [240]. Promising results also indicate the potential of FES to assist in the stabilization of the human trunk during quiet sitting [11,12]. Under postural disturbances commonly experienced in daily life – for example, when sitting on a bus – stabilizing the trunk has, however, larger compensational demands, calling for higher overall stimulation intensities that accelerate the onset of muscle fatigue [13]. In addition, stabilizing the trunk during such dynamic sitting paradigms requires many relevant muscles to be contracted synergistically, adhering to well-defined spatial and temporal activation patterns.

To reduce or prevent FES-induced muscle fatigue, low-intensity (open-loop) FES can be applied, which has already been suggested to facilitate fatigue-resistant static trunk stability by increasing overall trunk stiffness [12]. Such low-intensity FES could be paired with intermittent, kinematics-based (closed-loop) FES that ensures dynamic trunk stability as needed for the completion of many ADLs. To define the required, kinematics-based spatial and temporal muscle activation patterns under the constraint of fatigue optimization, one approach is to mimic muscle activation patterns that non-disabled individuals use to regulate trunk stability. This, however, requires a more comprehensive understanding of the relation between (1) multi-directional motion of the trunk relative to the base of support; and (2) the associated muscle activity during non-impaired, dynamic sitting.

Based on these considerations, the overall goal of this study was to obtain a more comprehensive, quantitative understanding of the muscle activation patterns in one type of dynamic sitting, i.e., unstable sitting as elicited via a wobble board paradigm. The specific objective was to quantify both the spatial and temporal relationships between (1) the angular kinematics of the wobble board-human system and (2) the trunk and upper leg muscle activity in unstable sitting.

4.3 Methods

4.3.1 Participants

Fifteen non-disabled, young and male individuals were invited to participate in this study (age 25 ± 5.2 years; height 179.6 ± 6.7 cm; and weight 75.1 ± 13.0 kg; mean ± standard deviation). All participants reported no history of neurological or musculoskeletal impairments or pain, gait or balance difficulties, or use of a walking aid. All participants gave written informed consent to the experimental procedures, which were approved by the Health Research Ethics Board of the University of Alberta (Study ID: Pro00039437).

4.3.2 Experimental Procedures and Data Acquisition

Participants were asked to sit on a custom-made wobble board (Figure 4.1A) with their sagittal plane aligned with the anterior-posterior axis of the wobble board as defined via four motion capture markers (Figure 4.1B). The wobble board, which is described elsewhere [235], was used to induce unstable sitting as elicited by its challenging postural environment. Hemispherical bases of different radii of curvature could be attached to the bottom of the sitting surface to allow for different levels of instability. For each participant, four 35 second trials were performed for each of two task conditions: (1) an easier base and eyes closed (B1EC; radius of curvature: 20 cm); and (2) a more difficult base and eyes open (B2EO; radius of curvature: 13 cm). We specifically included two task conditions to improve the validity of our findings, not to make comparisons across task conditions. To reduce potential learning effects, each participant performed one 60 second practice trial for each task condition. A resting break of 30 seconds was given in between trials.

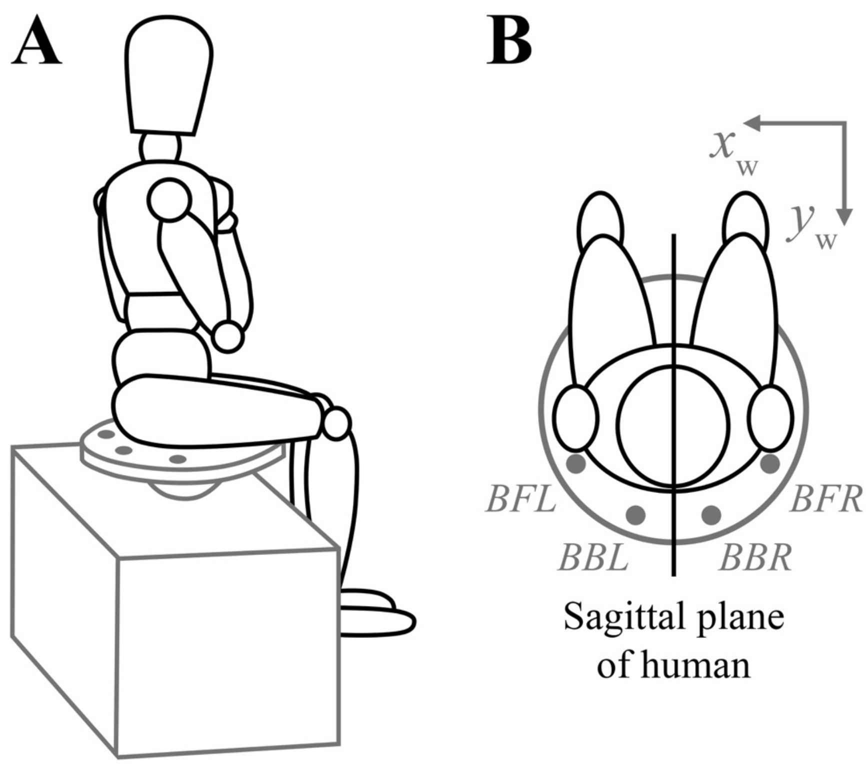

Figure 4.1: Schematic of wobble board balancing (A); and aerial view of wobble board-human system (B), with the following markers attached: board front left (*BFL*), board back left (*BBL*),

board back right (*BBR*), and board front right (*BFR*). In (B), the orientation of the local coordinate system of the wobble board relative to the sagittal plane of the participant is shown. Specifically, the y axis of the wobble board (y_w) was aligned with the sagittal plane of the participant.

Bilateral surface electromyograms (EMG) were recorded from fourteen trunk and upper leg muscles [31,241,242]. In line with [31,241,242], Bagnoli 2-bar surface EMG electrodes (Delsys Inc., Natick, Massachusetts, USA) were placed on the: (1) rectus abdominis (*RA*), 3 cm lateral of the umbilicus, aligned vertically; (2) external oblique (*ExO*), 15 cm lateral of the umbilicus, aligned at 45 degrees off the vertical; (3) latissimus dorsi (*LD*), lateral of the ninth thoracic vertebra (T9) over the muscle belly; (4) thoracic erector spinae (*TES*), 5 cm lateral of T9, aligned vertically; (5) lumbar erector spinae (*LES*), 3 cm lateral of the third lumbar vertebra, aligned vertically; (6) rectus femoris (*RF*), at 50% on the line between the anterior superior iliac spine and the superior part of the patella, aligned in the direction of the long axis of the upper leg; and (7) biceps femoris (*BF*), at 50% on the line between the ischial tuberosity and the lateral epicondyle of the tibia, aligned in the direction of the long axis of the upper leg (*see Appendix C for a complete electrode placement schematic*). Two pooled reference electrodes (Dermatrode, Delsys Inc.) were placed on the left and right olecranon. Left and right body side muscles are denoted with *L* and *R*, respectively, preceding the muscle abbreviation (e.g., *LRA* for left rectus abdominis). EMG data were amplified using a 16-channel Bagnoli EMG system (Delsys Inc.) and digitized at 1,000 Hz using a PowerLab 16/35 data acquisition system (ADInstruments, Sydney, Australia).

To capture the motion of the trunk relative to the wobble board during the unstable sitting task, kinematic data of the trunk, pelvis, and wobble board were recorded at a sampling rate of 100 Hz using an eight-camera motion capture system (Eagle Digital Camera, Motion Analysis, Santa Rosa, California, USA). However, since our previous work revealed that the trunk remains relatively upright and stationary, and is stabilized via motion of the wobble board during balancing (*see Chapter 3*), subsequent analyses focused on the wobble board kinematics only. As mentioned before, four markers were placed on the wobble board: board front left, board back left, board back right, and board front right (Figure 4.1B). EMG and kinematic data were time-synchronized using an MLA92 Push Button Switch (ADInstruments).

4.3.3 Experimental Data Processing and Analysis

After the recorded EMG time series were demeaned, rectified, and filtered using a zero phase-shift, fourth-order low-pass Butterworth filter with a cut-off frequency of 2.5 Hz [37], they were down-sampled to 100 Hz to match the sampling rate of the kinematic time series. A 30-second segment was then isolated in the EMG and motion data for each trial, starting one second after the time stamp of the push button switch. Missing motion capture marker data of four or less consecutive frames [237] were recreated using spline interpolation [238] (*note that, for all kinematic time series, the length of missing motion capture data was shorter than four frames*).

4.3.3.1 Angular Kinematics of the Wobble Board

To obtain the angular kinematics of the wobble board relative to the global coordinate system (*GCS*) for each trial, the coordinate system of the wobble board (*WCS*) was defined using the raw data of the wobble board markers. The rotation matrix from *GCS* to *WCS*, R_w, was identified according to Robertson et al. [196]. The three-dimensional angles of the wobble board were extracted from R_w using a Cardan rotation sequence: anterior-posterior tilt (*AP*) – medial-lateral tilt (*ML*) – axial rotation (*Rot*) about the moving axes of *WCS* according to Craig [198]. Only *AP* and *ML* were used in subsequent analyses as the wobble board does not induce substantial perturbations in the axial rotation direction. The obtained kinematic time series were filtered using a zero phase-shift, fourth-order low-pass Butterworth filter with a cut-off frequency of 2.5 Hz [18]. Details on how the angular kinematics of the wobble board were obtained are provided in *Appendix C*.

4.3.3.2 Cross-Correlation between Kinematics and EMG

To quantify both the spatial and temporal relationships between the angular kinematics of the wobble board and the activity of the trunk and upper leg muscles, cross-correlation analysis was used. The following steps were taken: (1) for each direction of wobble board displacement (i.e., *anterior* or *posterior* for *AP*; *left* or *right* for *ML*), a 4-second window centered at each of the three largest values (for *anterior* or *left*) or smallest values (for *posterior* or *right*) in the kinematic time series (with no overlap between the three windows) was created; (2) time-matched, corresponding 4-second windows were identified in a given muscle's EMG time series; (3) each of these segments (i.e., the 4-second window in the kinematic time series and its time-matched 4-second window in the EMG time series) was demeaned and cross-correlated; and (4) the three obtained cross-correlation functions (CCFs) for each direction were averaged for each trial. CCFs were mirrored with respect to the time lag (τ) axis for the *posterior* and *right* directions so that positive and negative correlation coefficients (r) always imply direction-dependent muscle activation and deactivation, respectively. Cross-correlations were performed such that a negative time lag implies EMG preceding the kinematics. Correlation coefficients were normalized such that +1, 0, and −1 represent perfect positive correlation, no correlation, and perfect negative correlation, respectively. The 4-second window length was chosen based on inspecting the kinematic time series' mean magnitude spectra for each of the B1EC and B2EO conditions, with the meaningful frequency content found between 0 and 3 Hz for both. The number of windows per direction (3) was chosen based on trial and window length.

To initially determine whether a positive correlation between a direction and muscle existed, mean CCFs across participants for each condition were analyzed. For a given direction-muscle pair, we assumed a positive correlation if, under at least one of the two task conditions, the maximum correlation coefficient, $r_{\max}$, of the mean CCF across trials and participants was ≥ 0.15 – the threshold at which r is statistically different from zero ($p < 0.01$, $N = 400$) [243,244]. If a direction and muscle were positively correlated, we also included the correlation between that muscle and the opposite direction, assuming a negative correlation between them.

For each positively (negatively) correlated pair and condition as determined with the mean, across-participant CCFs (*see above*), trials that did not meet all of the following were considered outliers: (1) the maximum (minimum) correlation coefficient was statistically significant (*see above*); (2) the CCF profile had one distinct peak, i.e., correlation of a direction with only activation (deactivation) of a muscle; and (3) the time lag at the maximum (minimum) correlation coefficient was not greater in magnitude than 0.3 seconds [245] and had the same sign as that of the mean CCF before removing outliers. Once outliers were removed, the mean CCF profile as well as the maximum (minimum) correlation coefficient and corresponding time lag values across participants were obtained (mean ± standard deviation). Details on the experimental data analysis are provided in *Appendix C*.

4.4 Results

In Figure 4.2, representative examples of corresponding *ML* (A) and *LExO* (B) time series are shown for the B2EO condition for a single participant. Shaded areas represent the 4-second windows centered at each of the three largest values (i.e., centered at 4.3, 14.3, and 23.5 seconds) in the *left* direction of *ML* (A) and their time-matched corresponding 4-second windows in *LExO* (B) that were cross-correlated. A visual inspection suggests that, since in all three windows *ML* and *LExO* move in the same direction, the pair may be positively correlated.

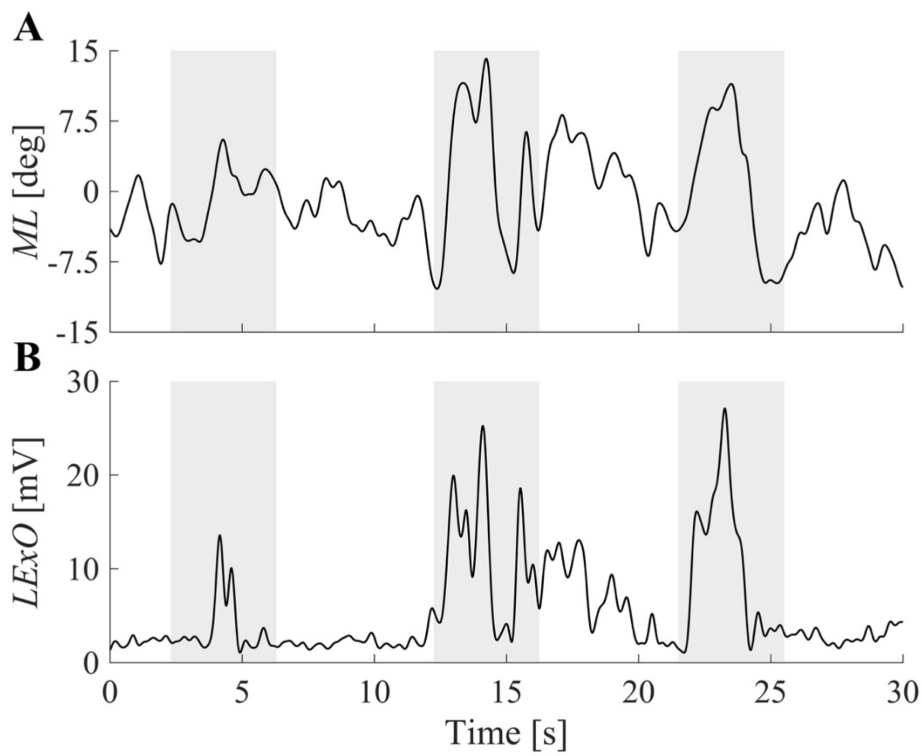

Figure 4.2: Representative time series of corresponding medial-lateral tilt (*ML*) (A) and left external oblique activity (*LExO*) (B) for the Base 2 Eyes Open condition for a single participant. The gray shaded regions mark the 4-second windows centered at each of the three largest values in the *left* direction of *ML* (A) and their time-matched, corresponding 4-second windows in *LExO* (B) that were cross-correlated.

4.4.1 Anterior-Posterior Base of Support Displacements

The cross-correlation results revealed that *anterior* and *posterior* were correlated with *RA*, *ExO*, *TES*, *LES*, *RF*, and *BF*. However, they were not correlated with *LD*. The activation and deactivation of *RA* and *BF* preceded *anterior* and *posterior*, respectively. Additionally, the activation and deactivation of *ExO*, *TES*, *LES*, and *RF* preceded *posterior* and *anterior*, respectively. Figure 4.3 depicts the mean CCFs across participants between the left body side muscles and *anterior* for the B1EC (dashed line) and B2EO (dotted line) conditions. Also shown are the mean CCFs across participants between the left body side muscles and *posterior* for the B1EC (dash-dot line) and B2EO (solid line) conditions. Mean CCFs for corresponding right body side muscles and *anterior* or *posterior* were found to be similar (*see Appendix D*). In Table 4.1, maximum or minimum correlation coefficient ($r_{\mathrm{max/min}}$) and corresponding time lag ($\tau_{\mathrm{max/min}}$) values (mean ± standard deviation) across participants for all *anterior* and *posterior* correlations under the B1EC and B2EO conditions are presented. Note that shaded and non-shaded entries for $r_{\mathrm{max/min}}$ indicate muscle activation and deactivation, respectively.

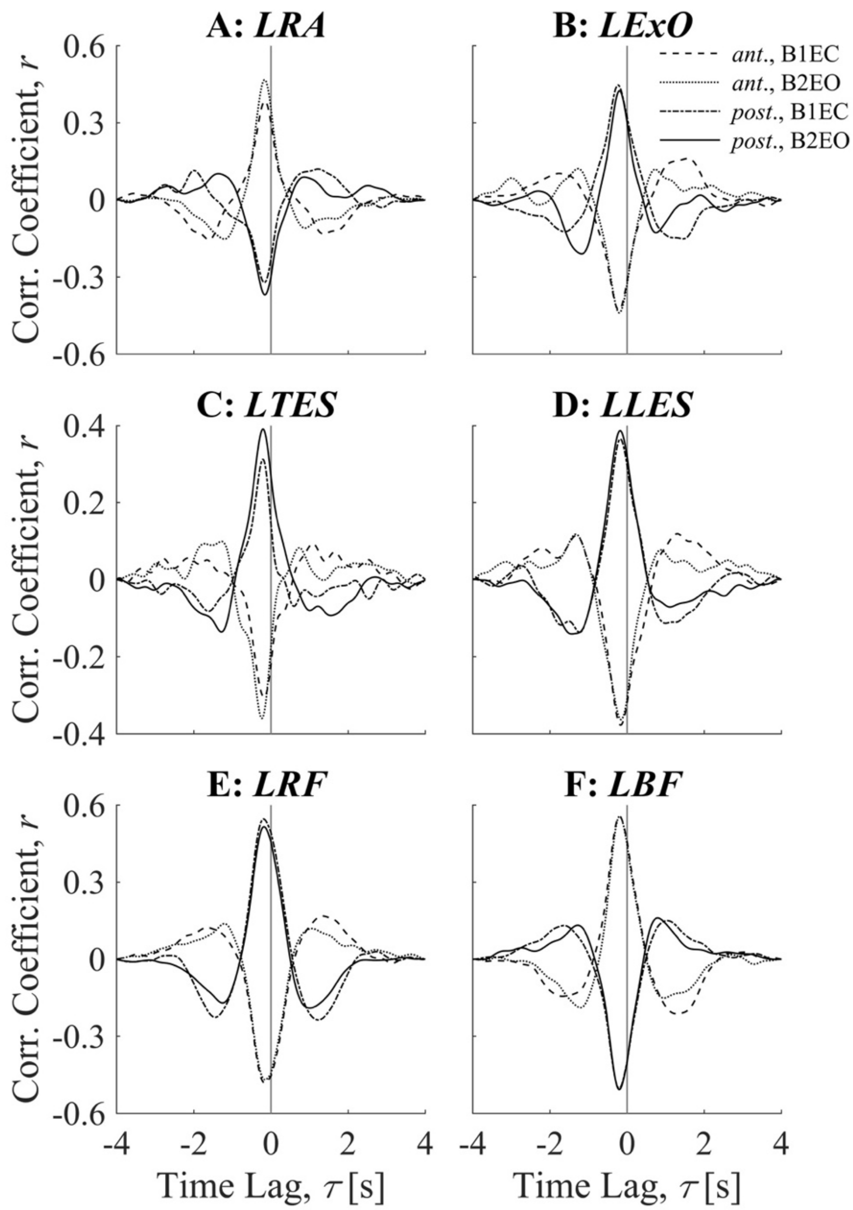

Figure 4.3: Mean cross-correlation functions across participants between left body side muscles and *anterior* for the Base 1 Eyes Closed (B1EC) (dashed line) and Base 2 Eyes Open (B2EO) (dotted line) conditions. Shown are also the mean cross-correlation functions across participants between left body side muscles and *posterior* for the B1EC (dash-dot line) and B2EO (solid line) conditions. Correlated muscles are: left rectus abdominis (*LRA*) (A), left external oblique (*LExO*) (B), left thoracic erector spinae (*LTES*) (C), left lumbar erector spinae (*LLES*) (D), left rectus femoris (*LRF*) (E), and left biceps femoris (*LBF*) (F).

Table 4.1: Maximum or minimum correlation coefficient ($r_{\text{max/min}}$) and corresponding time lag ($\tau_{\text{max/min}}$) values across participants. Shown are the values for *anterior* and *posterior* under the Base 1 Eyes Closed (B1EC) and Base 2 Eyes Open (B2EO) conditions when correlated with the activity of the following muscles: rectus abdominis (*RA*), external oblique (*ExO*), thoracic erector spinae (*TES*), lumbar erector spinae (*LES*), rectus femoris (*RF*), and biceps femoris (*BF*). Left and right body side muscles are denoted with *L* and *R*, respectively, preceding the muscle abbreviation. Shaded and non-shaded entries for $r_{\text{max/min}}$ indicate muscle activation and deactivation, respectively. Since $\tau_{\text{max/min}}$ was negative for all correlations, muscle activation and deactivation always preceded wobble board displacement. All values are presented as mean ± standard deviation (presented variability is *inter-participant*).

	Anterior				***Posterior***			
	B1EC		**B2EO**		**B1EC**		**B2EO**	
Muscle	$r_{\text{max/min}}$	$\tau_{\text{max/min}}$ [s]	$r_{\text{max/min}}$	$\tau_{\text{max/min}}$ [s]	$r_{\text{max/min}}$	$\tau_{\text{max/min}}$ [s]	$r_{\text{max/min}}$	$\tau_{\text{max/min}}$ [s]
RRA	0.40 ± 0.08	−0.17 ± 0.03	0.49 ± 0.13	−0.17 ± 0.04	−0.33 ± 0.09	−0.14 ± 0.04	−0.37 ± 0.10	−0.12 ± 0.06
LRA	0.38 ± 0.13	−0.15 ± 0.03	0.46 ± 0.12	−0.18 ± 0.04	−0.32 ± 0.08	−0.14 ± 0.06	−0.40 ± 0.11	−0.16 ± 0.05
RExO	−0.41 ± 0.11	−0.22 ± 0.09	−0.42 ± 0.10	−0.17 ± 0.10	0.38 ± 0.10	−0.21 ± 0.09	0.50 ± 0.14	−0.20 ± 0.04
LExO	−0.43 ± 0.13	−0.20 ± 0.07	−0.41 ± 0.16	−0.18 ± 0.02	0.41 ± 0.11	−0.23 ± 0.03	0.46 ± 0.14	−0.15 ± 0.10
RTES	−0.33 ± 0.09	−0.16 ± 0.06	−0.37 ± 0.10	−0.15 ± 0.09	0.38 ± 0.09	−0.18 ± 0.05	0.37 ± 0.11	−0.18 ± 0.08
LTES	−0.35 ± 0.07	−0.16 ± 0.09	−0.39 ± 0.13	−0.23 ± 0.06	0.35 ± 0.08	−0.20 ± 0.07	0.41 ± 0.11	−0.17 ± 0.08
RLES	−0.34 ± 0.09	−0.21 ± 0.08	−0.34 ± 0.07	−0.16 ± 0.06	0.36 ± 0.09	−0.19 ± 0.06	0.39 ± 0.12	−0.13 ± 0.09
LLES	−0.39 ± 0.14	−0.15 ± 0.10	−0.39 ± 0.11	−0.13 ± 0.08	0.37 ± 0.11	−0.15 ± 0.08	0.38 ± 0.12	−0.17 ± 0.07
RRF	−0.48 ± 0.09	−0.16 ± 0.08	−0.49 ± 0.11	−0.15 ± 0.08	0.49 ± 0.14	−0.20 ± 0.07	0.58 ± 0.09	−0.15 ± 0.08
LRF	−0.47 ± 0.14	−0.15 ± 0.09	−0.50 ± 0.07	−0.14 ± 0.09	0.53 ± 0.11	−0.17 ± 0.06	0.54 ± 0.11	−0.16 ± 0.06
RBF	0.57 ± 0.10	−0.18 ± 0.06	0.52 ± 0.11	−0.17 ± 0.04	−0.53 ± 0.12	−0.19 ± 0.06	−0.44 ± 0.13	−0.18 ± 0.08
LBF	0.56 ± 0.09	−0.17 ± 0.06	0.56 ± 0.09	−0.17 ± 0.05	−0.53 ± 0.13	−0.18 ± 0.08	−0.52 ± 0.11	−0.17 ± 0.07

4.4.2 Medial-Lateral Base of Support Displacements

The cross-correlation results revealed that *left* and *right* were correlated with *RA*, *ExO*, *TES*, and *BF*. However, they were not correlated with *LD*, *LES*, and *RF*. The activation and deactivation of *LRA*, *LExO*, *LTES*, and *LBF* preceded *left* and *right*, respectively. Additionally, the activation and deactivation of *RRA*, *RExO*, *RTES*, and *RBF* preceded *right* and *left*, respectively. Figure 4.4 depicts mean CCFs across participants between the left body side muscles and *left* for the B1EC (dashed line) and B2EO (dotted line) conditions. Also shown are the mean CCFs across participants between the left body side muscles and *right* for the B1EC (dash-dot line) and B2EO (solid line) conditions. Mean CCFs for corresponding right body side muscles and *left* or *right* were found to be similar, but expectedly mirrored with respect to the time lag (τ) axis (*see Appendix D*). In Table 4.2, $r_{\text{max/min}}$ and corresponding $\tau_{\text{max/min}}$ values (mean ± standard deviation) across participants for all *left* and *right* correlations under the B1EC and B2EO conditions are presented. Note that shaded and non-shaded entries for $r_{\text{max/min}}$ again indicate muscle activation and deactivation, respectively.

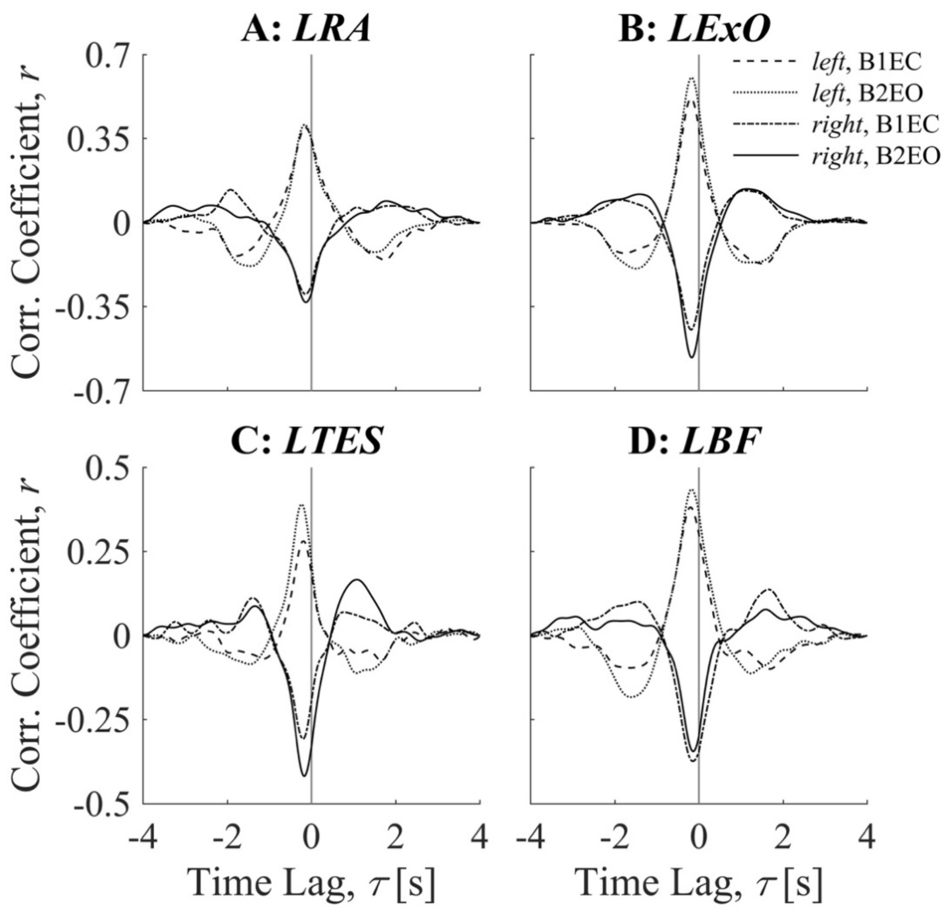

Figure 4.4: Mean cross-correlation functions across participants between left body side muscles and *left* for the Base 1 Eyes Closed (B1EC) (dashed line) and Base 2 Eyes Open (B2EO) (dotted line) conditions. Shown are also the mean cross-correlation functions across participants between left body side muscles and *right* for the B1EC (dash-dot line) and B2EO (solid line) conditions.

Correlated muscles are: left rectus abdominis (*LRA*) (A), left external oblique (*LExO*) (B), left thoracic erector spinae (*LTES*) (C), and left biceps femoris (*LBF*) (D).

Table 4.2: Maximum or minimum correlation coefficient ($r_{\text{max/min}}$) and corresponding time lag ($\tau_{\text{max/min}}$) values across participants. Shown are the values for *left* and *right* under the Base 1 Eyes Closed (B1EC) and Base 2 Eyes Open (B2EO) conditions when correlated with the activity of the following muscles: rectus abdominis (*RA*), external oblique (*ExO*), thoracic erector spinae (*TES*), and biceps femoris (*BF*). Left and right body side muscles are denoted with *L* and *R*, respectively, preceding the muscle abbreviation. Shaded and non-shaded entries for $r_{\text{max/min}}$ indicate muscle activation and deactivation, respectively. Since $\tau_{\text{max/min}}$ was negative for all correlations, muscle activation and deactivation always preceded wobble board displacement. All values are presented as mean ± standard deviation (presented variability is *inter-participant*).

	Left				***Right***			
	B1EC		**B2EO**		**B1EC**		**B2EO**	
Muscle	$r_{\text{max/min}}$	$\tau_{\text{max/min}}$ [s]	$r_{\text{max/min}}$	$\tau_{\text{max/min}}$ [s]	$r_{\text{max/min}}$	$\tau_{\text{max/min}}$ [s]	$r_{\text{max/min}}$	$\tau_{\text{max/min}}$ [s]
RRA	−0.34 ± 0.10	−0.11 ± 0.11	−0.35 ± 0.09	−0.11 ± 0.09	0.34 ± 0.05	−0.16 ± 0.10	0.43 ± 0.14	−0.15 ± 0.06
LRA	0.43 ± 0.12	−0.13 ± 0.06	0.43 ± 0.14	−0.16 ± 0.07	−0.32 ± 0.06	−0.13 ± 0.10	−0.36 ± 0.06	−0.13 ± 0.11
RExO	−0.48 ± 0.11	−0.16 ± 0.05	−0.53 ± 0.11	−0.17 ± 0.06	0.51 ± 0.14	−0.14 ± 0.05	0.63 ± 0.11	−0.16 ± 0.03
LExO	0.50 ± 0.14	−0.18 ± 0.06	0.62 ± 0.12	−0.17 ± 0.04	−0.44 ± 0.12	−0.17 ± 0.05	−0.59 ± 0.12	−0.15 ± 0.06
RTES	−0.30 ± 0.08	−0.15 ± 0.09	−0.43 ± 0.16	−0.19 ± 0.06	0.35 ± 0.13	−0.20 ± 0.07	0.44 ± 0.06	−0.19 ± 0.05
LTES	0.30 ± 0.07	−0.15 ± 0.10	0.42 ± 0.15	−0.22 ± 0.05	−0.33 ± 0.04	−0.18 ± 0.08	−0.41 ± 0.09	−0.14 ± 0.07
RBF	−0.32 ± 0.06	−0.14 ± 0.07	−0.42 ± 0.13	−0.15 ± 0.10	0.36 ± 0.14	−0.15 ± 0.08	0.44 ± 0.13	−0.11 ± 0.07
LBF	0.38 ± 0.09	−0.19 ± 0.09	0.45 ± 0.10	−0.18 ± 0.06	−0.39 ± 0.11	−0.15 ± 0.08	−0.38 ± 0.06	−0.12 ± 0.09

4.5 Discussion

The purpose of this study was to obtain a more comprehensive, quantitative understanding of the muscle activation patterns in unstable sitting, with the goal of using gained insights in closed-loop

FES applications. In what follows, we discuss the muscle activation patterns' spatial and temporal characteristics in the context of potentially underlying control mechanisms.

4.5.1 Presence of Active Control in Unstable Sitting

Our results show that wobble board displacement is correlated with direction-specific activation of trunk and upper leg muscles. Previous studies have shown that, for quiet sitting and small perturbations, tonic muscle activation may be sufficient to stabilize the trunk [24,31]; however, larger, transient perturbations require direction-specific, neurally-driven, phasic muscle activation to maintain trunk stability [31,32]. Our findings in unstable sitting agree with those in perturbed sitting as they show that phasic muscle activation is required to stabilize the trunk. Since the trunk is relatively upright and stationary during unstable sitting (*see Chapter 3*), it may be argued that wobble board displacement could activate the trunk and upper leg muscles via stretch reflex responses. However, for this to be true, wobble board displacement would necessarily need to precede stretch-induced muscle activation [246]. Since muscle activation preceded wobble board displacement for all direction-muscle pairs and conditions (*Tables 4.1 and 4.2*), it is not attributable to stretch reflex responses. Instead, the observed phasic activation is indicative of neurally-driven *active control* that originates in the central nervous system. It should be emphasized that *passive control* due to intrinsic mechanical properties of the spine, muscles, and connective tissue most certainly contributes to stabilization as well; nevertheless, our results suggest that active control plays a key role in maintaining stability during unstable sitting.

4.5.2 Preceding Muscle Activation and Compensation of Torque Generation Time Delay

In addition to suggesting that active control is present during unstable sitting, our finding that the trunk and upper leg muscles are activated *prior to* wobble board displacement agrees with similar results in upright standing where ankle extensor activity precedes body sway. More specifically, such work has shown that the central nervous system uses the position and velocity information of the body to activate the stabilizing muscles in a preceding manner, in spite of significant sensorimotor time delays [245,247]. Accordingly, our results may suggest that, during unstable sitting, the central nervous system uses the position and velocity information of the body – or its interaction with the base of support (*see Chapter 3*) – to activate the muscles prior to wobble board displacement. Similar to previous work in standing [248], the preceding activation of the muscles may be used to compensate for the torque generation time delay, i.e., the time it takes to generate a stabilizing moment after respective motor command has reached the muscle. In fact, the preceding time of muscle activation in our study (approximately 110 to 230 ms) is of similar duration as previously reported torque-generation time delays for joints whose moments can be experimentally measured (e.g., Masani et al., 2008). The presence of preceding muscle activation, as in our study, ensures a timely application of the moment at the wobble board-human interface to counter wobble board displacement.

4.5.3 Direction-Specific Muscle Activation and Stiffness Control

Our findings strongly suggest the existence of neurally-driven, direction-specific activation of trunk and upper leg muscles during unstable sitting. Previous studies have shown that, for both perturbed sitting [31,112,146,149] and standing [146], the trunk muscle response depends on the perturbation direction. Our findings in unstable sitting agree with those in perturbed sitting and standing as they show that neurally-driven, direction-specific activation is required to stabilize the trunk. Moreover, the contribution of each activated muscle to the stabilizing moment suggests that the CNS employs stiffness control in the *AP* but not the *ML* directions (*see below*).

For *anterior*, the activation of *RA* produces a *posterior* (stabilizing) moment at the wobble board-human interface, since the trunk can be assumed to be comparably upright during unstable sitting (*see Chapter 3*); and the activation of *BF* produces an *anterior* (destabilizing) moment. We speculate that the moment produced by *RA* is larger than the one produced by *BF*, resulting in a net *posterior* (stabilizing) moment. Furthermore, the concurrent activation of *RA* and *BF* results in higher stiffness at the wobble board-human interface than if only *RA* was activated. This suggests that the CNS employs stiffness control in the *anterior* direction, which could be to attain the accuracy in regulating the motion of the wobble board necessary to achieve stability [249].

For *posterior*, the activation of *ExO* or *RF* produces a *posterior* (destabilizing) moment; and the activation of *ES* produces an *anterior* (stabilizing) moment. We speculate that the moment produced by *ES* is larger than the one produced by *ExO* and *RF*, resulting in a net *anterior* (stabilizing) moment. Furthermore, the activation of *ExO*, *ES*, and *RF* results in higher stiffness at the wobble board-human interface than if only *ES* was activated. This suggests, again, that the CNS employs stiffness control in the *posterior* direction.

For *left*, the activation of *LRA*, *LExO*, *LTES*, or *LBF* produces a *right* moment, and the net moment is therefore a *right* (stabilizing) moment. Similarly, for *right*, the net moment is a *left* (stabilizing) moment. Unlike for the *AP* directions, our results do not suggest stiffness control in the *ML* directions. Reasons for this may include: (1) the activation of other muscles that could produce destabilizing moments in the *ML* directions did not result in sufficiently strong correlations with wobble board displacement; (2) the muscle(s) that could exhibit such behavior were not studied; and/or (3) the CNS does not employ stiffness control in the *ML* directions, which could be explained by intrinsic trunk stiffness being largest and smallest in the *ML* and *AP* directions, respectively [24]. In other words, intrinsic *ML* stiffness at the wobble board-human interface may be large enough for not requiring CNS stiffness control, resulting in motion-resisting activation of the *RA*, *ExO*, *TES*, and *BF muscles only*.

4.5.4 Conclusions and Future Directions

This study quantified the spatial and temporal relation of the angular kinematics of the wobble board and the trunk and upper leg muscle activity in unstable sitting. The wobble board-human system was stabilized through direction-specific activation of the muscles that preceded wobble board displacement. Direction-specific activation suggests the presence of active control, and preceding activation could be present to compensate for sensorimotor delays. Furthermore, our results suggest that the CNS employed stiffness control in the *AP* but not the *ML* directions. When developing a closed-loop FES system for unstable sitting, additional work is needed to quantify the muscle activation patterns directly from the observed kinematics. One approach could be to identify whether a model with feedback gains on wobble board displacement, velocity, and acceleration can predict EMG from wobble board kinematics, particularly for the positively correlated direction-muscle pairs identified in the present study. Note that a similar approach has recently been found to be successful for perturbed sitting [112]. Previous studies have additionally shown that the CNS employs synergistic muscle control during perturbed sitting [250]. Future work could therefore explore if such synergistic control is present during unstable sitting, as it could allow for simplified intermittent FES by reducing the number of required FES channels.

4.6 Acknowledgments

We would like to thank the Glenrose Rehabilitation Hospital for its in-kind support for this study. We would also like to thank Dhruv Prakash, Chris Wayne, and Andrew Williams for their contributions to experimental design, data acquisition, and data analysis. This study was partially funded through a Discovery Grant from the Natural Sciences and Engineering Research Council of Canada (RGPIN-2014-04666).

Chapter 5

5 Removing Force Plate Inertial Components from Any Instrumented Platform

The material presented in this chapter has been published in the article:

Roberts BWR, Hall JC, Williams AD, Rouhani H, Vette AH. A method to estimate inertial properties and force plate inertial components for instrumented platforms. Medical Engineering & Physics 2019;66:96–101.

The content of this chapter is identical to the material presented in the publication except for the text formatting which was done according to University of Alberta requirements. Parts of this work have also been presented at scientific conferences including *The XXVII Congress of the International Society of Biomechanics*, in conjunction with *The 43rd Annual Meeting of the American Society of Biomechanics*, held on July 31 to August 4, 2019, in Calgary, Canada.

5.1 Abstract

Kinetic data acquired from force plates embedded in moving platforms naturally contain artifacts due to platform acceleration, called force plate inertial components. While they can be estimated and removed from the measured signals, the system's inertial properties need to be known. Our objective was to: (1) develop a method for estimating the inertial properties and force plate inertial components for any instrumented platform; (2) estimate the inertial properties specifically for the Computer-Assisted Rehabilitation Environment (CAREN); and (3) validate the estimates with new experimental data. Unloaded ramp-and-hold perturbations (for estimation) and unloaded random perturbations (for validation) were executed to obtain the force, moment, and motion of the CAREN platform. Inertial properties were estimated by minimizing the error between the measured and computed inertial forces and moments. Obtained estimates were validated by

calculating the coefficient of determination (R^2) between the measured and computed forces or moments when keeping the inertial properties fixed. The estimates of the CAREN's inertial properties exhibited low variability across trials, and R^2 for the validation trials was 0.90±0.08 (mean±standard deviation). The developed method can be used for removing inertial components from force plate signals, yielding reliable estimates of ground reactions in dynamic biomechanical research and clinical assessments.

5.2 Introduction

The primary objective of human postural control is to maintain the body in a stable, upright position. While this task appears to be simple, it is accomplished by a complex process that takes advantage of previous experience (*feed-forward control*) [251,252] and seamless integration of sensory information (*feedback control*) [252–254]. Although the principles of postural control are generally understood, current efforts aim to shed light on the specific neurophysiological mechanisms the central nervous system applies to accomplish this task. Such mechanistic understanding is critical for clinicians seeking to identify balance deficits and optimize treatment in patient populations.

Postural perturbations displacing the body's center of mass (CoM) are commonly used to study the control of posture [253,255]. One of the most common forms of perturbations used in fundamental investigations is to disturb the support surface on which an individual is standing. Movement of the support surface, either through translation or rotation, displaces the base of support relative to the CoM, thus necessitating a neuromuscular reaction to reposition the CoM over the displaced base of support [253]. This is accomplished by means of timely, stabilizing moments that are globally reflected in the body's center of pressure fluctuation. Using an *instrumented platform* – defined as a moving platform embedding a single or multiple force plates – the trajectory of the center of pressure may be recorded and used to characterize postural stability and control, referred to as dynamic posturography. Depending on the application, different perturbation profiles are available, including ramp-and-hold, impulse, sinusoidal, or randomized profiles [256].

The need for an instrumented platform implies that studies involving dynamic posturography require complex and costly equipment. While multiple options are available [257–263], many of these systems are restricted to translations along, or rotations about, a finite set of principle axes [257]. However, one system in particular, the extended Computer-Assisted Rehabilitation Environment (CAREN; Motek Medical, Amsterdam, The Netherlands), employs a hydraulically actuated instrumented platform capable of delivering 6-degree of freedom perturbations. In addition, it includes: a 180-degree projection screen; a surround-sound audio system; a 12-camera motion capture system; and a dual-belt treadmill mounted above two force plates. With all of these features available, the CAREN seems optimal for all types of fundamental and rehabilitation research, including dynamic posturography. Unfortunately, such use is not always realistic as having the force plates embedded within the platform renders the data unreliable: in moving the force plates, the acquired forces and moments will contain components due to accelerating the total mass resting on the force plates' transducers, termed *force plate inertial components* (FPIC) [20]. Therefore, the CAREN's platform-embedded force plates can only be used to reliably measure kinetic data when the platform is stationary – as there is currently no accepted method to remove FPIC from CAREN force plate data [264,265]. This is, however, a problem not only for the force plates of the CAREN, but of any moving platform.

To solve the FPIC issue, Preuss et al. [20] introduced a method to isolate and reduce the effect of these components using motion capture and inverse dynamics. In tracking the moving base, they used the obtained position data along with the inertial properties of the platform (mass, moment of inertia, and position of platform's CoM relative to the force plate's transducers) to estimate the FPIC. A comparison between the predicted and acquired force plate signals validated the use of motion capture and inverse dynamics to reliably reduce FPIC from force plate data collected under dynamic conditions. Other potential methods to remove FPIC use accelerometers instead of motion capture [266,267]. Given that the CAREN is already equipped with a motion capture system, the approach outlined by Preuss et al. [20] offers the most suitable option to estimate and remove FPIC. The fundamental drawback of this method is, however, that it requires knowledge of the inertial properties of the platform. In addition, the assumption of symmetry suggests that the CoM lies directly above the average force plate transducer location, which further limits the method's application.

Oftentimes, for systems such as the CAREN, the inertial properties may be unknown, or vary between models. In addition, it is possible that the FPIC are affected by secondary components integrated into a given system (e.g., the treadmill in the CAREN). With that in mind, it is essential that a method be derived allowing users of the CAREN, or similar instrumented platforms, to estimate the inertial properties specific to their system, with the ultimate goal of removing the FPIC from the force plate measurements. The purpose of this study was therefore to: (1) outline a simple method for estimating the inertial properties and force plate inertial components for any instrumented platform; (2) estimate those properties specifically for the CAREN extended system; and (3) validate the obtained estimates via new experimental data.

5.3 Methods

5.3.1 Force Plate Signals

Force plate signals obtained during studies of dynamic posturography are a combination of ground reactions (applied to the force plate by the perturbed human) and inertial components (created by both motion and gravity of the platform). Therefore, the measured force plate force, $\vec{F}$, and moment, $\vec{M}$, expressed in the platform coordinate system (PCS) provided in Figure 5.1, are:

$$\begin{aligned} \vec{F} &= \vec{F}_{\mathrm{GR}} + \vec{F}_{\mathrm{I}} \\ \vec{M} &= \vec{M}_{\mathrm{GR}} + \vec{M}_{\mathrm{I}} \end{aligned} \tag{5.1}$$

where $\vec{F}_{\mathrm{GR}}$ and $\vec{M}_{\mathrm{GR}}$ are the ground reaction force and moment, respectively; and $\vec{F}_{\mathrm{I}}$ and $\vec{M}_{\mathrm{I}}$ are the inertial force and moment, respectively. Note that the force plate signals are assumed to be zeroed when the platform is in its starting orientation. The components of the inertial force are:

$$\begin{bmatrix} F_{\mathrm{I}_x} \\ F_{\mathrm{I}_y} \\ F_{\mathrm{I}_z} \end{bmatrix} = m \begin{bmatrix} a_x \\ a_y \\ a_z \end{bmatrix} + R_{xyz}^{\mathrm{T}} \begin{bmatrix} 0 \\ mg \\ 0 \end{bmatrix} - \begin{bmatrix} 0 \\ mg \\ 0 \end{bmatrix} \tag{5.2}$$

where m is the mass resting on the force plate transducers; a_x, a_y, and a_z are the components of the linear acceleration of the platform's CoM, $\vec{a}$, expressed in PCS; R_{xyz} is the rotation matrix capturing the orientation of PCS relative to the global coordinate system (GCS) provided in Figure 5.1; and g is the acceleration due to gravity. The components of the inertial moment are:

$$M_{I_x} = I_x\alpha_x + d_yF_{I_z} - d_zF_{I_y}$$
$$M_{I_y} = I_y\alpha_y - d_xF_{I_z} + d_zF_{I_x} \tag{5.3}$$
$$M_{I_z} = I_z\alpha_z + d_xF_{I_y} - d_yF_{I_x}$$

where I_x, I_y, and I_z are the principal components of the moment of inertia, $\vec{I}$, of the mass resting on the force plate transducers; α_x, α_y, and α_z are the components of the angular acceleration, $\vec{\alpha}$, of the platform; and d_x, d_y, and d_z are the components of the position, $\vec{d}$, of the CoM relative to the average force plate transducer location. Note that $\vec{I}$, $\vec{\alpha}$, and $\vec{d}$ are expressed in PCS. Detailed derivations of the components of $\vec{F}_I$ and $\vec{M}_I$ and of the PCS are provided in *Appendix E1* and *E2*, respectively.

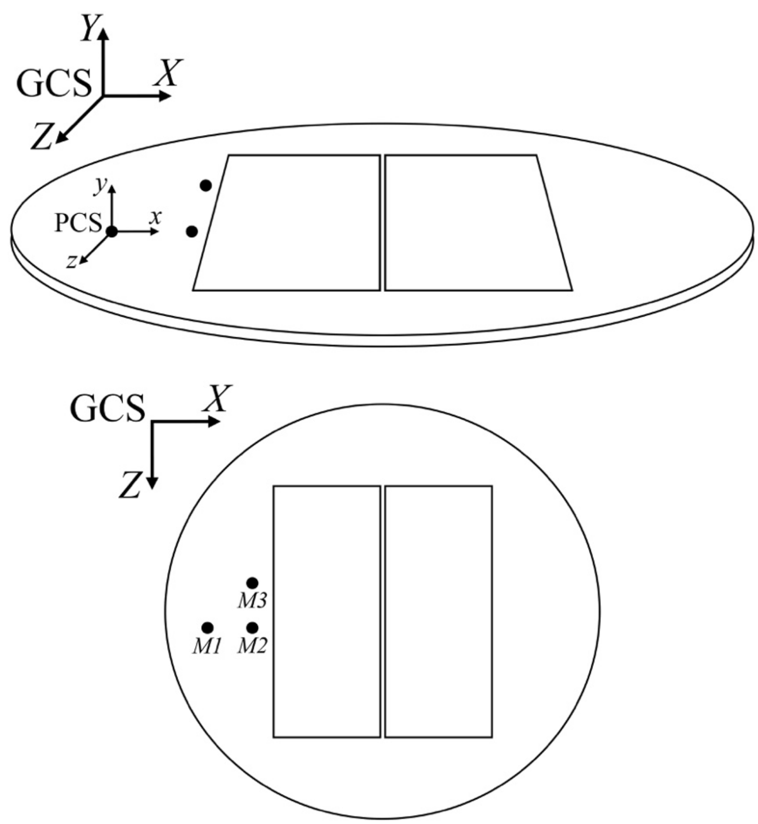

Figure 5.1: The orientations of the CAREN platform in its starting orientation relative to the global coordinate system (GCS); and of the platform coordinate system (PCS) relative to the CAREN platform. Three markers (*M1*, *M2*, and *M3*) were placed on the platform to define PCS, with *M1* and *M2* forming a line parallel to the *x* axis.

5.3.2 Experimental Procedure and Data Acquisition

To estimate the inertial properties m, $\vec{I}$, and $\vec{d}$ of the CAREN (*see Section 5.3.3.2*), two unloaded estimation trials (i.e., without a human user) were executed. Both estimation trials had ramp-and-hold perturbation profiles. The first estimation trial consisted of translations in the positive direction of each of the x, y, and z axes (Figure 5.1) followed by a return to the starting position. Translations from the starting position to maximum displacement, and vice versa, were 12 cm in 0.5 seconds, with a 3 second hold of maximum displacement [268–271]. Five translations were performed for each axis, for a total of fifteen translations. The second estimation trial consisted of positive rotations about each of the x, y, and z axes (Figure 5.1) followed by a return to the starting orientation. Rotations from the starting orientation to maximum angular displacement, and vice versa, were 7.5 degrees in 0.5 seconds, with a 3 second hold of maximum angular displacement [272–274]. Five rotations were performed for each axis, for a total of fifteen rotations.

To validate the estimated inertial properties (*see Section 5.3.3.3*), two unloaded validation trials were executed. Both validation trials had random perturbation profiles. The first validation trial consisted of random translations [265,275–277] along each of the x, y, and z axes (Figure 5.1). Five 10 second translations were performed for each axis, for a total of fifteen translations. The second validation trial consisted of random rotations [265,275–277] about each of the x, y, and z axes (Figure 5.1). Five 10 second rotations were performed for each axis, for a total of fifteen rotations. Different perturbation profiles were used across the three translation (rotation) axes, but the same perturbation profile was used for all five translations (rotations) of a given axis.

Force and moment data were recorded at a sampling frequency of 1,000 Hz [264,265] using two force plates (Bertec Corporation, Columbus, USA) embedded within the treadmill of the CAREN. Raw force plate data were down-sampled to 100 Hz and filtered using a fourth-order, zero phase-shift, low-pass Butterworth filter with a cut-off frequency of 5 Hz [264,265]. Platform motion data were recorded at 100 Hz [264,265] using a 12-camera motion capture system (MX T20S, Vicon Inc., Oxford, UK). Three markers (*M1*, *M2*, and *M3*) were placed on the platform, with *M1* and *M2* defining a line parallel to the x axis (Figure 5.1). Raw marker data were filtered using a second-order, zero phase-shift, low-pass Butterworth filter with a cut-off frequency of 4 Hz [264,265]. Note that raw force plate and marker data were expressed in PCS and GCS, respectively.

5.3.3 Experimental Data Analysis

5.3.3.1 Platform Kinematics

The position of the platform was calculated as the average of *M1*, *M2*, and *M3*. The linear acceleration of the platform, expressed in GCS, was then calculated from the position of the platform using finite difference equations [199]. Finally, the linear acceleration of the platform, $\vec{a}$, expressed in PCS, was calculated using its representation in GCS and R_{xyz}. The platform angles θ_x, θ_y, and θ_z were calculated from R_{xyz} using the Cardan *xyz* sequence [198]. The angular acceleration of the platform was then calculated from the angular displacement of the platform using finite difference equations [199]. Equations for $\vec{a}$, R_{xyz}, and the Cardan *xyz* sequence are provided in *Appendix E3*.

5.3.3.2 Estimation of Inertial Properties

Referring to Eq. (5.1), since the platform was unloaded (i.e., $\vec{F}_{\mathrm{GR}} = \vec{M}_{\mathrm{GR}} = 0$) for both the estimation and validation trials, $\vec{F} = \vec{F}_{\mathrm{I}}$ and $\vec{M} = \vec{M}_{\mathrm{I}}$. The inertial properties were therefore estimated by finding the values that minimized the sum of squared errors (SSE) between the force and moment recorded in the estimation trials and the computed, *reduced* inertial force and moment, respectively. Specifically, m and $\vec{d}$ were estimated from the translation, and $\vec{I}$ from the rotation trial data. The *reduced* inertial force and moment equations were derived from Eqs. (2) and (3) by setting variables to zero that were theoretically zero (e.g., $a_y = 0$ for x translations) and replacing $\vec{F}_{\mathrm{I}}$ components with corresponding $\vec{F}$ components in $\vec{M}_{\mathrm{I}}$. Detailed derivations of the *reduced* inertial force and moment in unloaded platform translations and rotations are provided in *Appendix E4* and *E5*, respectively.

For x translations, the SSE expressions that were minimized are:

$$\begin{aligned} \mathrm{SSE}_{F_x}(m) &= \sum_{i=1}^{N} [F_x(i) - \boldsymbol{m} a_x(i)]^2 \\ \mathrm{SSE}_{M_y}(d_z) &= \sum_{i=1}^{N} \left[M_y(i) - \boldsymbol{d_z} F_x(i)\right]^2 \end{aligned} \tag{5.4}$$

$$\mathrm{SSE}_{M_z}(d_y) = \sum_{i=1}^{N}\left[M_z(i) + \boldsymbol{d_y}F_x(i)\right]^2$$

where N is the total number of samples per translation (excluding hold time). Estimates of m, d_y, and d_z (bold in Eq. (5.4)) were obtained for each x translation, for a total of five estimates of each. The SSE expressions for y and z translations are similar. Note that m, d_x, and d_z estimates were obtained from y translations, and m, d_x, and d_y estimates were obtained from z translations. Overall m and $\vec{d}$ values (mean ± standard deviation) were calculated from the estimates from all translations.

For x rotations, the SSE expression that was minimized is:

$$\mathrm{SSE}_{M_x}(I_x) = \sum_{i=1}^{N}\left[M_x(i) - \left(\boldsymbol{I_x}\alpha_x(i) + d_yF_z(i) - d_zF_y(i)\right)\right]^2 \tag{5.5}$$

where N is as before, but for rotations, and d_y and d_z are mean estimates identified earlier. An estimate of I_x (bold in Eq. (5.5)) was obtained for each x rotation, for a total of five estimates. The SSE expressions for y and z rotations are similar. Note that I_y and I_z estimates were obtained from y and z rotations, respectively. Overall $\vec{I}$ values (mean ± standard deviation) were calculated from the estimates from all rotations.

SSE expressions were minimized using the function *fminsearch* in MATLAB (version R2017a, MathWorks, Natick, United States). A complete set of SSE expressions is provided in *Appendix E6*.

5.3.3.3 Validation of Estimated Inertial Properties

The mean estimates of the inertial properties and the equations for the inertial components were validated by calculating, for all estimation and validation data, the coefficient of determination (R^2) between the measured and computed force or moment. Overall R^2 values (mean ± standard deviation) were reported for estimation and validation trials separately.

5.4 Results

5.4.1 Inertial Properties of the CAREN Extended System

Figure 5.2 depicts representative time series of the linear displacement (A) and acceleration (C) of the unloaded CAREN platform, along with the measured force F_x (B) and moment M_z (D), for a ramp-and-hold x translation in an estimation trial. The 0.5 second intervals of the translation used to estimate m and d_y are marked with bold lines. It can be clearly seen that the measured force F_x and moment M_z are affected by the motion of the platform.

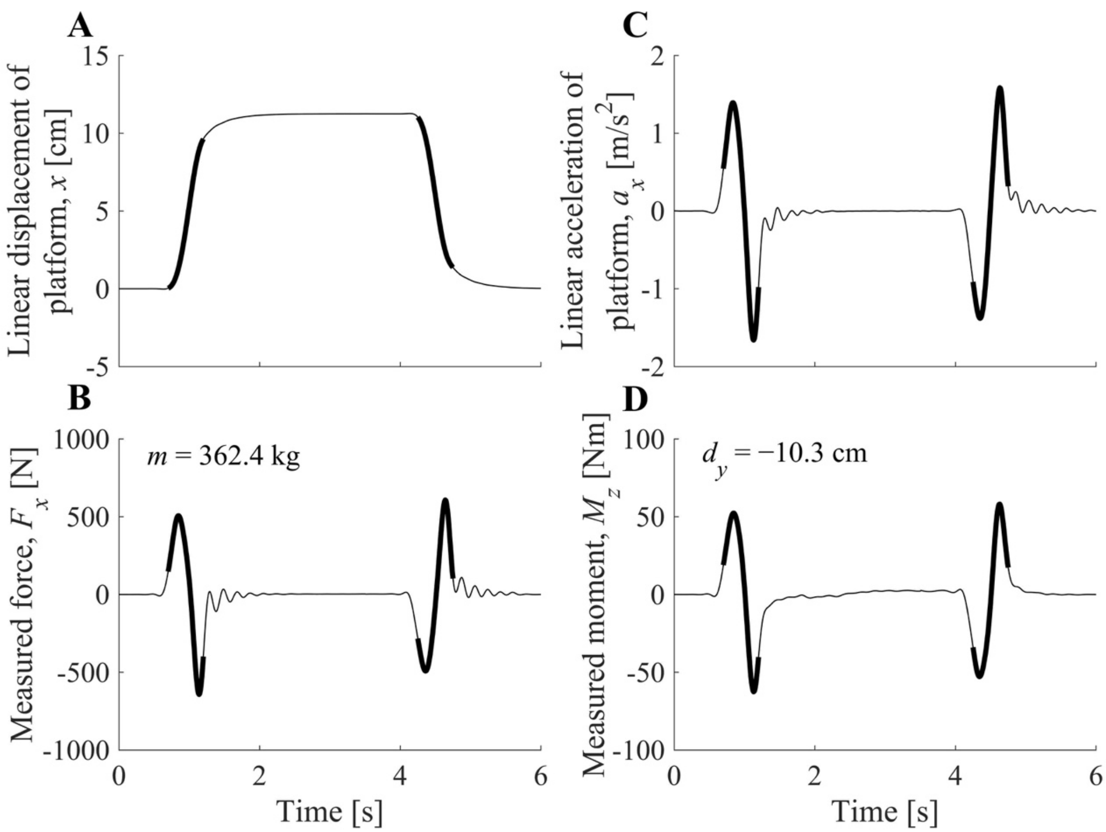

Figure 5.2: Representative platform motion and corresponding force plate time series for a ramp-and-hold x translation in an estimation trial. A and C: Linear displacement and acceleration of the platform; B and D: Corresponding measured force F_x and moment M_z. Bold lines mark the 0.5 second intervals of the translation used to estimate the mass resting on the force plate transducers, m, and the y component of the position of the center of mass relative to the average force plate transducer location, d_y. Estimates of m and d_y obtained from the translation are shown.

In Table 5.1, the estimated inertial properties of the CAREN are presented (mean ± standard deviation). Listed are the values calculated for each axis (from five estimates for translations and five estimates for rotations) and across all movements. The overall value for d_x (0.0 ± 0.3 cm) indicates that the CAREN platform is symmetrical with respect to its yz plane.

Table 5.1: Estimated inertial properties of the CAREN extended system. Listed are the values calculated for each axis (from five estimates for translations and five estimates for rotations) and across all movements. All values are presented as mean ± standard deviation.

Axis	Inertial Property						
	m [kg]	d_x [cm]	d_y [cm]	d_z [cm]	I_x [kg m^2]	I_y [kg m^2]	I_z [kg m^2]
x	362.3 ± 0.1	-	−10.5 ± 0.1	−8.3 ± 0.1	139.5 ± 2.5	-	-
y	356.3 ± 1.0	−0.2 ± 0.0	-	−13.3 ± 0.2	-	165.1 ± 1.2	-
z	351.0 ± 0.6	0.3 ± 0.1	−6.9 ± 0.3	-	-	-	46.3 ± 0.2
Overall	**356.5 ± 4.8**	**0.0 ± 0.3**	**−8.7 ± 2.0**	**−10.8 ± 2.6**	**139.5 ± 2.5**	**165.1 ± 1.2**	**46.3 ± 0.2**

5.4.2 Validation of Computed Inertial Force and Moment

Figure 5.3A and B depict representative time series of the linear displacement of the CAREN platform and the measured force F_x (black line), respectively, for a random x translation in a validation trial. Figure 5.3C and D depict representative time series of the platform angle θ_x and the measured moment M_x (black line), respectively, for a random x rotation in a validation trial. In Figure 5.3B and D, the measured force F_x and moment M_x are compared to the computed force F_{I_x} and moment M_{I_x} (gray lines), respectively. A visual inspection and respective R^2 values for the translation ($R^2 = 0.94$) and rotation ($R^2 = 0.96$) suggest the ability of Eq. (5.2) and (5.3) to estimate the inertial force and moment in CAREN force plate signals.

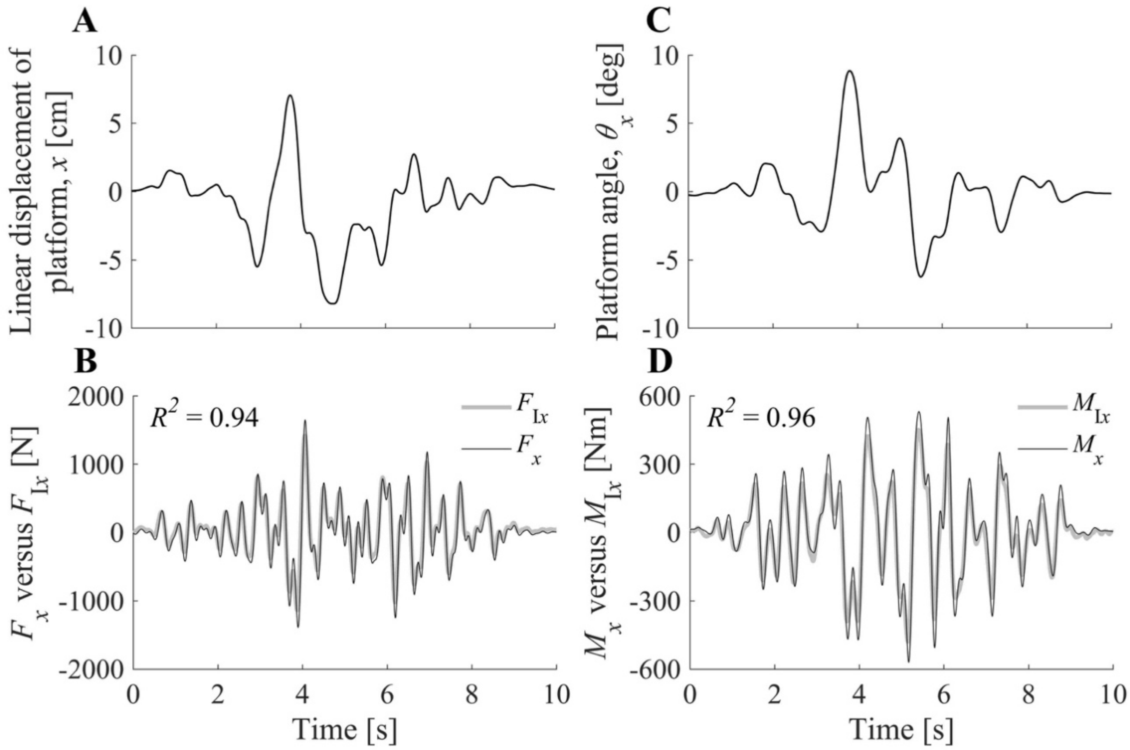

Figure 5.3: Representative platform motion and corresponding force plate time series for a random x translation (A and B) and rotation (C and D) in the validation trials. A and B: Linear displacement of the platform, x, and comparison between the x component of the corresponding measured force (black) and the computed inertial force (gray). The coefficient of determination, R^2, between the forces was $R^2 = 0.94$. C and D: Platform angle about the x axis, θ_x, and comparison between the x component of the corresponding measured moment (black) and the computed inertial moment (gray). The coefficient of determination between the moments was $R^2 = 0.96$.

In Table 5.2, overall R^2 values (mean ± standard deviation) for estimation and validation trials are presented. Also presented are values calculated from the five R^2 values from each translation or rotation, for each component of the measured force and moment. The overall R^2 value for the validation trials (0.90 ± 0.08) confirms that the mean estimates of the inertial properties, together with Eq. (5.2) and (5.3), can predict the inertial force and moment in CAREN force plate signals.

Table 5.2: Coefficient of determination (R^2) values between the measured force and moment and the computed inertial force and moment, respectively. Shown are overall R^2 values for estimation (ramp-and-hold) and validation (random) trials. Also shown are values calculated from the five R^2 values from each translation or rotation, for each component of the measured force and moment. All values are presented as mean ± standard deviation.

		Axis	Coefficient of Determination (R^2)					
			F_x	F_y	F_z	M_x	M_y	M_z
Ramp-and-Hold	***Trans.***	***x***	0.98 ± 0.00	-	-	-	0.94 ± 0.02	0.94 ± 0.01
		y	-	0.98 ± 0.00	-	0.90 ± 0.01	-	-
		z	-	-	0.98 ± 0.00	0.89 ± 0.03	-	-
	Rot.	***x***	-	-	-	0.98 ± 0.00	-	-
		y	-	-	-	-	0.99 ± 0.00	-
		z	-	-	-	-	-	0.99 ± 0.00
Random	***Trans.***	***x***	0.94 ± 0.00	-	-	-	0.87 ± 0.01	0.88 ± 0.01
		y	-	0.96 ± 0.00	-	0.85 ± 0.01	-	-
		z	-	-	0.94 ± 0.00	0.70 ± 0.03	-	-
	Rot.	***x***	-	-	-	0.96 ± 0.00	-	-
		y	-	-	-	-	0.96 ± 0.00	-
		z	-	-	-	-	-	0.96 ± 0.00
Overall ramp-and-hold: 0.96 ± 0.04; Overall random: 0.90 ± 0.08								

5.5 Discussion

The objectives of the present study were to develop a method for estimating the inertial properties and FPIC for any instrumented platform, and to estimate and validate the inertial properties specifically for the CAREN. Low variability of the estimated inertial properties for the CAREN (*see Table 5.1*) and excellent agreement between the measured and computed force or moment (*see Figure 5.3 and Table 5.2*) confirm the adequacy of the developed method to meet our objectives. It can be used for removing inertial components from force plate signals, yielding reliable estimates of ground reactions in biomechanical research and clinical assessments. In what follows, we recommend a simplified experimental procedure and assumptions for $\vec{d}$ for symmetrical platforms, discuss alternative SSE expressions, and elaborate on how overall R^2 values were calculated.

5.5.1 Simplified Procedure and Considerations for Symmetrical Platforms

Based on an inspection of the variability of the CAREN inertial property values presented in Table 5.1, a *simplified* experimental procedure is recommended. Specifically, in the estimation trial used to estimate m and $\vec{d}$ (translations), we recommend that only one translation be performed for each axis, for a total of three translations. Additionally, in the estimation trial used to estimate $\vec{I}$ (rotations), we recommend that only one rotation be performed for each axis, for a total of three rotations.

For platforms that are known to be symmetrical with respect to only one of their *xy* and *yz* planes (i.e., *partial* symmetry), we recommend d_z be assumed zero (for *xy* plane symmetry) or d_x be assumed zero (for *yz* plane symmetry) and not calculated from acquired force, moment, and platform motion data. Since the CAREN extended system is symmetrical with respect to its *yz* plane, we recommend that, for this system, d_x be assumed zero. For platforms that are known to be symmetrical with respect to both their *xy* and *yz* planes (i.e., *full* symmetry), we recommend both d_x and d_z be assumed zero. Note that the method to estimate and remove FPIC introduced by Preuss et al. [20] assumes *full* symmetry and should therefore not be applied if the platform does not possess *full* symmetry. However, if the platform is known to possess *full* symmetry, their method to estimate and remove FPIC is equivalent to the one developed here. Nevertheless, it assumes knowledge of the inertial properties of the platform.

5.5.2 Alternative to Reduced Method for Estimating Inertial Properties

The *reduced* inertial force and moment used in the SSE expressions (*see Section 5.3*) were chosen in this work because they provide a *simple* method for estimating the inertial properties of a platform. Alternative SSE expressions may be developed that find inertial property values that minimize the SSE between the measured force and moment and the inertial force and moment computed using Eq. (5.2) and (5.3), respectively. However, these SSE expressions would be coupled and therefore require a simultaneous approach in solving them. Moreover, we expect that this alternative, more involved approach would yield similar inertial property estimates to those obtained here, since: (1) the simplifying assumptions made in deriving the *reduced* inertial force and moment (*see Appendix E4 and E5*) are justified; and (2) the overall R^2 value for the validation trials (0.90 ± 0.08) indicates that the mean estimates of the inertial properties are acceptable.

5.5.3 Values used in Calculating Overall R^2 Values

Overall R^2 values for estimation and validation trials were calculated using only R^2 values from select components of the measured force and moment depending on the axis (i.e., x, y, or z) and perturbation type (i.e., translation or rotation) (*see Table 5.2*). For a particular axis and type of perturbation, R^2 values from force and moment components were excluded (and not reported in *Table 5.2*) if the force and moment components: (1) were theoretically zero (e.g., F_y and M_x for x translations); (2) negligibly small due to d_x being negligibly small (e.g., M_z for y translations); or (3) otherwise negligibly small (e.g., all components of $\vec{F}$, M_y, and M_z for x rotations).

5.6 Acknowledgments

We would like to thank Darrell Goertzen for his contributions to CAREN programming and experimental data acquisition. This study was partially funded through a Discovery Grant from the Natural Sciences and Engineering Research Council of Canada (RGPIN-2014-04666).

6 Conclusion

Recent work suggests that closed-loop electrical stimulation may restore dynamic trunk stability following neuromuscular impairment. However, developing such neuroprostheses requires quantitative predictions of the activation profiles of relevant muscles under different types of dynamic trunk disturbances experienced in daily life during non-impaired sitting. Muscle activity predictions could be based on characteristic angular kinematics or the body's center of pressure displacement in dynamic sitting. Challenges exist, however, that need to be resolved to allow kinematics- or kinetics-based predictions of muscle activity to be obtained in dynamic sitting.

The first objective of this thesis was to quantify the kinematics characterizing trunk stabilization in unstable sitting. During unstable sitting, the trunk is stabilized through relatively large, fast displacements of the base of support, whereas the trunk adopts a quasi-static pose (Chapter 3). These insights can be used to quantify the relation between the characteristic kinematics and the muscle activity in unstable sitting.

The second objective of this thesis was to quantify both the spatial and temporal relations between the characteristic kinematics and the muscle activity in unstable sitting. During unstable sitting, the trunk is stabilized through direction-specific activation of the trunk and upper leg muscles that precedes base of support displacement temporally (Chapter 4). This relation can be used to predict the kinematics-based muscle activation patterns within a closed-loop electrical stimulation system for dynamic sitting.

The third objective of this thesis was to propose and validate a method for estimating the inertial properties and force plate inertial components for any instrumented platform. Low variability of the estimated inertial properties for the Computer-Assisted Rehabilitation Environment and excellent agreement between the measured and computed forces and moments confirm the adequacy of the developed method to meet this objective (Chapter 5). The developed method can be used to quantify the relation between the body's center of pressure displacement and the muscle activity in dynamic sitting. The obtained relations can again be used to predict the center of pressure-based muscle activation patterns within a closed-loop electrical stimulation system for dynamic sitting.

6.1 Recommendations for Future Work

Closed-loop electrical stimulation systems for restoring dynamic trunk stability following impairment require quantitative kinematics- or kinetics-based predictions of muscle activity under different types of dynamic trunk disturbances experienced in daily life during non-impaired sitting. Among the types of disturbances that may be experienced – intrinsic instability or external displacement of the support surface, as well as the exposure to external trunk forces – kinematics- or kinetics-based predictions of muscle activity have been obtained only in response to external trunk forces (Chapter 2). Specifically, kinematics-based predictions have been obtained, in several directions for each trunk muscle, using a model with feedback gains on trunk displacement, velocity, and acceleration (Chapter 2) [112].

To design robust closed-loop electrical stimulation systems for restoring dynamic trunk stability, additional work is therefore needed to obtain kinematics- or kinetics-based predictions of muscle activity under all the different types of dynamic trunk disturbances that may be experienced. To obtain kinematics-based predictions of muscle activity in the dynamic sitting paradigms, one approach could be to identify whether models with feedback gains on characteristic displacement, velocity, and acceleration can predict muscle activity from characteristic kinematics (i.e., similar to the approach that has been found to be successful for the exposure to external trunk forces). This approach could be applied, in particular, for the muscles that are activated in a particular direction of base of support displacement in unstable sitting (Chapter 4) or direction of trunk displacement when displacing the support surface [146,149]. Similarly, this approach could be applied to kinetics-based predictions of muscle activity in the dynamic sitting paradigms (using the insights from Chapter 5), but instead using models with feedback gains on center of pressure displacement, velocity, and acceleration. However, before obtaining such predictions, the relation between the body's center of pressure displacement and the muscle activity in the dynamic sitting paradigms needs to be quantified.

References

[1] Dupeyron A, Perrey S, Micallef JP, Pélissier J. Influence of back muscle fatigue on lumbar reflex adaptation during sudden external force perturbations. J Electromyogr Kinesiol 2010;20:426–32.

[2] Shumway-Cook A, Woollacott MH. Motor control: theory and practical applications. 1st ed. Maryland: Lippincott Williams & Wilkins; 1995.

[3] Hyun GK, Dingwell JB. A direct comparison of local dynamic stability during unperturbed standing and walking. Exp Brain Res 2006;172:35–48.

[4] Lin VW, Bono CM. Spinal cord medicine: principles and practice. 2nd ed. New York: Demos Medical Publishing; 2010.

[5] Chen CL, Yeung KT, Bih LI, Wang CH, Chen MI, Chien JC. The relationship between sitting stability and functional performance in patients with paraplegia. Arch Phys Med Rehabil 2003;84:1276–81.

[6] Potten YJM, Seelen HAM, Drukker J, Reulen JPH, Drost MR. Postural muscle responses in the spinal cord injured persons during forward reaching. Ergonomics 1999;42:1200–15.

[7] Janssen-Potten YJ, Seelen HA, Drukker J, Reulen JP. Chair configuration and balance control in persons with spinal cord injury. Arch Phys Med Rehabil 2000;81:401–8.

[8] Reft J, Hasan Z. Trajectories of target reaching arm movements in individuals with spinal cord injury: effect of external trunk support. Spinal Cord 2002;40:186–91.

[9] Janssen-Potten YJ, Seelen HA, Drukker J, Spaans F, Drost MR. The effect of footrests on sitting balance in paraplegic subjects. Arch Phys Med Rehabil 2002;83:642–8.

[10] Aissaoui R, Boucher C, Bourbonnais D, Lacoste M, Dansereau J. Effect of seat cushion on dynamic stability in sitting during a reaching task in wheelchair users with paraplegia. Arch Phys Med Rehabil 2001;82:274–81.

[11] Ho CH, Triolo RJ, Elias AL, Kilgore KL, DiMarco AF, Bogie K, et al. Functional electrical stimulation and spinal cord injury. Phys Med Rehabil Clin N Am 2014;25:631–54.

[12] Vette AH, Wu N, Masani K, Popovic MR. Low-intensity functional electrical stimulation can increase multidirectional trunk stiffness in able-bodied individuals during sitting. Med Eng Phys 2015;37:777–82.

[13] Levy M, Mizrahi J, Susak Z. Recruitment, force and fatigue characteristics of quadriceps muscles of paraplegics isometrically activated by surface functional electrical stimulation. J Biomed Eng 1990;12:150–6.

[14] Lee H, Granata KP, Madigan ML. Effects of trunk exertion force and direction on postural control of the trunk during unstable sitting. Clin Biomech 2008;23:505–9.

[15] Larivière C, Gagnon DH, Mecheri H. Trunk postural control in unstable sitting: effect of sex and low back pain status. Clin Biomech 2015;30:933–9.

[16] Freddolini M, Strike S, Lee R. Dynamic stability of the trunk during unstable sitting in people with low back pain. Spine (Phila Pa 1976) 2014;39:785–90.

[17] Freddolini M, Strike S, Lee RYW. Stiffness properties of the trunk in people with low back pain. Hum Mov Sci 2014;36:70–9.

[18] Willigenburg NW, Kingma I, Van Dieën JH. Center of pressure trajectories, trunk kinematics and trunk muscle activation during unstable sitting in low back pain patients. Gait Posture 2013;38:625–30.

[19] Oomen NMCW, Reeves NP, Priess MC, van Dieën JH. Trunk muscle coactivation is tuned to changes in task dynamics to improve responsiveness in a seated balance task. J Electromyogr Kinesiol 2015;25:765–72.

[20] Preuss R, Fung J. A simple method to estimate force plate inertial components in a moving surface. J Biomech 2004;37:1177–80.

[21] Claudino R, dos Santos ECC, Santos MJ. Compensatory but not anticipatory adjustments are altered in older adults during lateral postural perturbations. Clin Neurophysiol 2013;124:1628–37.

[22] Kanekar N, Aruin AS. The effect of aging on anticipatory postural control. Exp Brain Res 2014;232:1127–36.

[23] Aruin AS, Kanekar N, Lee YJ, Ganesan M. Enhancement of anticipatory postural adjustments in older adults as a result of a single session of ball throwing exercise. Exp Brain Res 2014;233:649–55.

[24] Vette AH, Masani K, Wu N, Popovic MR. Multidirectional quantification of trunk stiffness and damping during unloaded natural sitting. Med Eng Phys 2014;36:102–9.

[25] Tisserand R, Robert T, Chabaud P, Livet P, Bonnefoy M, Chèze L. Comparison between investigations of induced stepping postural responses and voluntary steps to better detect community-dwelling elderly fallers. Neurophysiol Clin 2015;45:269–84.

[26] Shmidt RA, Lee TD. Motor control and learning: a behavioural emphasis. 5th ed. Illinois: Human Kinetics; 2011.

[27] Cresswell AG, Oddsson L, Thorstensson A. The influence of sudden perturbations on trunk muscle activity and intra-abdominal pressure while standing. Exp Brain Res 1994;98:336–41.

[28] Grillner S, Nilsson J, Thorstensson A. Intra-abdominal pressure changes during natural movements in man. Acta Physiol Scand 1978;103:275–83.

[29] Loram ID, Lakie M. Human balancing of an inverted pendulum: position control by small, ballistic-like, throw and catch movements. J Physiol 2002;540:1111–24.

[30] Patla AE, Ishac MG, Winter DA. Anticipatory control of center of mass and joint stability during voluntary arm movement from a standing posture: interplay between active and passive control. Exp Brain Res 2002;143:318–27.

[31] Masani K, Sin VW, Vette AH, Thrasher AT, Kawashima N, Morris A, et al. Postural reactions of the trunk muscles to multi-directional perturbations in sitting. Clin Biomech 2009;24:176–82.

[32] Moorhouse KM, Granata KP. Role of reflex dynamics in spinal stability: intrinsic muscle stiffness alone is insufficient for stability. J Biomech 2007;40:1058–65.

[33] McGill SM. Electromyographic activity of the abdominal and low back musculature during the generation of isometric and dynamic axial trunk torque: implications for lumbar mechanics. J Orthop Res 1991;9:91–103.

[34] Ng JKF, Kippers V, Parnianpour M, Richardson CA. EMG activity normalization for trunk muscles in subjects with and without back pain. Med Sci Sports Exerc 2002;34:1082–6.

[35] Sullivan PBO, Grahamslaw KM, Ther MM, Kendell M, Lapenskie SC, Moller NE, et al. The effect of different standing and sitting postures on trunk muscle activity in a pain-free population. Spine (Phila Pa 1976) 2002;27:1238–44.

[36] Lehman GJ, McGill SM. Spinal manipulation causes variable spine kinematic and trunk muscle electromyographic responses. Clin Biomech 2001;16:293–9.

[37] Vera-Garcia FJ, Brown SHM, Gray JR, McGill SM. Effects of different levels of torso coactivation on trunk muscular and kinematic responses to posteriorly applied sudden loads. Clin Biomech 2006;21:443–55.

[38] Cholewicki J, McGill SM. Mechanical stability of the in vivo lumbar spine: implications for injury and chronic low back pain. Clin Biomech 1996;11:1–15.

[39] Kendall FP, McCreary EK, Provance PG, Rodgers MM, Romani WA. Muscles: testing and function with posture and pain. 5th ed. Maryland: Lippincott Williams & Wilkins; 2005.

[40] Chauvie S, Obertino M, Papaleo A, Ruspa M, Solano A, Gozzoli L, et al. A method for the visual analysis of early-stage Parkinson's disease based on virtual MRI-derived SPECT images. Int J Imaging Syst Technol 2012;22:172–6.

[41] Pearsall DJ, Reid JG, Livingston LA. Segmental inertial parameters of the human trunk as determined from computed tomography. Ann Biomed Eng 1996;24:198–210.

[42] Farahpour N, Ghasemi S, Allard P, Saba MS. Electromyographic responses of erector spinae and lower limb's muscles to dynamic postural perturbations in patients with adolescent idiopathic scoliosis. J Electromyogr Kinesiol 2014;24:645–51.

[43] Kim M, Han S, Kim S. Changes in the range of motion of the hip joint and the muscle activity of the rectus femoris and biceps femoris of stroke patients during obstacles crossing on the ground and underwater. J Phys Ther Sci 2014;26:1143–6.

[44] Song CY, Huang HY, Chen SC, Lin JJ, Chang AH. Effects of femoral rotational taping on pain, lower extremity kinematics, and muscle activation in female patients with patellofemoral pain. J Sci Med Sport 2015;18:388–93.

[45] Kuhnen HR, Rybar MM, Onushko T, Doyel RE, Hunter SK, Schmit BD, et al. Stroke-related effects on maximal dynamic hip flexor fatigability and functional implications. Muscle Nerve 2015;51:446–8.

[46] Jiroumaru T, Kurihara T, Isaka T. Measurement of muscle length-related electromyography activity of the hip flexor muscles to determine individual muscle contributions to the hip flexion torque. Springerplus 2014;3:1–9.

[47] Jung HS, Kang SY, Park JH, Cynn HS, Jeon HS. EMG activity and force during prone hip extension in individuals with lumbar segmental instability. Man Ther 2015;20:440–4.

[48] Oh J-S. Effects of pelvic belt on hip extensor muscle EMG activity during prone hip

extension in females with chronic low back pain. J Phys Ther Sci 2014;26:1023–4.

[49] Winters JM, Woo SL-Y. Multiple muscle systems: biomechanics and movement organization. 1st ed. New York: Springer; 1990.

[50] Sherwood AM, Dimitrijevic MR, Barry McKay W. Evidence of subclinical brain influence in clinically complete spinal cord injury: discomplete SCI. J Neurol Sci 1992;110:90–8.

[51] Maynard FM, Bracken MB, Creasey G, Ditunno JF, Donovan WH, Ducker TB, et al. International standards for neurological and functional classification of spinal cord injury. Spinal Cord 1997;35:266–74.

[52] Gorgey AS, Dudley GA. Skeletal muscle atrophy and increased intramuscular fat after incomplete spinal cord injury. Spinal Cord 2007;45:304–9.

[53] Milosevic M, Masani K, Kuipers MJ, Rahouni H, Verrier MC, McConville KMV, et al. Trunk control impairment is responsible for postural instability during quiet sitting in individuals with cervical spinal cord injury. Clin Biomech 2015;30:507–12.

[54] Zacharkow D. Posture: sitting, standing, chair design and exercise. 1st ed. Illinois: Charles C Thomas; 1988.

[55] Bolin I, Bodin P, Kreuter M. Sitting position - posture and performance in C5 - C6 tetraplegia. Spinal Cord 2000;38:425–34.

[56] Samuelsson KAM, Tropp H, Gerdle B. Shoulder pain and its consequences in paraplegic spinal cord-injured, wheelchair users. Spinal Cord 2004;42:41–6.

[57] Lee H, Granata KP. Process stationarity and reliability of trunk postural stability. Clin Biomech 2008;23:735–42.

[58] Hendershot BD, Toosizadeh N, Muslim K, Madigan ML, Nussbaum MA. Evidence for an exposure-response relationship between trunk flexion and impairments in trunk postural control. J Biomech 2013;46:2554–7.

[59] Tanaka ML, Nussbaum MA, Ross SD. Evaluation of the threshold of stability for the human spine. J Biomech 2009;42:1017–22.

[60] Slota GP, Granata KP, Madigan ML. Effects of seated whole-body vibration on postural control of the trunk during unstable seated balance. Clin Biomech 2008;23:381–6.

[61] Shahvarpour A, Shirazi-Adl A, Larivière C. Active-passive biodynamics of the human trunk when seated on a wobble chair. J Biomech 2016;49:939–45.

[62] Larivière C, Mecheri H, Shahvarpour A, Gagnon D, Shirazi-Adl A. Criterion validity and between-day reliability of an inertial-sensor-based trunk postural stability test during unstable sitting. J Electromyogr Kinesiol 2013;23:899–907.

[63] Shahvarpour A, Gagnon D, Preuss R, Henry SM, Larivière C. Trunk postural balance and low back pain: reliability and relationship with clinical changes following a lumbar stabilization exercise program. Gait Posture 2018;61:375–81.

[64] Hendershot BD, Nussbaum MA. Persons with lower-limb amputation have impaired trunk postural control while maintaining seated balance. Gait Posture 2013;38:438–42.

[65] Acasio JC, Butowicz CM, Golyski PR, Nussbaum MA, Hendershot BD. Associations

between trunk postural control in walking and unstable sitting at various levels of task demand. J Biomech 2018;75:181–5.

[66] Cholewicki J, Peter Reeves N, Everding VQ, Morrisette DC. Lumbosacral orthoses reduce trunk muscle activity in a postural control task. J Biomech 2007;40:1731–6.

[67] Albertsen IM, Temprado JJ, Berton E, Heuer H. Effect of haptic supplementation on postural control of younger and older adults in an unstable sitting task. J Electromyogr Kinesiol 2014;24:572–8.

[68] Haruyama K, Kasai K, Makino R, Hoshi F, Nishihara K. Quantification of trunk segmental coordination and head stability in laterally unstable sitting identifies aging and cerebellar ataxia. Clin Biomech 2019;63:127–33.

[69] Motealleh A, Kordi Yoosefinejad A, Ghoddosi M, Azhdari N, Pirouzi S. Trunk postural control during unstable sitting differs between patients with patellofemoral pain syndrome and healthy people: a cross-sectional study. Knee 2019;26:26–32.

[70] Van Dieen J, Koppes L, Twisk J. Low back pain history and postural sway in unstable sitting. Spine (Phila Pa 1976) 2010;35:812–7.

[71] Reeves NP, Everding VQ, Cholewicki J, Morrisette DC. The effects of trunk stiffness on postural control during unstable seated balance. Exp Brain Res 2006;174:694–700.

[72] Van Daele U, Hagman F, Truijen S, Vorlat P, Van Gheluwe B, Vaes P. Differences in balance strategies between nonspecific chronic low back pain patients and healthy control subjects during unstable sitting. Spine (Phila Pa 1976) 2009;34:1233–8.

[73] Andreopoulou G, Maaswinkel E, Cofré Lizama LE, van Dieën JH. Effects of support surface stability on feedback control of trunk posture. Exp Brain Res 2015;233:1079–87.

[74] Barbado D, Moreside J, Vera-Garcia FJ. Reliability and repetition effect of the center of pressure and kinematics parameters that characterize trunk postural control during unstable sitting test. PM R 2017;9:219–30.

[75] Sung W, Abraham M, Plastaras C, Silfies SP. Trunk motor control deficits in acute and subacute low back pain are not associated with pain or fear of movement. Spine J 2015;15:1772–82.

[76] Radebold A, Cholewicki J, Polzhofer GK, Greene HS. Impaired postural control of the lumbar spine is associated with delayed muscle response times in patients with chronic idiopathic low back pain. Spine (Phila Pa 1976) 2001;26:724–30.

[77] Barbado D, Reina R, Roldan A, McCulloch K, Campayo-Piernas M, Vera-Garcia FJ. How much trunk control is affected in adults with moderate-to-severe cerebral palsy? J Biomech 2019;82:368–74.

[78] Peter Reeves N, Cholewicki J, Narendra KS. Effects of reflex delays on postural control during unstable seated balance. J Biomech 2009;42:164–70.

[79] Feipel V, Parent C, Dugailly PM, Brassinne E, Salvia P, Rooze M. Development of kinematics tests for the evaluation of lumbar proprioception and equilibration. Clin Biomech 2003;18:612–8.

[80] Duclos NC, Maynard L, Abbas D, Mesure S. Effects of aging in postural strategies during

a seated auto-stabilization task. J Electromyogr Kinesiol 2013;23:807–13.

[81] van Dieën JH, Koppes LLJ, Twisk JWR. Postural sway parameters in seated balancing; their reliability and relationship with balancing performance. Gait Posture 2010;31:42–6.

[82] Barbado D, Barbado LC, Elvira JLL, van Dieën JH, Vera-Garcia FJ. Sports-related testing protocols are required to reveal trunk stability adaptations in high-level athletes. Gait Posture 2016;49:90–6.

[83] Van Daele U, Huyvaert S, Hagman F, Duquet W, Van Gheluwe B, Vaes P. Reproducibility of postural control measurement during unstable sitting in low back pain patients. BMC Musculoskelet Disord 2007;8:1–9.

[84] Barbado D, Gomez-Illan R, Moreno-Navarro P, Valero-Conesa G, Reina R, Vera-Garcia FJ. Postural control quantification in minimally and moderately impaired persons with multiple sclerosis: the reliability of a posturographic test and its relationships with functional ability. J Sport Heal Sci 2018;00:1–8.

[85] Munoz F, Rouboa AI, Rougier PR. The balance control effects on sitting posture induced by lumbosacral orthosis wear vary depending on the level of stability. Appl Ergon 2013;44:511–6.

[86] Foroughi F, Sobhani S, Yoosefinejad AK, Motealleh A. Added value of isolated core postural control training on knee pain and function in women with patellofemoral pain syndrome: a randomized controlled trial. Arch Phys Med Rehabil 2019;100:220–9.

[87] Silfies SP, Cholewicki J, Radebold A. The effects of visual input on postural control of the lumbar spine in unstable sitting. Hum Mov Sci 2003;22:237–52.

[88] van der Burg JCE, van Wegen EEH, Rietberg MB, Kwakkel G, van Dieën JH. Postural control of the trunk during unstable sitting in Parkinson’s disease. Park Relat Disord 2006;12:492–8.

[89] Cholewicki J, Polzhofer GK, Radebold A. Postural control of trunk during unstable sitting. J Biomech 2000;33:1733–7.

[90] Preuss RA, Grenier SG, McGill SM. Postural control of the lumbar spine in unstable sitting. Arch Phys Med Rehabil 2005;86:2309–15.

[91] Chiang J, Potvin JR. The in vivo dynamic response of the human spine to rapid lateral bend perturbation. Spine (Phila Pa 1976) 2001;26:1457–64.

[92] Bazrgari B, Shirazi-Adl A, Larivière C. Trunk response analysis under sudden forward perturbations using a kinematics-driven model. J Biomech 2009;42:1193–200.

[93] Hodges P, van den Hoorn W, Dawson A, Cholewicki J. Changes in the mechanical properties of the trunk in low back pain may be associated with recurrence. J Biomech 2009;42:61–6.

[94] Kim Y, Shim JK, Son J, Pyeon HY, Yoon BC. A neuromuscular strategy to prevent spinal torsion: backward perturbation alters asymmetry of transversus abdominis muscle thickness into symmetry. Gait Posture 2013;38:231–5.

[95] Larivière C, Forget R, Vadeboncoeur R, Bilodeau M, Mecheri H. The effect of sex and chronic low back pain on back muscle reflex responses. Eur J Appl Physiol 2010;109:577–

90.

[96] Santos BR, Larivière C, Delisle A, McFadden D, Plamondon A, Imbeau D. Sudden loading perturbation to determine the reflex response of different back muscles: a reliability study. Muscle Nerve 2011;43:348–59.

[97] Vera-Garcia FJ, Elvira JLL, Brown SHM, McGill SM. Effects of abdominal stabilization maneuvers on the control of spine motion and stability against sudden trunk perturbations. J Electromyogr Kinesiol 2007;17:556–67.

[98] Santos BR, Larivière C, Delisle A, Plamondon A, Boileau PÉ, Imbeau D. A laboratory study to quantify the biomechanical responses to whole-body vibration: the influence on balance, reflex response, muscular activity and fatigue. Int J Ind Ergon 2008;38:626–39.

[99] Shahvarpour A, Shirazi-Adl A, Mecheri H, Larivière C. Trunk response to sudden forward perturbations – effects of preload and sudden load magnitudes, posture and abdominal antagonistic activation. J Electromyogr Kinesiol 2014;24:394–403.

[100] Ishida H, Suehiro T, Kurozumi C, Watanabe S. Comparison between the effectiveness of expiration and abdominal bracing maneuvers in maintaining spinal stability following sudden trunk loading. J Electromyogr Kinesiol 2016;26:125–9.

[101] Bazrgari B, Nussbaum MA, Madigan ML, Shirazi-Adl A. Soft tissue wobbling affects trunk dynamic response in sudden perturbations. J Biomech 2011;44:547–51.

[102] Granata KP, Slota GP, Wilson SE. Influence of fatigue in neuromuscular control of spinal stability. Hum Factors 2004;46:81–91.

[103] Bazrgari B, Nussbaum MA, Madigan ML. Estimation of trunk mechanical properties using system identification: effects of experimental setup and modelling assumptions. Comput Methods Biomech Biomed Engin 2012;15:1001–9.

[104] Krajcarski SR, Potvin JR, Chiang J. The in vivo dynamic response of the spine to perturbations causing rapid flexion: effects of pre-load and step input magnitude. Clin Biomech 1999;14:54–62.

[105] Lawrence BM, Mirka GA, Buckner GD. Adaptive system identification applied to the biomechanical response of the human trunk during sudden loading. J Biomech 2005;38:2472–9.

[106] Pedersen MT, Essendrop M, Skotte JH, Jørgensen K, Fallentin N. Training can modify back muscle response to sudden trunk loading. Eur Spine J 2004;13:548–52.

[107] Pedersen MT, Essendrop M, Skotte JH, Jørgensen K, Schibye B, Fallentin N. Back muscle response to sudden trunk loading can be modified by training among healthcare workers. Spine (Phila Pa 1976) 2007;32:1454–60.

[108] Skotte JH, Fallentin N, Pedersen MT, Essendrop M, Strøyer J, Schibye B. Adaptation to sudden unexpected loading of the low back—the effects of repeated trials. J Biomech 2004;37:1483–9.

[109] Thomas JS, Lavender SA, Corcos DM, Andersson GBJ. Trunk kinematics and trunk muscle activity during a rapidly applied load. J Electromyogr Kinesiol 1998;8:215–25.

[110] Thomas JS, Lavender SA, Corcos DM, Andersson GBJ. Effect of lifting belts on trunk

muscle activation during a suddenly applied load. Hum Factors 1999;41:670–6.

[111] Thrasher TA, Sin VW, Masani K, Vette AH, Craven BC, Popovic MR. Responses of the trunk to multidirectional perturbations during unsupported sitting in normal adults. J Appl Biomech 2010;26:332–40.

[112] Bobet J, Masani K, Popovic MR, Vette AH. Kinematics-based prediction of trunk muscle activity in response to multi-directional perturbations during sitting. Med Eng Phys 2018;58:56–63.

[113] Milosevic M, McConville KMV, Sejdic E, Masani K, Kyan MJ, Popovic MR. Visualization of trunk muscle synergies during sitting perturbations using self-organizing maps (SOM). IEEE Trans Biomed Eng 2012;59:2516–23.

[114] Granata KP, Slota GP, Bennett BC. Paraspinal muscle reflex dynamics. J Biomech 2004;37:241–7.

[115] Miller EM, Slota GP, Agnew MJ, Madigan ML. Females exhibit shorter paraspinal reflex latencies than males in response to sudden trunk flexion perturbations. Clin Biomech 2010;25:541–5.

[116] Gardner-Morse MG, Stokes IAF. Trunk stiffness increases with steady-state effort. J Biomech 2001;34:457–63.

[117] Stokes IAF, Fox JR, Henry SM. Trunk muscular activation patterns and responses to transient force perturbation in persons with self-reported low back pain. Eur Spine J 2006;15:658–67.

[118] Stokes IAF, Gardner-Morse M, Henry SM, Badger GJ. Decrease in trunk muscular response to perturbation with preactivation of lumbar spinal musculature. Spine (Phila Pa 1976) 2000;25:1957–64.

[119] van Drunen P, Maaswinkel E, van der Helm FCT, van Dieën JH, Happee R. Identifying intrinsic and reflexive contributions to low-back stabilization. J Biomech 2013;46:1440–6.

[120] van Dieën JH, van Drunen P, Happee R. Sensory contributions to stabilization of trunk posture in the sagittal plane. J Biomech 2018;70:219–27.

[121] Griffioen M, Maaswinkel E, Zuurmond WWA, van Dieën JH, Perez RSGM. Trunk stabilization estimated using pseudorandom force perturbations, a reliability study. J Biomech 2016;49:244–51.

[122] Granata KP, Rogers E, Moorhouse K. Effects of static flexion-relaxation on paraspinal reflex behavior. Clin Biomech 2005;20:16–24.

[123] Lee PJ, Rogers EL, Granata KP. Active trunk stiffness increases with co-contraction. J Electromyogr Kinesiol 2006;16:51–7.

[124] Moorhouse KM, Granata KP. Trunk stiffness and dynamics during active extension exertions. J Biomech 2005;38:2000–7.

[125] Navalgund A, Buford JA, Briggs MS, Givens DL. Trunk muscle reflex amplitudes increased in patients with subacute, recurrent LBP treated with a 10-week stabilization exercise program. Motor Control 2013;17:1–17.

[126] Rogers EL, Granata KP. Disturbed paraspinal reflex following prolonged flexion-relaxation

and recovery. Spine (Phila Pa 1976) 2006;31:839–45.

[127] Hendershot B, Bazrgari B, Muslim K, Toosizadeh N, Nussbaum MA, Madigan ML. Disturbance and recovery of trunk stiffness and reflexive muscle responses following prolonged trunk flexion: influences of flexion angle and duration. Clin Biomech 2011;26:250–6.

[128] Hendershot BD, Bazrgari B, Nussbaum MA. Persons with unilateral lower-limb amputation have altered and asymmetric trunk mechanical and neuromuscular behaviors estimated using multidirectional trunk perturbations. J Biomech 2013;46:1907–12.

[129] Miller EM, Bazrgari B, Nussbaum MA, Madigan ML. Effects of exercise-induced low back pain on intrinsic trunk stiffness and paraspinal muscle reflexes. J Biomech 2013;46:801–5.

[130] Cholewicki J, Greene H, Polzhofer G, Galloway M, Shah R, Radebold A. Neuromuscular function in athletes following recovery from a recent acute low back injury. J Orthop Sport Phys Ther 2002;32:568–75.

[131] McCook DT, Vicenzino B, Hodges PW. Activity of deep abdominal muscles increases during submaximal flexion and extension efforts but antagonist co-contraction remains unchanged. J Electromyogr Kinesiol 2009;19:754–62.

[132] Cholewicki J, Juluru K, Radebold A, Panjabi MM, McGill SM. Lumbar spine stability can be augmented with an abdominal belt and/or increased intra-abdominal pressure. Eur Spine J 1999;8:388–95.

[133] Cholewicki J, Lee AS, Peter Reeves N, Morrisette DC. Comparison of trunk stiffness provided by different design characteristics of lumbosacral orthoses. Clin Biomech 2010;25:110–4.

[134] Cholewicki J, Mcgill KC, Shah KR, Lee AS. The effects of a three-week use of lumbosacral orthoses on trunk muscle activity and on the muscular response to trunk perturbations. BMC Musculoskelet Disord 2010;11:1–10.

[135] Cholewicki J, Silfies SP, Shah RA, Greene HS, Reeves NP, Alvi K, et al. Delayed trunk muscle reflex responses increase the risk of low back injuries. Spine (Phila Pa 1976) 2005;30:2614–20.

[136] Cholewicki J, Simons APD, Radebold A. Effects of external trunk loads on lumbar spine stability. J Biomech 2000;33:1377–85.

[137] Kim Y, Son J, Yoon B. Intensive unilateral neuromuscular training on non-dominant side of low back improves balanced muscle response and spinal stability. Eur J Appl Physiol 2013;113:997–1004.

[138] Radebold A, Cholewicki J, Panjabi MM, Patel TC. Muscle response pattern to sudden trunk loading in healthy individuals and in patients with chronic low back pain. Spine (Phila Pa 1976) 2000;25:947–54.

[139] Reeves NP, Cholewicki J, Milner TE. Muscle reflex classification of low-back pain. J Electromyogr Kinesiol 2005;15:53–60.

[140] Cort JA, Dickey JP, Potvin JR. Trunk muscle contributions of to L 4 – 5 joint rotational stiffness following sudden trunk lateral bend perturbations. J Electromyogr Kinesiol

2013;23:1334–42.

[141] Côté JN, Patenaude I, St-Onge N, Fung J. Whiplash-associated disorders affect postural reactions to antero-posterior support surface translations during sitting. Gait Posture 2009;29:603–11.

[142] St-Onge N, Côté JN, Patenaude I, Fung J. A paradigm to assess postural responses triggered by anteroposterior translations in healthy seated individuals. Gait Posture 2009;30:417–23.

[143] Macintyre D, Cort JA. Neuromuscular response of the trunk to inertial based sudden perturbations following whole body vibration exposure. J Electromyogr Kinesiol 2014;24:977–85.

[144] Forssberg H, Hirschfeld H. Postural adjustments in sitting humans following external perturbations: muscle activity and kinematics. Exp Brain Res 1994;97:515–27.

[145] Xia T, Ankrum JA, Spratt KF, Wilder DG. Seated human response to simple and complex impacts: paraspinal muscle activity. Int J Ind Ergon 2008;38:767–74.

[146] Preuss R, Fung J. Musculature and biomechanics of the trunk in the maintenance of upright posture. J Electromyogr Kinesiol 2008;18:815–28.

[147] Stenlund TC, Lundström R, Lindroos O, Häger CK, Burström L, Neely G, et al. Seated postural neck and trunk reactions to sideways perturbations with or without a cognitive task. J Electromyogr Kinesiol 2015;25:548–56.

[148] Milosevic M, Shinya M, Masani K, Patel K, McConville KMV, Nakazawa K, et al. Anticipation of direction and time of perturbation modulates the onset latency of trunk muscle responses during sitting perturbations. J Electromyogr Kinesiol 2016;26:94–101.

[149] Zedka M, Kumar S, Narayan Y. Electromyographic response of the trunk muscles to postural perturbation in sitting subjects. J Electromyogr Kinesiol 1998;8:3–10.

[150] Lanzetta D, Cattaneo D, Pellegatta D, Cardini R. Trunk control in unstable sitting posture during functional activities in healthy subjects and patients with multiple sclerosis. Arch Phys Med Rehabil 2004;85:279–83.

[151] Prieto TE, Myklebust JB, Hoffmann RG, Lovett EG, Myklebust BM. Measures of postural steadiness: differences between healthy young and elderly adults. IEEE Trans Biomed Eng 1996;43:956–66.

[152] Collins JJ, De Luca CJ. Open-loop and closed-loop control of posture: a random-walk analysis of center-of-pressure trajectories. Exp Brain Res 1993;95:308–18.

[153] Winter DA. Biomechanics and motor control of human movement. 4th ed. New Jersey: Wiley; 2009.

[154] Bull AMJ, Berkshire FH, Amis AA. Accuracy of an electromagnetic measurement device and application to the measurement and description of knee joint motion. Proc. Inst. Mech. Eng. Part H J. Eng. Med., 1998, p. 347–55.

[155] An KN, Jacobsen MC, Berglund LJ, Chao EYS. Application of a magnetic tracking device to kinesiologic studies. J Biomech 1988;21:613–20.

[156] Pearcy MJ, Hindle RJ. New method for the non-invasive three-dimensional measurement of human back movement. Clin Biomech 1989;4:73–9.

[157] Shull PB, Jirattigalachote W, Hunt MA, Cutkosky MR, Delp SL. Quantified self and human movement: a review on the clinical impact of wearable sensing and feedback for gait analysis and intervention. Gait Posture 2014;40:11–9.

[158] Salarian A, Russmann H, Vingerhoets FJG, Dehollain C, Blanc Y, Burkhard PR, et al. Gait assessment in Parkinson's disease: toward an ambulatory system for long-term monitoring. IEEE Trans Biomed Eng 2004;51:1434–43.

[159] Sabatini AM. Quaternion-based strap-down integration method for applications of inertial sensing to gait analysis. Med Biol Eng Comput 2005;43:94–101.

[160] Rebula JR, Ojeda LV, Adamczyk PG, Kuo AD. Measurement of foot placement and its variability with inertial sensors. Gait Posture 2013;38:974–80.

[161] Lee JK, Park EJ. 3D spinal motion analysis during staircase walking using an ambulatory inertial and magnetic sensing system. Med Biol Eng Comput 2011;49:755–64.

[162] Dejnabadi H, Jolles BM, Casanova E, Fua P, Aminian K. Estimation and visualization of sagittal kinematics of lower limbs orientation using body-fixed sensors. IEEE Trans Biomed Eng 2006;53:1385–93.

[163] Schmitz A, Ye M, Shapiro R, Yang R, Noehren B. Accuracy and repeatability of joint angles measured using a single camera markerless motion capture system. J Biomech 2014;47:587–91.

[164] Schmitz A, Ye M, Boggess G, Shapiro R, Yang R, Noehren B. The measurement of in vivo joint angles during a squat using a single camera markerless motion capture system as compared to a marker based system. Gait Posture 2015;41:694–8.

[165] Corazza S, Mündermann L, Chaudhari AM, Demattio T, Cobelli C, Andriacchi TP. A markerless motion capture system to study musculoskeletal biomechanics: visual hull and simulated annealing approach. Ann Biomed Eng 2006;34:1019–29.

[166] Leardini A, Biagi F, Belvedere C, Benedetti MG. Quantitative comparison of current models for trunk motion in human movement analysis. Clin Biomech 2009;24:542–50.

[167] Cappozzo A, Della Croce U, Leardini A, Chiari L. Human movement analysis using stereophotogrammetry. Gait Posture 2005;21:186–96.

[168] Brown RH, Burstein AH, Nash CL, Schock CC. Spinal analysis using a three-dimensional radiographic technique. J Biomech 1976;9:355–65.

[169] Wong C, Zhang ZQ, Lo B, Yang GZ. Wearable sensing for solid biomechanics: a review. IEEE Sens J 2015;15:2747–60.

[170] Zijlstra W, Aminian K. Mobility assessment in older people: new possibilities and challenges. Eur J Ageing 2007;4:3–12.

[171] Allard P, Stokes IAF, Blanchi JP. Three-dimensional analysis of human movement. 1st ed. Illinois: Human Kinetics; 1995.

[172] Huiskes R, Kremers J, de Lange A, Woltring HJ, Selvik G, van Rens TJG. Analytical stereophotogrammetric determination of three-dimensional knee-joint geometry. J Biomech 1985;18:559–70.

[173] Selvik G, Alberius P, Aronson AS. A roentgen stereophotogrammetric system: construction,

calibration and technical accuracy. Acta Radiol Diagnosis 1983;24:343–52.

[174] Stevens WP. Reconstruction of three-dimensional anatomical landmark coordinates using video-based stereophotogrammetry. J Anat 1997;191:277–84.

[175] Chiari L, Della Croce U, Leardini A, Cappozzo A. Human movement analysis using stereophotogrammetry: part 2: instrumental errors. Gait Posture 2005;21:197–211.

[176] Ferrarin M, Rizzone M, Lopiano L, Recalcati M, Pedotti A. Effects of subthalamic nucleus stimulation and l-dopa in trunk kinematics of patients with Parkinson's disease. Gait Posture 2004;19:164–71.

[177] Ferrarin M, Lopiano L, Rizzone M, Lanotte M, Bergamasco B, Recalcati M, et al. Quantitative analysis of gait in Parkinson's disease: a pilot study on the effects of bilateral sub-thalamic stimulation. Gait Posture 2002;16:135–48.

[178] Wu G, Van Der Helm FCT, Veeger HEJ, Makhsous M, Van Roy P, Anglin C, et al. ISB recommendation on definitions of joint coordinate systems of various joints for the reporting of human joint motion—part II: shoulder, elbow, wrist and hand. J Biomech 2005;38:981–92.

[179] Frigo C, Carabalona R, Dalla Mura M, Negrini S. The upper body segmental movements during walking by young females. Clin Biomech 2003;18:419–25.

[180] Fantozzi S, Benedetti MG, Leardini A, Banks SA, Cappello A, Assirelli D, et al. Fluoroscopic and gait analysis of the functional performance in stair ascent of two total knee replacement designs. Gait Posture 2003;17:225–34.

[181] Allard P, Cappozzo A, Lundberg A, Vaughan CL. Three-dimensional analysis of human locomotion. 1st ed. New Jersey: Wiley; 1998.

[182] Nguyen TC, Baker R. Two methods of calculating thorax kinematics in children with myelomeningocele. Clin Biomech 2004;19:1060–5.

[183] Taylor KD, Mottier FM, Simmons DW, Cohen W, Pavlak R, Cornell DP, et al. An automated motion measurement system for clinical gait analysis. J Biomech 1982;15:505–16.

[184] Ferrigno G, Borghese NA, Pedotti A. Pattern recognition in 3D automatic human motion analysis. ISPRS J Photogramm Remote Sens 1990;45:227–46.

[185] National Research Council. Virtual reality: scientific and technological challenges. 1st ed. Washington, DC: The National Academies Press; 1995.

[186] Della Croce U, Leardini A, Chiari L, Cappozzo A. Human movement analysis using stereophotogrammetry: part 4: assessment of anatomical landmark misplacement and its effects on joint kinematics. Gait Posture 2005;21:226–37.

[187] Cappozzo A, Catani F, Della Croce U, Leardini A. Position and orientation in space of bones during movement: anatomical frame definition and determination. Clin Biomech 1995;10:171–8.

[188] Rabuffetti M, Baroni G, Ferrarin M, Ferrigno G, Pedotti A. Self-marking of anatomical landmarks for on-orbit experimental motion analysis compared to expert direct-marking. Hum Mov Sci 2002;21:439–55.

[189] Leardini A, Chiari A, Della Croce U, Cappozzo A. Human movement analysis using stereophotogrammetry: part 3: soft tissue artifact assessment and compensation. Gait Posture 2005;21:212–25.

[190] Kavcic N, Grenier S, McGill SM. Determining the stabilizing role of individual torso muscles during rehabilitation exercises. Spine (Phila Pa 1976) 2004;29:1254–65.

[191] Fortin C, Nadeau S, Labelle H. Inter-trial and test-retest reliability of kinematic and kinetic gait parameters among subjects with adolescent idiopathic scoliosis. Eur Spine J 2008;17:204–16.

[192] Vette AH, Yoshida T, Thrasher TA, Masani K, Popovic MR. A complete, non-lumped, and verifiable set of upper body segment parameters for three-dimensional dynamic modeling. Med Eng Phys 2011;33:70–9.

[193] Vette AH, Yoshida T, Thrasher TA, Masani K, Popovic MR. A comprehensive three-dimensional dynamic model of the human head and trunk for estimating lumbar and cervical joint torques and forces from upper body kinematics. Med Eng Phys 2012;34:640–9.

[194] Ayatollahzadeh S. Human trunk multi-segment kinematics: sensitivity to experimental errors. University of Toronto, 2014.

[195] Kadaba MP, Ramakrishnan HK, Wootten ME. Measurement of lower extremity kinematics during level walking. J Orthop Res 1990;8:383–92.

[196] Robertson G, Caldwell G, Hamill J, Kamen G, Whittlesey S. Research methods in biomechanics. 1st ed. Illinois: Human Kinetics; 2004.

[197] Cole GK, Nigg BM, Ronsky JL, Yeadon MR. Application of the joint coordinate system to three-dimensional joint attitude and movement representation: a standardization proposal. J Biomech Eng 1993;115:344–9.

[198] Craig JJ. Introduction to robotics: mechanics and control. 3rd ed. United Kingdom: Prentice Hall; 2004.

[199] O'Connor CM, Thorpe SK, O'Malley MJ, Vaughan CL. Automatic detection of gait events using kinematic data. Gait Posture 2007;25:469–74.

[200] Basmajian JV, De Luca CJ. Muscles alive: their functions revealed by electromyography. 2nd ed. Maryland: Lippincott Williams & Wilkins; 1985.

[201] Drake JDM, Callaghan JP. Elimination of electrocardiogram contamination from electromyogram signals: an evaluation of currently used removal techniques. J Electromyogr Kinesiol 2006;16:175–87.

[202] Soderberg GL, Knutson LM. A guide for use and interpretation of kinesiologic electromyographic data. Phys Ther 2000;80:485–98.

[203] Clancy EA, Morin EL, Merletti R. Sampling, noise-reduction and amplitude estimation issues in surface electromyography. J Electromyogr Kinesiol 2002;12:1–16.

[204] Allen TR, Brookham RL, Cudlip AC, Dickerson CR. Comparing surface and indwelling electromyographic signals of the supraspinatus and infraspinatus muscles during submaximal axial humeral rotation. J Electromyogr Kinesiol 2013;23:1343–9.

[205] Dankaerts W, O'Sullivan PB, Burnett AF, Straker LM, Danneels LA. Reliability of EMG

measurements for trunk muscles during maximal and sub-maximal voluntary isometric contractions in healthy controls and CLBP patients. J Electromyogr Kinesiol 2004;14:333–42.

[206] Soderberg GL, Cook TM. Electromyography in biomechanics. Phys Ther 1984;64:1813–20.

[207] McMulkin ML, Woldstad JC, Hughes RE. Torso loading via a harness method activates trunk muscles less than a hand loading method. J Biomech 1998;31:391–5.

[208] Staudenmann D, Potvin JR, Kingma I, Stegeman DF, van Dieën JH. Effects of EMG processing on biomechanical models of muscle joint systems: sensitivity of trunk muscle moments, spinal forces, and stability. J Biomech 2007;40:900–9.

[209] Redfern MS, Hughes RE, Chaffin DB. High-pass filtering to remove electrocardiographic interference from torso EMG recordings. Clin Biomech 1993;8:44–8.

[210] Van Der Burg JCE, Kingma I, Van Dieën JH. Is the trunk movement more perturbed after an asymmetric than after a symmetric perturbation during lifting? J Biomech 2004;37:1071–7.

[211] Gagnon D, Larivière C, Loisel P. Comparative ability of EMG, optimization, and hybrid modelling approaches to predict trunk muscle forces and lumbar spine loading during dynamic sagittal plane lifting. Clin Biomech 2001;16:359–72.

[212] Potvin JR, Brown SHM. Less is more: high pass filtering, to remove up to 99% of the surface EMG signal power, improves EMG-based biceps brachii muscle force estimates. J Electromyogr Kinesiol 2004;14:389–99.

[213] Albertus-Kajee Y, Tucker R, Derman W, Lamberts RP, Lambert MI. Alternative methods of normalising EMG during running. J Electromyogr Kinesiol 2011;21:579–86.

[214] Rantalainen T, Kłodowski A, Piitulainen H. Effect of innervation zones in estimating biceps brachii force-EMG relationship during isometric contraction. J Electromyogr Kinesiol 2012;22:80–7.

[215] Mitchell MD, Yarossi MB, Pierce DN, Garbarini EL, Forrest GF. Reliability of surface EMG as an assessment tool for trunk activity and potential to determine neurorecovery in SCI. Spinal Cord 2015;53:368–74.

[216] Larivière C, Gagnon D, Loisel P. The comparison of trunk muscles EMG activation between subjects with and without chronic low back pain during flexion-extension and lateral bending tasks. J Electromyogr Kinesiol 2000;10:79–91.

[217] Cholewicki J, VanVliet IV JJ. Relative contribution of trunk muscles to the stability of the lumbar spine during isometric exertions. Clin Biomech 2002;17:99–105.

[218] Dolan P, Kingma I, De Looze MP, van Dieen JH, Toussaint HM, Baten CTM, et al. An EMG technique for measuring spinal loading during asymmetric lifting. Clin Biomech 2001;16:S17–24.

[219] Laursen B, Jensen BR, Németh G, Sjøgaard G. A model predicting individual shoulder muscle forces based on relationship between electromyographic and 3D external forces in static position. J Biomech 1998;31:731–9.

[220] Madeleine P, Bajaj P, Søgaard K, Arendt-Nielsen L. Mechanomyography and electromyography force relationships during concentric, isometric and eccentric contractions. J Electromyogr Kinesiol 2001;11:113–21.

[221] Kamen G, Caldwell GE. Physiology and interpretation of the electromyogram. J Clin Neurophysiol 1996;13:366–84.

[222] Burden A. How should we normalize electromyograms obtained from healthy participants? what we have learned from over 25 years of research. J Electromyogr Kinesiol 2010;20:1023–35.

[223] McGill SM, Kavcic NS, Harvey E. Sitting on a chair or an exercise ball: various perspectives to guide decision making. Clin Biomech 2006;21:353–60.

[224] Cholewicki J, McGill SM. Mechanical stability of the in vivo lumbar spine: implications for injury and chronic low back pain. Clin Biomech 1996;11:1–15.

[225] Potvin JR, Norman RW, McGill SM. Mechanically corrected EMG for the continuous estimation of erector spinae muscle loading during repetitive lifting. Eur J Appl Physiol 1996;74:119–32.

[226] Sutherland DH. The evolution of clinical gait analysis part III – kinetics and energy assessment. Gait Posture 2005;21:447–61.

[227] Hof AL, Gazendam MGJ, Sinke WE. The condition for dynamic stability. J Biomech 2005;38:1–8.

[228] Major MJ, Stine RL, Gard SA. The effects of walking speed and prosthetic ankle adapters on upper extremity dynamics and stability-related parameters in bilateral transtibial amputee gait. Gait Posture 2013;38:858–63.

[229] Begg RK, Wytch R, Major RE. Instrumentation used in clinical gait studies: a review. J Med Eng Technol 1989;13:290–5.

[230] Beckham G, Suchomel T, Mizuguchi S. Force plate use in performance monitoring and sport science testing. New Stud Athl 2014;29:25–37.

[231] Psycharakis SG, Miller S. Estimation of errors in force platform data. Res Q Exerc Sport 2006;77:514–8.

[232] Higson GR. Recent advances in strain gauges. J Sci Instrum 1964;41:405–14.

[233] Wang DF, Lou X, Bao A, Yang X, Zhao J. A temperature compensation methodology for piezoelectric based sensor devices. Appl Phys Lett 2017;111:1–5.

[234] Liu J, Luo X, Liu J, Li M, Qin L. Development of a commercially viable piezoelectric force sensor system for static force measurement. Meas Sci Technol 2017;28:1–7.

[235] Williams AD, Boser QA, Kumawat AS, Agarwal K, Rouhani H, Vette AH. Design and evaluation of an instrumented wobble board for assessing and training dynamic seated balance. J Biomech Eng 2018;140:1–10.

[236] Wu G, Siegler S, Allard P, Kirtley C, Leardini A, Rosenbaum D, et al. ISB recommendation on definitions of joint coordinate system of various joints for the reporting of human joint motion—part I: ankle, hip, and spine. J Biomech 2002;35:543–8.

[237] Nilsson J, Panizza M, Hallett M. Principles of digital sampling of a physiologic signal. Electroencephalogr Clin Neurophysiol 1993;89:349–58.

[238] Moin P. Fundamentals of engineering numerical analysis. 2nd ed. New York: Cambridge University Press; 2010.

[239] Press WH, Vetterling WT. Numerical recipes. 1st ed. New York: Cambridge University Press; 1989.

[240] Popovic MR, Thrasher TA. Neuroprostheses. Encycl Biomater Biomed Eng 2004:1056–65.

[241] Callaghan JP, Gunning JL, McGill SM. The relationship between lumbar spine load and muscle activity during extensor exercises. Phys Ther 1998;78:8–18.

[242] van den Tillaar R, Andersen V, Saeterbakken AH. Comparison of muscle activation and performance during 6 RM, two-legged free-weight squats. Kinesiol Slov 2014;20:5–16.

[243] Box GEP, Jenkins GM, Reinsel GC. Time series analysis: forecasting and control. 3rd ed. New Jersey: Prentice Hall; 1994.

[244] Söderström T, Stoica P. System identification. 1st ed. New Jersey: Prentice Hall; 1989.

[245] Gatev P, Thomas S, Kepple T, Hallett M. Feedforward ankle strategy of balance during quiet stance in adults. J Physiol 1999;514:915–28.

[246] Fujio K, Obata H, Kawashima N, Nakazawa K. The effects of temporal and spatial predictions on stretch reflexes of ankle flexor and extensor muscles while standing. PLoS One 2016;11:1–14.

[247] Masani K, Vette AH, Popovic MR. Controlling balance during quiet standing: proportional and derivative controller generates preceding motor command to body sway position observed in experiments. Gait Posture 2006;23:164–72.

[248] Masani K, Vette AH, Kawashima N, Popovic MR. Neuromusculoskeletal torque-generation process has a large destabilizing effect on the control mechanism of quiet standing. J Neurophysiol 2008;100:1465–75.

[249] Lametti DR, Houle G, Ostry DJ. Control of movement variability and the regulation of limb impedance. J Neurophysiol 2007;98:3516–24.

[250] Milosevic M, Yokoyama H, Grangeon M, Masani K, Popovic MR, Nakazawa K, et al. Muscle synergies reveal impaired trunk muscle coordination strategies in individuals with thoracic spinal cord injury. J Electromyogr Kinesiol 2017;36:40–8.

[251] Massion J. Movement, posture and equilibrium: interaction and coordination. Prog Neurobiol 1992;38:35–56.

[252] Tjernström F, Fransson PA, Patel M, Magnusson M. Postural control and adaptation are influenced by preceding postural challenges. Exp Brain Res 2010;202:613–21.

[253] Chen CL, Lou SZ, Wu HW, Wu SK, Yeung KT, Su FC. Effects of the type and direction of support surface perturbation on postural responses. J Neuroeng Rehabil 2014;11:1–12.

[254] Mancini M, Horak FB. The relevance of clinical balance assessment tools to differentiate balance deficits. Eur J Phys Rehabil Med 2010;46:239–48.

[255] Horak FB, Henry SM, Shumway-Cook A. Postural perturbations: new insights for treatment

of balance disorders. Phys Ther 1997;77:517–33.

[256] Vette AH, Sanin E, Bulsen A, Morris A, Masani K, Popovic MR. A portable and automated postural perturbation system for balance assessment, training, and neuromuscular system identification. J Med Device 2008;2:1–9.

[257] Chen CL, Lee JY, Horng RF, Lou SZ, Su FC. Development of a three-degrees-of-freedom moveable platform for providing postural perturbations. Proc. Inst. Mech. Eng. Part H J. Eng. Med., 2009, p. 87–97.

[258] Bassi Luciani L, Genovese V, Monaco V, Odetti L, Cattin E, Micera S. Design and evaluation of a new mechatronic platform for assessment and prevention of fall risks. J Neuroeng Rehabil 2012;9:1–13.

[259] Motek Medical. Gait real-time analysis interactive lab 2018. https://www.motekforcelink.com/product/grail/ (accessed June 26, 2018).

[260] Motek Medical. Dynamic stability and balance learning environment 2018. https://www.motekforcelink.com/product/dynstable/ (accessed June 26, 2018).

[261] Peterka RJ. Sensorimotor integration in human postural control. J Neurophysiol 2002;88:1097–118.

[262] Logan D, Kiemel T, Jeka JJ. Asymmetric sensory reweighting in human upright stance. PLoS One 2014;9:1–10.

[263] Fung J, Johnstone E. Lost in space: multi-axial and multi-dimensional surface perturbations delivered by a novel motion base device. Soc. Neurosci., 1998, p. 1158.

[264] Sinitski EH, Lemaire ED, Baddour N. Characteristics of a dual force plate system embedded in a six degree of freedom motion platform. 2013 IEEE Int. Symp. Med. Meas. Appl., 2013, p. 241–5.

[265] Sinitski EH, Lemaire ED, Baddour N. Evaluation of motion platform embedded with force plate-instrumented treadmill. J Rehabil Res Dev 2015;52:221–33.

[266] Pagnacco G, Silva A, Oggero E, Berme N. Inertially compensated force plate: a means for quantifying subject's ground reaction forces in non-inertial conditions. Biomed Sci Instrum 2000;36:397–402.

[267] Hnat SK, van Basten BJH, van den Bogert AJ. Compensation for inertial and gravity effects in a moving force platform. J Biomech 2018;75:96–101.

[268] Welch TDJ, Ting LH. Mechanisms of motor adaptation in reactive balance control. PLoS One 2014;9:1–18.

[269] Chvatal SA, Ting LH. Common muscle synergies for balance and walking. Front Comput Neurosci 2013;7:1–14.

[270] Torres-Oviedo G, Ting LH. Muscle synergies characterizing human postural responses. J Neurophysiol 2007;98:2144–56.

[271] Torres-Oviedo G, Ting LH. Subject-specific muscle synergies in human balance control are consistent across different biomechanical contexts. J Neurophysiol 2010;103:3084–98.

[272] Carpenter MG, Allum JHJ, Honegger F. Directional sensitivity of stretch reflexes and

balance corrections for normal subjects in the roll and pitch planes. Exp Brain Res 1999;129:93–113.

[273] Oude Nijhuis LB, Allum JHJ, Borm GF, Honegger F, Overeem S, Bloem BR. Directional sensitivity of “first trial” reactions in human balance control. J Neurophysiol 2009;101:2802–14.

[274] Oude Nijhuis LB, Allum JHJ, Nanhoe-Mahabier W, Bloem BR. Influence of perturbation velocity on balance control in Parkinson’s disease. PLoS One 2014;9:1–7.

[275] Van Der Kooij H, Van Asseldonk E, Van Der Helm FCT. Comparison of different methods to identify and quantify balance control. J Neurosci Methods 2005;145:175–203.

[276] Engelhart D, Boonstra TA, Aarts RGKM, Schouten AC, van der Kooij H. Comparison of closed-loop system identification techniques to quantify multi-joint human balance control. Annu Rev Control 2015;41:58–70.

[277] Kiemel T, Zhang Y, Jeka JJ. Identification of neural feedback for upright stance in humans: stabilization rather than sway minimization. J Neurosci 2011;31:15144–53.

Appendices

Appendix A: Chapter 3 – Detailed Description of Experimental Data Analysis

A1 – Wobble Board Coordinate System

Using the wobble board markers (Figure A1), the coordinate system of the wobble board (*WCS*) was defined as follows: (1) the x_w axis points to the left from board back right (*BBR*) to board back left (*BBL*); (2) an auxiliary vector (AUX_w) points from *BBR* to board front left (*BFL*); (3) the z_w axis is perpendicular to the plane formed by the x_w axis and AUX_w, pointing superiorly; and (4) the y_w axis is perpendicular to the x_w and z_w axes, pointing posteriorly.

The x_w, y_w, and z_w axes were calculated using the following equations. The x_w axis was calculated using:

$$x_w = \frac{BBL - BBR}{\|BBL - BBR\|} \tag{A1}$$

AUX_w was calculated using:

$$AUX_w = \frac{BFL - BBR}{\|BFL - BBR\|} \tag{A2}$$

The z_w axis was calculated using:

$$z_w = AUX_w \times x_w \tag{A3}$$

Finally, the y_w axis was calculated using:

$$y_w = z_w \times x_w \tag{A4}$$

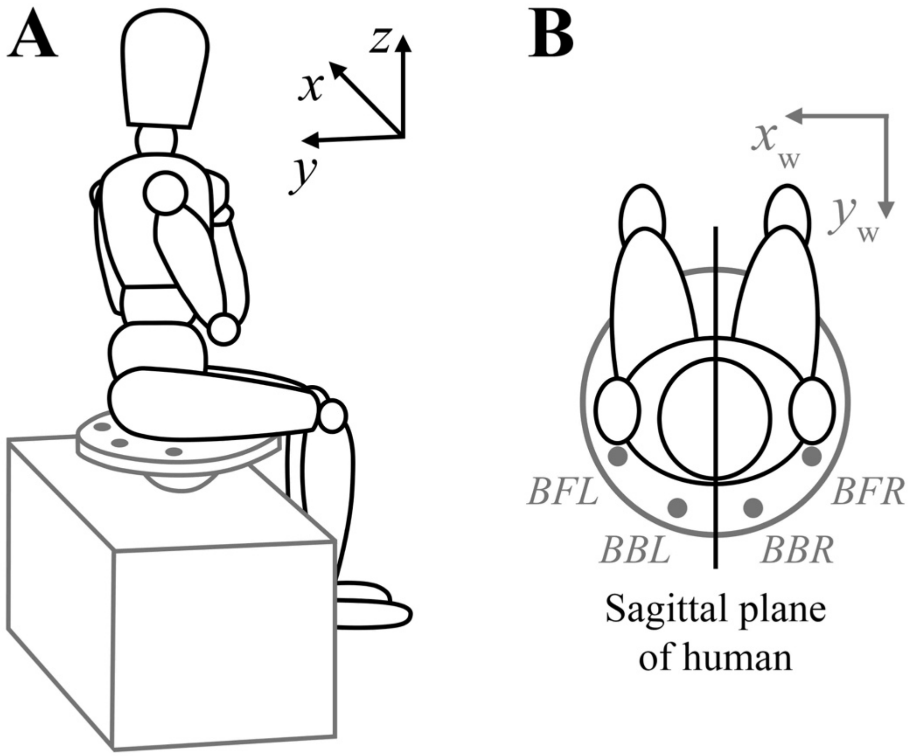

Figure A1: Schematic of wobble board balancing (A); and aerial view of wobble board-human dynamic system (B), with the following markers attached: board front left (*BFL*), board back left (*BBL*), board back right (*BBR*), and board front right (*BFR*). In (A), the orientation of the global coordinate system relative to the starting orientation of the participant is shown. In (B), the orientation of the local coordinate system of the wobble board relative to the sagittal plane of the participant is shown. Specifically, the y axis of the wobble board (y_w) was aligned with the sagittal plane of the participant.

A2 – Pelvis Coordinate System

Using the pelvis markers (Figure A2), the coordinate system of the pelvis (*PCS*) was defined as follows [1]: (1) the x_p axis points to the left from the right anterior superior iliac spine (*RASIS*) to the left anterior superior iliac spine (*LASIS*); (2) an auxiliary vector (AUX_p) is perpendicular to the plane formed by *LASIS*, *RASIS*, and the mid-point between the left posterior superior iliac spine (*LPSIS*) and the right posterior superior iliac spine (*RPSIS*), pointing superiorly; (3) the y_p axis is perpendicular to the plane formed by the x_p axis and AUX_p, pointing posteriorly; and (4) the z_p axis is perpendicular to the x_t and y_t axes, pointing superiorly.

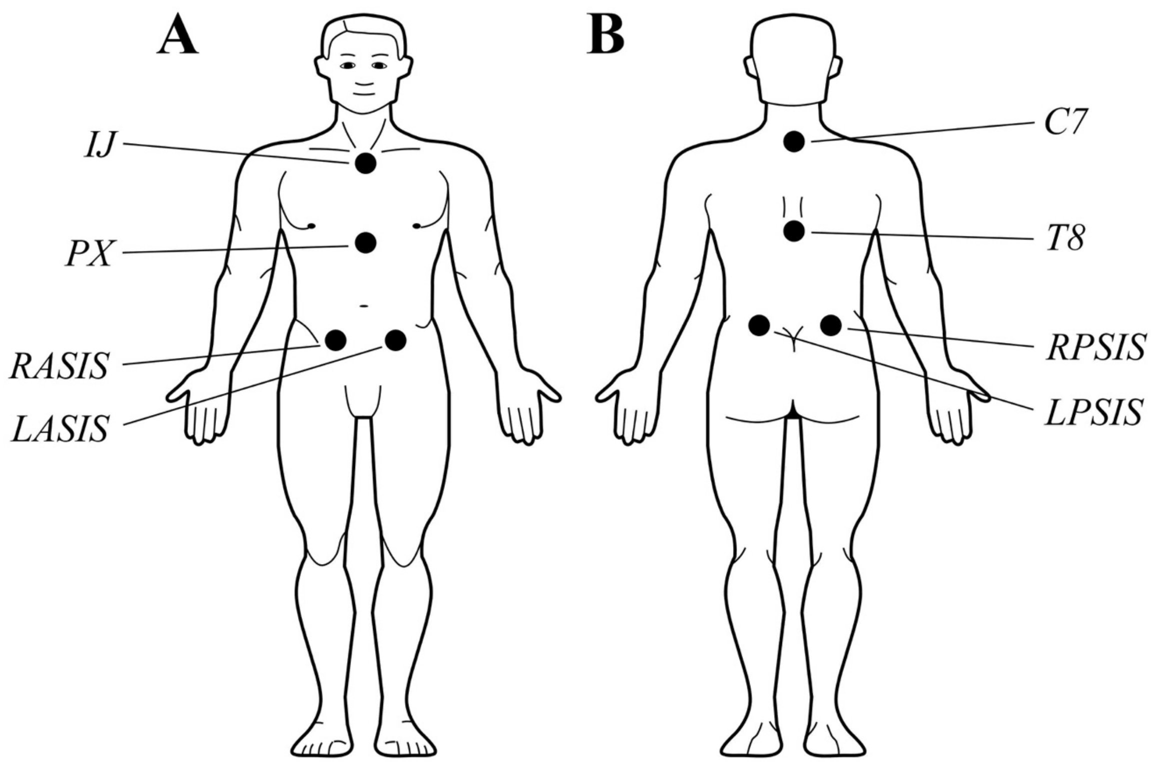

Figure A2: Placement of reflective markers on the participant's body, tracked by the motion capture system for establishing pelvis [1] and trunk [2] coordinate systems and computing three-dimensional angular kinematics. A: Anterior view showing: pelvis markers on the left and right anterior superior iliac spine (*LASIS* and *RASIS*); and trunk markers on the deepest point of the incisura jugularis (*IJ*) and the processus xiphoideus (*PX*). B: Posterior view showing: pelvis markers on the left and right posterior superior iliac spine (*LPSIS* and *RPSIS*); and trunk markers on the seventh cervical vertebra (*C7*) and eighth thoracic vertebra (*T8*).

The x_p, y_p, and z_p axes were calculated using the following equations. The x_p axis was calculated using:

$$x_p = \frac{LASIS - RASIS}{\|LASIS - RASIS\|} \tag{A5}$$

AUX_p was calculated using:

$$AUX_p = \frac{(RASIS - 0.5(LPSIS + RPSIS)) \times (LASIS - 0.5(LPSIS + RPSIS))}{\|(RASIS - 0.5(LPSIS + RPSIS)) \times (LASIS - 0.5(LPSIS + RPSIS))\|} \quad \text{(A6)}$$

The y_p axis was calculated using:

$$y_p = AUX_p \times x_p \quad \text{(A7)}$$

Finally, the z_p axis was calculated using:

$$z_p = x_p \times y_p \quad \text{(A8)}$$

A3 – Trunk Coordinate System

Using the trunk markers (Figure A2), the coordinate system of the trunk (*TCS*) was defined as follows [2]: (1) the z_t axis points superiorly from the mid-point between the eighth thoracic vertebra (*T8*) and processus xiphoideus (*PX*) to the mid-point between the seventh cervical vertebra (*C7*) and deepest point of the incisura jugularis (*IJ*); (2) the x_t axis is perpendicular to the plane formed by *C7*, *IJ*, and the mid-point between *T8* and *PX*, pointing to the left; and (3) the y_t axis is perpendicular to the x_t and z_t axes, pointing posteriorly.

The x_t, y_t, and z_t axes were calculated using the following equations. The z_t axis was calculated using:

$$z_t = \frac{0.5(C7 + IJ) - 0.5(T8 + PX)}{\|0.5(C7 + IJ) - 0.5(T8 + PX)\|} \quad \text{(A9)}$$

The x_t axis was calculated using:

$$x_t = \frac{(C7 - 0.5(T8 + PX)) \times (IJ - 0.5(T8 + PX))}{\|(C7 - 0.5(T8 + PX)) \times (IJ - 0.5(T8 + PX))\|} \quad \text{(A10)}$$

Finally, the y_t axis was calculated using:

$$y_t = z_t \times x_t \quad \text{(A11)}$$

A4 – Wobble Board, Pelvis, and Trunk Rotation Matrices

The rotation matrix from the global coordinate system (*GCS*) (Figure A1A) to *WCS*, R_w, was calculated using [3]:

$$R_w = \begin{bmatrix} r_{11} & r_{12} & r_{13} \\ r_{21} & r_{22} & r_{23} \\ r_{31} & r_{32} & r_{33} \end{bmatrix} = \begin{bmatrix} x_w \cdot x & y_w \cdot x & z_w \cdot x \\ x_w \cdot y & y_w \cdot y & z_w \cdot y \\ x_w \cdot z & y_w \cdot z & z_w \cdot z \end{bmatrix} = \begin{bmatrix} x_w & y_w & z_w \end{bmatrix} \quad \text{(A12)}$$

where it is noted that $x = [1\ 0\ 0]^T$, $y = [0\ 1\ 0]^T$, and $z = [0\ 0\ 1]^T$.

The rotation matrix from *GCS* to *PCS*, R_p, was calculated using [3]:

$$R_p = \begin{bmatrix} r_{11} & r_{12} & r_{13} \\ r_{21} & r_{22} & r_{23} \\ r_{31} & r_{32} & r_{33} \end{bmatrix} = \begin{bmatrix} x_p \cdot x & y_p \cdot x & z_p \cdot x \\ x_p \cdot y & y_p \cdot y & z_p \cdot y \\ x_p \cdot z & y_p \cdot z & z_p \cdot z \end{bmatrix} = \begin{bmatrix} x_p & y_p & z_p \end{bmatrix} \quad \text{(A13)}$$

The rotation matrix from *GCS* to *TCS*, R_t, was calculated using [3]:

$$R_t = \begin{bmatrix} r_{11} & r_{12} & r_{13} \\ r_{21} & r_{22} & r_{23} \\ r_{31} & r_{32} & r_{33} \end{bmatrix} = \begin{bmatrix} x_t \cdot x & y_t \cdot x & z_t \cdot x \\ x_t \cdot y & y_t \cdot y & z_t \cdot y \\ x_t \cdot z & y_t \cdot z & z_t \cdot z \end{bmatrix} = \begin{bmatrix} x_t & y_t & z_t \end{bmatrix} \quad \text{(A14)}$$

A5 – Wobble Board, Pelvis, and Trunk Angles

The three-dimensional angles of the wobble board, pelvis, and trunk were extracted using a Cardan rotation sequence according to [4]:

$$\begin{aligned} LB &= \operatorname{atan2}\left(r_{13}, \sqrt{r_{23}^2 + r_{33}^2}\right) \\ F/E &= \operatorname{atan2}\left(-\frac{r_{23}}{c_{LB}}, \frac{r_{33}}{c_{LB}}\right) \\ Rot &= \operatorname{atan2}\left(-\frac{r_{12}}{c_{LB}}, \frac{r_{11}}{c_{LB}}\right) \end{aligned} \quad \text{(A15)}$$

where $c_{LB} = \cos(LB)$, atan2 is the four-quadrant inverse tangent, and r_{ij} are the entries of R_w, R_p, or R_t.

A6 – Posturographic Measures

The range of the angle (*RANGE*), root mean square of the angle (*RMS*), and mean of the absolute angular velocity (*MVELO*) were calculated for *F/E* (and similarly for *LB*) as follows. $RANGE_{F/E}$ was calculated using [5]:

$$RANGE_{F/E} = \max_{F/E} - \min_{F/E} \tag{A16}$$

where $\max_{F/E}$ and $\min_{F/E}$ are the maximum and minimum values in an F/E time series, respectively.

$RMS_{F/E}$ was calculated using [5]:

$$RMS_{F/E} = \sqrt{\frac{1}{N}\sum_{i=1}^{N} F/E(i)^2} \tag{A17}$$

where N is the number of samples of an F/E time series.

$MVELO_{F/E}$ was calculated using [5]:

$$MVELO_{F/E} = \frac{1}{T}\sum_{i=1}^{N-1} \left|F/E(i+1) - F/E(i)\right| \tag{A18}$$

where T is the length in time of an F/E time series (30 seconds).

References for Appendix A

[1] Wu G, Siegler S, Allard P, Kirtley C, Leardini A, Rosenbaum D, et al. ISB recommendation on definitions of joint coordinate system of various joints for the reporting of human joint motion—part I: ankle, hip, and spine. J Biomech 2002;35:543–8.

[2] Wu G, Van Der Helm FCT, Veeger HEJ, Makhsous M, Van Roy P, Anglin C, et al. ISB recommendation on definitions of joint coordinate systems of various joints for the reporting of human joint motion—part II: shoulder, elbow, wrist and hand. J Biomech 2005;38:981–92.

[3] Robertson G, Caldwell G, Hamill J, Kamen G, Whittlesey S. Research methods in biomechanics. 1st ed. Illinois: Human Kinetics; 2004.

[4] Craig JJ. Introduction to robotics: mechanics and control. 3rd ed. United Kingdom: Prentice Hall; 2004.

[5] Prieto TE, Myklebust JB, Hoffmann RG, Lovett EG, Myklebust BM. Measures of postural steadiness: differences between healthy young and elderly adults. IEEE Trans Biomed Eng 1996;43:956–66.

Appendix B: Chapter 3 – Results for the Posturographic Measures

Table B1: Posturographic time-domain measures for wobble board (WB), pelvis, and trunk kinematics. Shown are the range of the angle (*RANGE*), root mean square of the angle (*RMS*), and mean of the absolute angular velocity (*MVELO*) for flexion/extension (*F/E*) and lateral bending (*LB*) under the Base 1 Eyes Closed (B1EC) and Base 2 Eyes Open (B2EO) conditions. All values are presented as mean ± standard deviation (presented variability is *inter-participant*). A two-tailed, paired t-test revealed statistically significant differences between WB and pelvis kinematics and between WB and trunk kinematics for all measures, angles, and task conditions ($p < 1\times10^{-2}$; 24 comparisons) (*see Table B2 for p-values*).

Measures		**WB**		**Pelvis**		**Trunk**	
		B1EC	**B2EO**	**B1EC**	**B2EO**	**B1EC**	**B2EO**
RANGE **[deg]**	***F/E***	7.99 ± 3.24	9.57 ± 4.55	3.25 ± 0.83	4.85 ± 2.74	4.24 ± 1.16	5.34 ± 1.84
	LB	7.68 ± 3.02	11.8 ± 4.05	3.24 ± 1.20	4.71 ± 1.68	3.81 ± 1.51	4.72 ± 1.80
RMS **[deg]**	***F/E***	1.60 ± 0.67	1.84 ± 0.83	0.63 ± 0.14	0.94 ± 0.63	0.87 ± 0.21	1.13 ± 0.42
	LB	1.46 ± 0.62	2.07 ± 0.88	0.64 ± 0.27	0.83 ± 0.30	0.74 ± 0.24	0.82 ± 0.26
MVELO **[deg/s]**	***F/E***	2.60 ± 0.89	2.96 ± 1.10	1.29 ± 0.50	1.79 ± 0.85	1.63 ± 0.73	1.65 ± 0.41
	LB	2.61 ± 0.69	4.07 ± 1.64	1.36 ± 0.58	1.94 ± 0.81	1.41 ± 0.66	1.58 ± 0.62

Table B2: Two-tailed, paired *t*-test *p*-values for comparisons of posturographic time-domain measures between wobble board (WB) and pelvis kinematics and between WB and trunk kinematics. Shown are values for comparisons of the range of the angle (*RANGE*), root mean square of the angle (*RMS*), and mean of the absolute angular velocity (*MVELO*) for flexion/extension (*F/E*) and lateral bending (*LB*) under the Base 1 Eyes Closed (B1EC) and Base 2 Eyes Open (B2EO) conditions.

Measures		WB and Pelvis		WB and Trunk	
		B1EC	**B2EO**	**B1EC**	**B2EO**
RANGE	***F/E***	6.61×10^{-6}	1.63×10^{-5}	6.82×10^{-5}	2.19×10^{-3}
	LB	3.79×10^{-6}	3.22×10^{-5}	8.70×10^{-6}	2.32×10^{-6}
RMS	***F/E***	2.69×10^{-5}	1.11×10^{-5}	9.52×10^{-5}	3.90×10^{-3}
	LB	8.10×10^{-6}	2.17×10^{-4}	5.33×10^{-5}	7.23×10^{-5}
MVELO	***F/E***	1.76×10^{-8}	8.29×10^{-7}	1.98×10^{-6}	1.69×10^{-4}
	LB	1.12×10^{-8}	2.44×10^{-4}	1.95×10^{-7}	1.45×10^{-5}

Appendix C: Chapter 4 – Detailed Description of Study Methods

C1 – Electromyography Electrode Placement

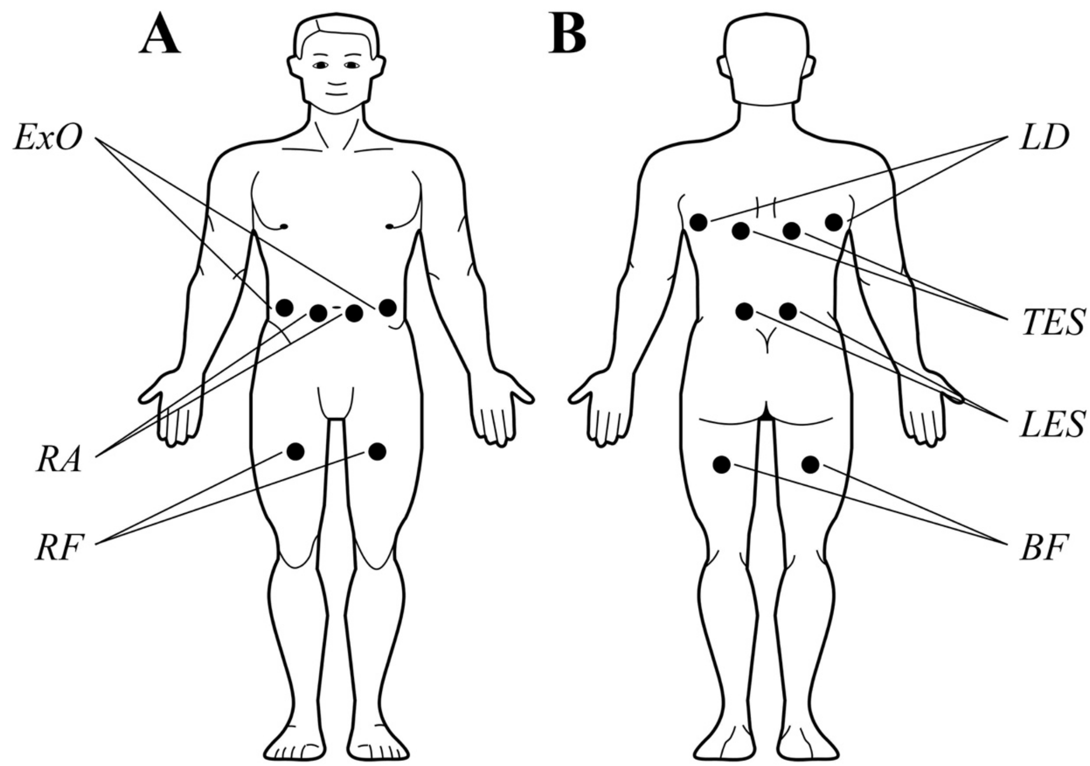

Figure C1: Placement of electromyography electrodes on the participant's body, for recording the electrical activity of seven trunk and upper leg muscle groups [1–3]. A: Anterior view showing the: rectus abdominis (*RA*), external oblique (*ExO*), and rectus femoris (*RF*) electrodes. B: Posterior view showing the: latissimus dorsi (*LD*), thoracic erector spinae (*TES*), lumbar erector spinae (*LES*), and biceps femoris (*BF*) electrodes.

C2 – Wobble Board Coordinate System

Using the wobble board markers (Figure C2), the coordinate system of the wobble board (*WCS*) was defined as follows: (1) the x_w axis points to the left from board back right (*BBR*) to board back left (*BBL*); (2) an auxiliary vector (*AUX*) points from *BBR* to board front left (*BFL*); (3) the z_w axis is perpendicular to the plane formed by the x_w axis and AUX, pointing superiorly; and (4) the y_w axis is perpendicular to the x_w and z_w axes, pointing posteriorly.

The x_w, y_w, and z_w axes were calculated using the following equations. The x_w axis was calculated using:

$$x_w = \frac{BBL - BBR}{\|BBL - BBR\|} \tag{C1}$$

AUX was calculated using:

$$AUX = \frac{BFL - BBR}{\|BFL - BBR\|} \tag{C2}$$

The z_w axis was calculated using:

$$z_w = AUX \times x_w \tag{C3}$$

Finally, the y_w axis was calculated using:

$$y_w = z_w \times x_w \tag{C4}$$

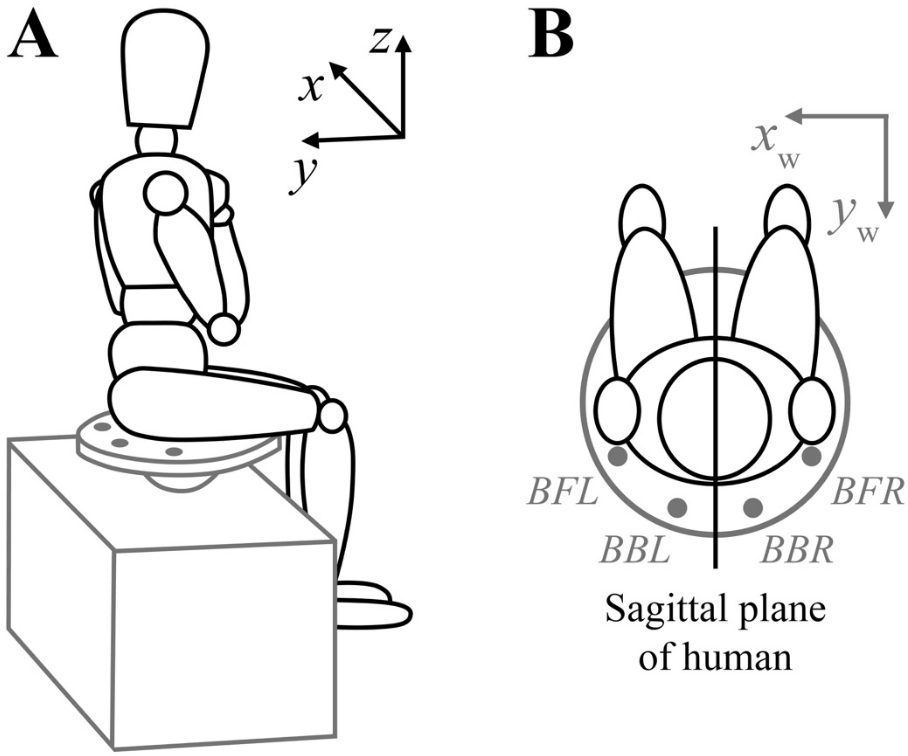

Figure C2: Schematic of wobble board balancing (A); and aerial view of wobble board-human dynamic system (B), with the following markers attached: board front left (*BFL*), board back left (*BBL*), board back right (*BBR*), and board front right (*BFR*). In (A), the orientation of the global coordinate system relative to the starting orientation of the participant is shown. In (B), the orientation of the local coordinate system of the wobble board relative to the sagittal plane of the participant is shown. Specifically, the y axis of the wobble board (y_w) was aligned with the sagittal plane of the participant.

C3 – Wobble Board Rotation Matrix

The rotation matrix from the global coordinate system (*GCS*) (Figure C2A) to *WCS*, R_w, was calculated using [4]:

$$R_w = \begin{bmatrix} r_{11} & r_{12} & r_{13} \\ r_{21} & r_{22} & r_{23} \\ r_{31} & r_{32} & r_{33} \end{bmatrix} = \begin{bmatrix} x_w \cdot x & y_w \cdot x & z_w \cdot x \\ x_w \cdot y & y_w \cdot y & z_w \cdot y \\ x_w \cdot z & y_w \cdot z & z_w \cdot z \end{bmatrix} = \begin{bmatrix} x_w & y_w & z_w \end{bmatrix} \tag{C5}$$

where it is noted that $x = [1\ 0\ 0]^T$, $y = [0\ 1\ 0]^T$, and $z = [0\ 0\ 1]^T$ are the axes of *GCS* (Figure C2A).

C4 – Wobble Board Angles

The three-dimensional angles of the wobble board were extracted using a Cardan rotation sequence according to [5]:

$$\begin{aligned} ML &= \operatorname{atan2}\left(r_{13}, \sqrt{r_{23}^2 + r_{33}^2}\right) \\ AP &= \operatorname{atan2}\left(-\frac{r_{23}}{c_{ML}}, \frac{r_{33}}{c_{ML}}\right) \\ Rot &= \operatorname{atan2}\left(-\frac{r_{12}}{c_{ML}}, \frac{r_{11}}{c_{ML}}\right) \end{aligned} \tag{C6}$$

where $c_{ML} = \cos(ML)$, atan2 is the four-quadrant inverse tangent, and r_{ij} are the entries of R_{w}.

C5 – Cross-Correlation Function

The cross-correlation function (CCF) between the 4-second window in a kinematic time series, $f[n]$, and its time-matched 4-second window in an electromyogram time series, $g[n]$, was calculated using:

$$(f \star g)[n] = \sum_{m=1}^{401} f[m]g[m+n] \tag{C7}$$

where the domain of $(f \star g)[n]$ is $n \in \mathbb{Z} : -400 \leq n \leq 400$; and the domain of both $f[n]$ and $g[n]$ is $n \in \mathbb{Z} : 1 \leq n \leq 401$.

The CCF was normalized using:

$$(f \star g)[n] = \frac{(f \star g)[n]}{\sqrt{\sum_{m=1}^{401}(f[m])^2 \sum_{m=1}^{401}(g[m])^2}} \tag{C8}$$

References for Appendix C

[1] Callaghan JP, Gunning JL, McGill SM. The relationship between lumbar spine load and muscle activity during extensor exercises. Phys Ther 1998;78:8–18.

[2] van den Tillaar R, Andersen V, Saeterbakken AH. Comparison of muscle activation and performance during 6 RM, two-legged free-weight squats. Kinesiol Slov 2014;20:5–16.

[3] Masani K, Sin VW, Vette AH, Thrasher AT, Kawashima N, Morris A, et al. Postural reactions of the trunk muscles to multi-directional perturbations in sitting. Clin Biomech 2009;24:176–82.

[4] Robertson G, Caldwell G, Hamill J, Kamen G, Whittlesey S. Research methods in biomechanics. 1st ed. Illinois: Human Kinetics; 2004.

[5] Craig JJ. Introduction to robotics: mechanics and control. 3rd ed. United Kingdom: Prentice Hall; 2004.

Appendix D: Chapter 4 – Mean Cross-Correlation Functions for Right Body Side Muscles

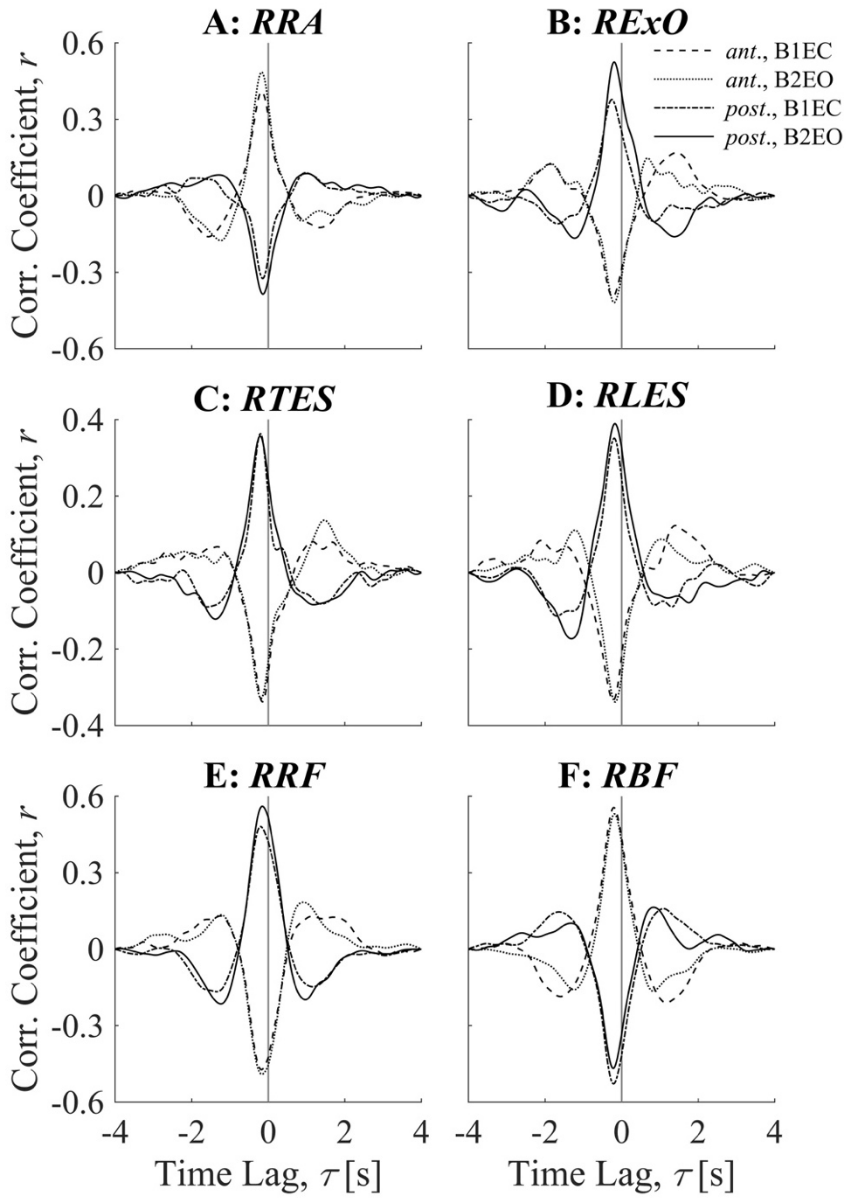

Figure D1: Mean cross-correlation functions across participants between right body side muscles and *anterior* for the Base 1 Eyes Closed (B1EC) (dashed line) and Base 2 Eyes Open (B2EO) (dotted line) conditions. Shown are also the mean cross-correlation functions across participants between right body side muscles and *posterior* for the B1EC (dash-dot line) and B2EO (solid line) conditions. Correlated muscles are: right rectus abdominis (*RRA*) (A), right external oblique

(*RExO*) (B), right thoracic erector spinae (*RTES*) (C), right lumbar erector spinae (*RLES*) (D), right rectus femoris (*RRF*) (E), and right biceps femoris (*RBF*) (F).

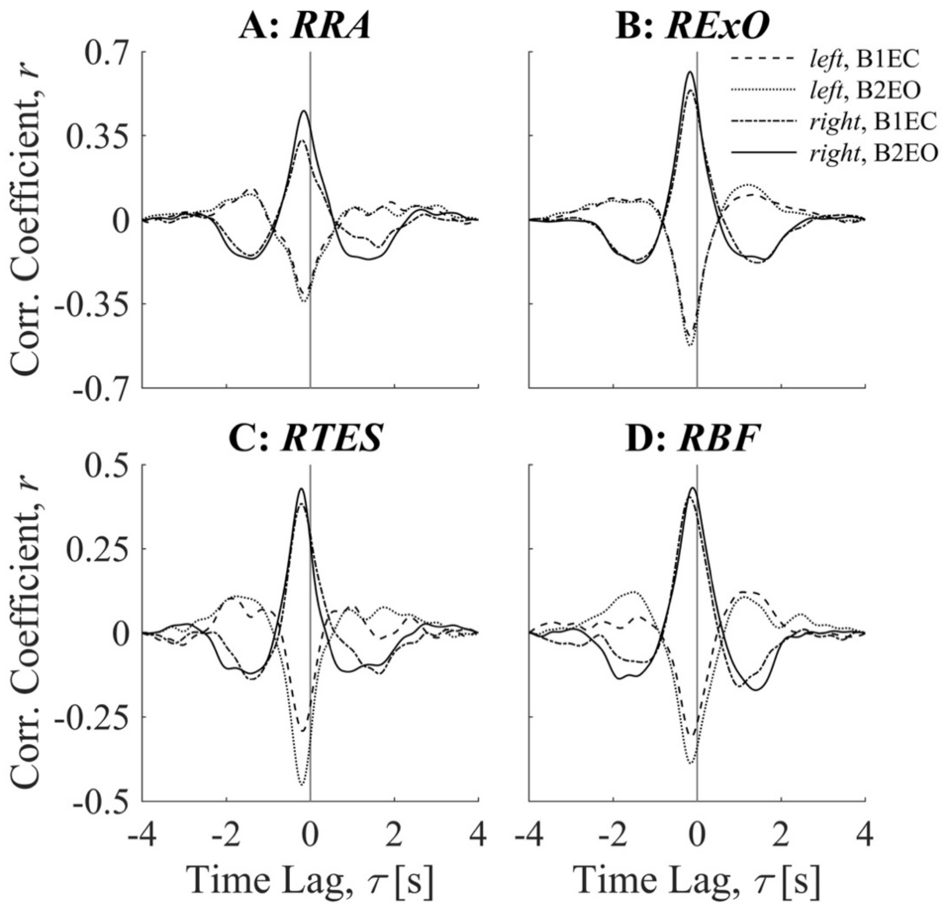

Figure D2: Mean cross-correlation functions across participants between right body side muscles and *left* for the Base 1 Eyes Closed (B1EC) (dashed line) and Base 2 Eyes Open (B2EO) (dotted line) conditions. Shown are also the mean cross-correlation functions across participants between right body side muscles and *right* for the B1EC (dash-dot line) and B2EO (solid line) conditions. Correlated muscles are: right rectus abdominis (*RRA*) (A), right external oblique (*RExO*) (B), right thoracic erector spinae (*RTES*) (C), and right biceps femoris (*RBF*) (D).

Appendix E: Chapter 5 – Supplementary Material

E1 – Force Plate Inertial Force and Moment

The inertial force, $\vec{F}_{\mathrm{I}}$, is the sum of forces applied by the force plate to the mass resting on the force plate transducers to (1) linearly accelerate the platform's center of mass (CoM); and (2) support its weight. The components of $\vec{F}_{\mathrm{I}}$ are:

$$\begin{bmatrix} F_{\mathrm{I}_x} \\ F_{\mathrm{I}_y} \\ F_{\mathrm{I}_z} \end{bmatrix} = m \begin{bmatrix} a_x \\ a_y \\ a_z \end{bmatrix} + R_{xyz}^{\mathrm{T}} \begin{bmatrix} 0 \\ mg \\ 0 \end{bmatrix} - \begin{bmatrix} 0 \\ mg \\ 0 \end{bmatrix} \tag{E1}$$

where m is the mass resting on the force plate transducers; a_x, a_y, and a_z are the components of the linear acceleration of the platform's CoM, $\vec{a}$, expressed in the platform coordinate system (PCS) provided in Figure E1; R_{xyz} is the rotation matrix capturing the orientation of PCS relative to the global coordinate system (GCS) provided in Figure E1; and g is the acceleration due to gravity.

The inertial moment, $\vec{M}_{\mathrm{I}}$, is the sum of moments applied by the force plate to m to (1) angularly accelerate the platform; and (2) support the moment created by $\vec{F}_{\mathrm{I}}$. The components of $\vec{M}_{\mathrm{I}}$ are:

$$\begin{gathered} \vec{M}_{\mathrm{I}} = \vec{I} \cdot \vec{\alpha} + \vec{d} \times \vec{F}_{\mathrm{I}} \\ \vec{M}_{\mathrm{I}} = \left(I_x\hat{\imath} + I_y\hat{\jmath} + I_z\hat{k}\right) \cdot \left(\alpha_x\hat{\imath} + \alpha_y\hat{\jmath} + \alpha_z\hat{k}\right) + \left(d_x\hat{\imath} + d_y\hat{\jmath} + d_z\hat{k}\right) \times \left(F_{\mathrm{I}_x}\hat{\imath} + F_{\mathrm{I}_y}\hat{\jmath} + F_{\mathrm{I}_z}\hat{k}\right) \\ \vec{M}_{\mathrm{I}} = \left(I_x\alpha_x + d_yF_{\mathrm{I}_z} - d_zF_{\mathrm{I}_y}\right)\hat{\imath} + \left(I_y\alpha_y - d_xF_{\mathrm{I}_z} + d_zF_{\mathrm{I}_x}\right)\hat{\jmath} + \left(I_z\alpha_z + d_xF_{\mathrm{I}_y} - d_yF_{\mathrm{I}_x}\right)\hat{k} \end{gathered} \tag{E2}$$

where I_x, I_y, and I_z are the principal components of the moment of inertia, $\vec{I}$, of the mass resting on the force plate transducers; α_x, α_y, and α_z are the components of the angular acceleration, $\vec{\alpha}$, of the platform; and d_x, d_y, and d_z are the components of the position, $\vec{d}$, of the CoM relative to the average force plate transducer location. Note that $\vec{I}$, $\vec{\alpha}$, and $\vec{d}$ are expressed in PCS.

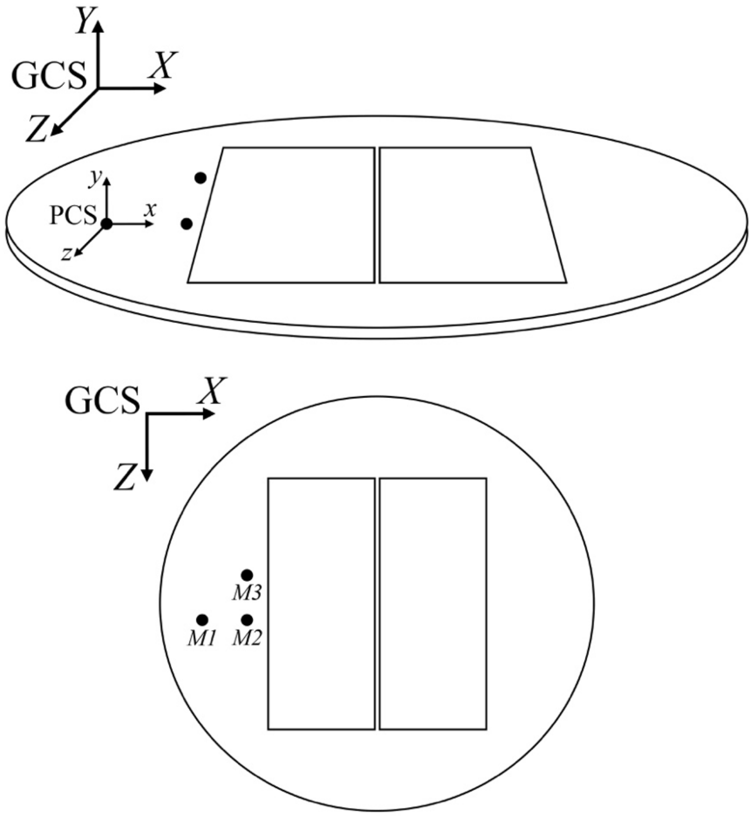

Figure E1: The orientations of the CAREN platform in its starting orientation relative to the global coordinate system (GCS); and of the platform coordinate system (PCS) relative to the CAREN platform. Three markers (*M1*, *M2*, and *M3*) were placed on the platform to define PCS, with *M1* and *M2* forming a line parallel to the *x* axis.

E2 – Platform Coordinate System

The PCS was defined as follows (Figure E1): (1) the *x* axis points from *M1* to *M2*; (2) an auxiliary vector (*AUX*) points from *M1* to *M3*; (3) the *y* axis is perpendicular to the *x* axis and *AUX* and points superior of the platform; (4) the *z* axis is perpendicular to the *x* and *y* axes and points posterior of the platform; and (5) the origin coincides with *M1*.

The *x*, *y*, and *z* axes were calculated using the following equations. The *x* axis was calculated using:

$$x = \frac{M2 - M1}{\|M2 - M1\|} \tag{E3}$$

where *M1* and *M2* are the position vectors, expressed in GCS, of Markers 1 and 2, respectively.

The auxiliary vector, AUX, was calculated using:

$$AUX = \frac{M3 - M1}{\|M3 - M1\|} \tag{E4}$$

where $M3$ is the position vector, expressed in GCS, of Marker 3.

The y axis was calculated using:

$$y = x \times AUX \tag{E5}$$

Finally, the z axis was calculated using:

$$z = x \times y \tag{E6}$$

E3 – Platform Kinematics

The linear acceleration of the platform was calculated using:

$$\vec{a} = R_{xyz}^{\mathrm{T}}(\vec{a})_{\mathrm{G}} \tag{E7}$$

where $(\vec{a})_{\mathrm{G}}$ is the linear acceleration of the platform, expressed in GCS.

The rotation matrix R_{xyz} was calculated using:

$$R_{xyz} = \begin{bmatrix} r_{11} & r_{12} & r_{13} \\ r_{21} & r_{22} & r_{23} \\ r_{31} & r_{32} & r_{33} \end{bmatrix} = \begin{bmatrix} x \cdot X & y \cdot X & z \cdot X \\ x \cdot Y & y \cdot Y & z \cdot Y \\ x \cdot Z & y \cdot Z & z \cdot Z \end{bmatrix} = [x \quad y \quad z] \tag{E8}$$

where it is noted that $X = [1\ 0\ 0]^{\mathrm{T}}$, $Y = [0\ 1\ 0]^{\mathrm{T}}$, and $Z = [0\ 0\ 1]^{\mathrm{T}}$.

The platform angles θ_x, θ_y, and θ_z were calculated using the Cardan xyz sequence [1]:

$$\begin{aligned} \theta_y &= \operatorname{atan2}\left(r_{13}, \sqrt{r_{23}^2 + r_{33}^2}\right) \\ \theta_x &= \operatorname{atan2}\left(-\frac{r_{23}}{c_{\theta_y}}, \frac{r_{33}}{c_{\theta_y}}\right) \\ \theta_z &= \operatorname{atan2}\left(-\frac{r_{12}}{c_{\theta_y}}, \frac{r_{11}}{c_{\theta_y}}\right) \end{aligned} \tag{E9}$$

where $c_{\theta_y} = \cos(\theta_y)$ and atan2 is the four-quadrant inverse tangent.

E4 – Reduced Inertial Force and Moment in Unloaded Platform Translations

For translations of the unloaded platform, $\vec{F} = \vec{F}_{\mathrm{I}}$, $R_{xyz} = I_{3x3}$, and $\vec{\alpha} = \vec{0}$. Note that I_{3x3} is the identity matrix.

For x translations, additionally, $a_y = a_z = 0$. Therefore, for x translations, the reduced inertial force and moment are:

$$\begin{bmatrix} F_{I_x} \\ F_{I_y} \\ F_{I_z} \end{bmatrix} = m\begin{bmatrix} a_x \\ 0 \\ 0 \end{bmatrix} + I_{3x3}\begin{bmatrix} 0 \\ mg \\ 0 \end{bmatrix} - \begin{bmatrix} 0 \\ mg \\ 0 \end{bmatrix} = \begin{bmatrix} ma_x \\ 0 \\ 0 \end{bmatrix}$$

$$\vec{M}_I = \left(I_x(0) + d_y(0) - d_z(0)\right)\hat{\imath} + \left(I_y(0) - d_x(0) + d_zF_x\right)\hat{\jmath} + \left(I_z(0) + d_x(0) - d_yF_x\right)\hat{k} \tag{E10}$$

$$\vec{M}_I = d_zF_x\hat{\jmath} - d_yF_x\hat{k}$$

For y translations, additionally, $a_x = a_z = 0$. Therefore, for y translations, the reduced inertial force and moment are:

$$\begin{bmatrix} F_{I_x} \\ F_{I_y} \\ F_{I_z} \end{bmatrix} = m\begin{bmatrix} 0 \\ a_y \\ 0 \end{bmatrix} + I_{3x3}\begin{bmatrix} 0 \\ mg \\ 0 \end{bmatrix} - \begin{bmatrix} 0 \\ mg \\ 0 \end{bmatrix} = \begin{bmatrix} 0 \\ ma_y \\ 0 \end{bmatrix}$$

$$\vec{M}_I = \left(I_x(0) + d_y(0) - d_zF_y\right)\hat{\imath} + \left(I_y(0) - d_x(0) + d_z(0)\right)\hat{\jmath} + \left(I_z(0) + d_xF_y - d_y(0)\right)\hat{k} \tag{E11}$$

$$\vec{M}_I = -\,d_zF_y\hat{\imath} + d_xF_y\hat{k}$$

For z translations, additionally, $a_x = a_y = 0$. Therefore, for z translations, the reduced inertial force and moment are:

$$\begin{bmatrix} F_{I_x} \\ F_{I_y} \\ F_{I_z} \end{bmatrix} = m\begin{bmatrix} 0 \\ 0 \\ a_z \end{bmatrix} + I_{3x3}\begin{bmatrix} 0 \\ mg \\ 0 \end{bmatrix} - \begin{bmatrix} 0 \\ mg \\ 0 \end{bmatrix} = \begin{bmatrix} 0 \\ 0 \\ ma_z \end{bmatrix}$$

$$\vec{M}_I = \left(I_x(0) + d_yF_z - d_z(0)\right)\hat{\imath} + \left(I_y(0) - d_xF_z + d_z(0)\right)\hat{\jmath} + \left(I_z(0) + d_x(0) - d_y(0)\right)\hat{k} \tag{E12}$$

$$\vec{M}_I = d_yF_z\hat{\imath} - d_xF_z\hat{\jmath}$$

E5 – Reduced Inertial Force and Moment in Unloaded Platform Rotations

For rotations of the unloaded platform, $\vec{F} = \vec{F}_I$.

For x rotations, additionally, $a_x = \alpha_y = \alpha_z = 0$. Therefore, for x rotations, the reduced inertial force and moment are:

$$\begin{bmatrix} F_{I_x} \\ F_{I_y} \\ F_{I_z} \end{bmatrix} = m\begin{bmatrix} 0 \\ a_y \\ a_z \end{bmatrix} + R_{xyz}^{T}\begin{bmatrix} 0 \\ mg \\ 0 \end{bmatrix} - \begin{bmatrix} 0 \\ mg \\ 0 \end{bmatrix} \tag{E13}$$

$$\vec{M}_\mathrm{I} = \left(I_x\alpha_x + d_yF_z - d_zF_y\right)\hat{\imath} + \left(I_y(0) - d_xF_z + d_zF_x\right)\hat{\jmath} + \left(I_z(0) + d_xF_y - d_yF_x\right)\hat{k}$$

$$\vec{M}_\mathrm{I} = \left(I_x\alpha_x + d_yF_z - d_zF_y\right)\hat{\imath} + (-d_xF_z + d_zF_x)\hat{\jmath} + \left(d_xF_y - d_yF_x\right)\hat{k}$$

For y rotations, additionally, $a_y = \alpha_x = \alpha_z = 0$. Therefore, for y rotations, the reduced inertial force and moment are:

$$\begin{gathered} \begin{bmatrix} F_{\mathrm{I}_x} \\ F_{\mathrm{I}_y} \\ F_{\mathrm{I}_z} \end{bmatrix} = m \begin{bmatrix} a_x \\ 0 \\ a_z \end{bmatrix} + R_{xyz}^\mathrm{T} \begin{bmatrix} 0 \\ mg \\ 0 \end{bmatrix} - \begin{bmatrix} 0 \\ mg \\ 0 \end{bmatrix} \\ \vec{M}_\mathrm{I} = \left(I_x(0) + d_yF_z - d_zF_y\right)\hat{\imath} + \left(I_y\alpha_y - d_xF_z + d_zF_x\right)\hat{\jmath} + \left(I_z(0) + d_xF_y - d_yF_x\right)\hat{k} \\ \vec{M}_\mathrm{I} = \left(d_yF_z - d_zF_y\right)\hat{\imath} + \left(I_y\alpha_y - d_xF_z + d_zF_x\right)\hat{\jmath} + \left(d_xF_y - d_yF_x\right)\hat{k} \end{gathered} \tag{E14}$$

For z rotations, additionally, $a_z = \alpha_x = \alpha_y = 0$. Therefore, for z rotations, the reduced inertial force and moment are:

$$\begin{gathered} \begin{bmatrix} F_{\mathrm{I}_x} \\ F_{\mathrm{I}_y} \\ F_{\mathrm{I}_z} \end{bmatrix} = m \begin{bmatrix} a_x \\ a_y \\ 0 \end{bmatrix} + R_{xyz}^\mathrm{T} \begin{bmatrix} 0 \\ mg \\ 0 \end{bmatrix} - \begin{bmatrix} 0 \\ mg \\ 0 \end{bmatrix} \\ \vec{M}_\mathrm{I} = \left(I_x(0) + d_yF_z - d_zF_y\right)\hat{\imath} + \left(I_y(0) - d_xF_z + d_zF_x\right)\hat{\jmath} + \left(I_z\alpha_z + d_xF_y - d_yF_x\right)\hat{k} \\ \vec{M}_\mathrm{I} = \left(d_yF_z - d_zF_y\right)\hat{\imath} + (-d_xF_z + d_zF_x)\hat{\jmath} + \left(I_z\alpha_z + d_xF_y - d_yF_x\right)\hat{k} \end{gathered} \tag{E15}$$

E6 – Sum of Squared Errors (SSE) Expressions

For x translations, the SSE expressions that were minimized are:

$$\begin{gathered} \mathrm{SSE}_{F_x}(m) = \sum_{i=1}^{N} [F_x(i) - ma_x(i)]^2 \\ \mathrm{SSE}_{M_y}(d_z) = \sum_{i=1}^{N} \left[M_y(i) - d_zF_x(i)\right]^2 \\ \mathrm{SSE}_{M_z}\left(d_y\right) = \sum_{i=1}^{N} \left[M_z(i) + d_yF_x(i)\right]^2 \end{gathered} \tag{E16}$$

For x rotations, the SSE expression that was minimized is:

$$\mathrm{SSE}_{M_x}(I_x) = \sum_{i=1}^{N} \Big[M_x(i) - \Big(I_x\alpha_x(i) + d_yF_z(i) - d_zF_y(i)\Big)\Big]^2 \tag{E17}$$

For y translations, the SSE expressions that were minimized are:

$$\begin{aligned}
\mathrm{SSE}_{F_y}(m) &= \sum_{i=1}^{N} \big[F_y(i) - ma_y(i)\big]^2 \\
\mathrm{SSE}_{M_x}(d_z) &= \sum_{i=1}^{N} \big[M_x(i) + d_zF_y(i)\big]^2 \\
\mathrm{SSE}_{M_z}(d_x) &= \sum_{i=1}^{N} \big[M_z(i) - d_xF_y(i)\big]^2
\end{aligned} \tag{E18}$$

For y rotations, the SSE expression that was minimized is:

$$\mathrm{SSE}_{M_y}(I_y) = \sum_{i=1}^{N} \Big[M_y(i) - \Big(I_y\alpha_y(i) - d_xF_z(i) + d_zF_x(i)\Big)\Big]^2 \tag{E19}$$

For z translations, the SSE expressions that were minimized are:

$$\begin{aligned}
\mathrm{SSE}_{F_z}(m) &= \sum_{i=1}^{N} [F_z(i) - ma_z(i)]^2 \\
\mathrm{SSE}_{M_x}(d_y) &= \sum_{i=1}^{N} \big[M_x(i) - d_yF_z(i)\big]^2 \\
\mathrm{SSE}_{M_y}(d_x) &= \sum_{i=1}^{N} \big[M_y(i) + d_xF_z(i)\big]^2
\end{aligned} \tag{E20}$$

For z rotations, the SSE expression that was minimized is:

$$\mathrm{SSE}_{M_z}(I_z) = \sum_{i=1}^{N} \Big[M_z(i) - \Big(I_z\alpha_z(i) + d_xF_y(i) - d_yF_x(i)\Big)\Big]^2 \tag{E21}$$

SSE expressions were minimized using the function *fminsearch* in MATLAB (version R2017a, MathWorks, Natick, United States).

References for Appendix E

[1] Craig JJ. Introduction to robotics: mechanics and control. 3rd ed. United Kingdom: Prentice Hall; 2004.